POLISH ACADEMY OF SCIENCES – WROCŁAW BRANCH
WROCŁAW UNIVERSITY OF TECHNOLOGY

# ARCHIVES OF CIVIL AND MECHANICAL ENGINEERING

Quarterly
Vol. VI, No. 4

WROCŁAW 2006

ARCHIVES OF CIVIL AND MECHANICAL ENGINEERING
Vol. VI 2006 No. 4

# Some problems of designing the main drives of universal machine tools

JAN WOJCIECHOWSKI, PRZEMYSLAW WYGLĄDACZ
Institute of Production Engineering and Automation, Wrocław University of Technology,
Łukasiewicza 5, 50-371 Wrocław

The problem of fitting the characteristic of the universal machine tool's main drive to anticipated machining tasks is considered. The power demand and the cutting torque demand for turning and milling are analysed. It is shown that by employing a multiplying gear one can obtain a constant machining power in a wide range of spindle speeds whereby both steel and aluminium alloys can be efficiently machined.

Keywords: *machine tool, main drive, designing*

## 1. Introduction

As the range of cutting speed increases, there is a tendency to increase the rotational speed of spindles in the design of the main drives of machine tools. In the years 1989–1999, the maximum spindle speed increased ten times.

Another requirement connected with a drive towards higher metal removal rates is that rotational speed be changed in a stepless way to maintain the optimum cutting speed on the one hand and to minimize self-excited vibration on the other one [1]. Still another important requirement is that high (much over the capacity of the driving motor) spindle speeds should be assured at a constant motor power. The power is indispensable for efficient machining at both low and high spindle speeds. The efficient machining of materials characterized by high specific cutting resistance, such as steel, requires a low spindle speed at a constant power, whereas by increasing this speed one can efficiently machine such materials as aluminium and its alloys as well as other materials with a much weaker cutting resistance but requiring a much higher cutting speed. The high-speed electrospindles used today are often incapable of meeting the above requirements. The latter, however, can be met by incorporating additional gears, both reducing and multiplying the motor speed, into the main drive. The possibilities of applying of such gears in the main drives of selected universal machine tools are explored in this paper.

## 2. Shaping main drive characteristics

The design of the main drive of machine tool consists in the selection of proper commercially available subassemblies. In order to choose a suitable drive unit, one must analyse and compare the required load curves for the intended machining processes with those of a potential motor equipped with a power supply unit and possibly a gear transmission [2]. The drive should be capable of performing all the intended tasks at a high degree of machine tool production potential utilization. The drive's load curves can be determined if one has such input data as:

- the rotational speeds required,
- the power needed to realize the machining process,
- the cutting torque.

To precisely determine the input data one must know the machining tasks which a given machine tool is to perform. In the case of universal machine tools, it is not easy to foresee what procedures will be applied to workpieces. The latter could be used to determine the load characteristic.

One of the methods of preselecting a motor for the main drive is the method of maximum loads [2], in which the worst possible drive loading conditions that may occur during the operation of the machine tool are selected. This means that roughing operations in which large-diameter layers are cut and operations involving high rotational speeds are considered. The choice of machining parameters should take into account the machine tool's load-bearing structure, its ways and the machining parameters permissible for the cutting tool materials.

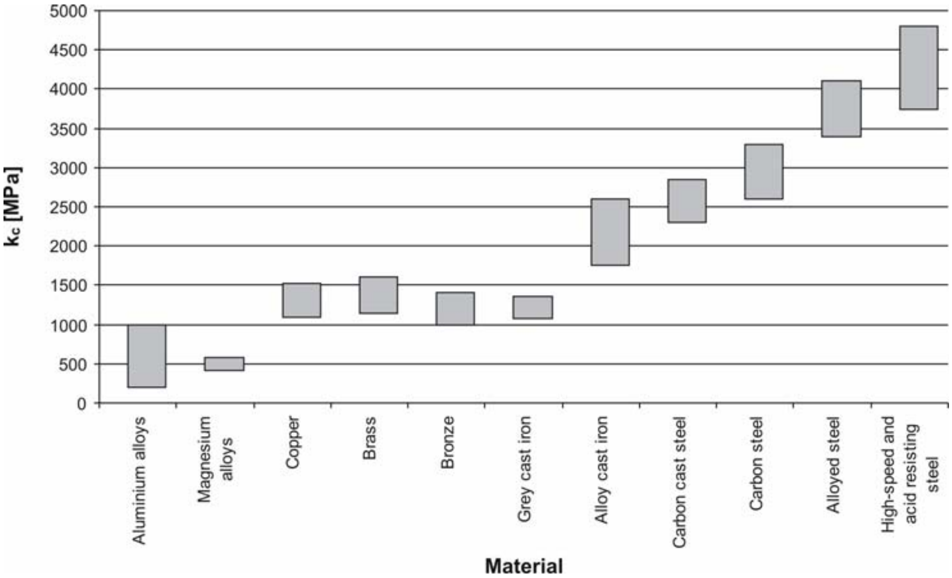

Fig. 1. Specific cutting resistance $k_c$ of different materials

The method of maximum loads is applied here to show how by incorporating a multiplying gear into the kinematic chain of the main drive the machine tool's functional properties can be improved. In order to determine the main drive's load characteristic, the machining power and the torque were calculated. Turning and milling, as the main ways of machining by universal machine tools, were investigated. Much heavier loads than the ones associated with, for example, drilling are involved in the above processes.

The machining of objects made of steel St60-2 and aluminium alloy Al99,8_F6 (DIN) was analysed since the latter are the most commonly machined materials with diametrically different cutting resistances (Figure 1).

Sandvik Coromant's catalogues were used for the selection of cutting tools and machining parameters for the exemplary procedures [3].

## 3. Analysis of main drive characteristics

The load characteristics of the main drives of universal machine tools: a milling machine and a lathe were analysed. In the case of the milling machine, face milling by a cutter with a typical diameter $d$ = 50 mm and number of inserts $z$ = 4 was chosen. Insert material CT530 (ensuring a high cutting speed) recommended by Sandvik Coromant was used for machining both steel and aluminium [3]. In the case of the lathe, a roller with diameter $d$ = 50 mm was straight turned and the insert material was CT630.

The machining parameters used in the analysis of main drive loading for the two machines are shown in the Table.

Table. Machining parameters for milling and turning

| Stock<br>Method of machining | | St60–2 | | Al99.8_F6 | |
|---|---|---|---|---|---|
| Milling | Feed $f_z$ | Feed per cutting edge $f_z$ [mm/edge] | | | |
| | Cutting depth $a_p$<br>and cutting speed $v_c$ | 0.1 | 1 | 0.1 | 1 |
| | $a_p$ [mm] | 1–10 | | | |
| | $v_c$ [m/min] | 360 | 90 | 1130 | 385 |
| Turning | Feed $f$ | Feed $f$ [mm/r] | | | |
| | Cutting depth $a_p$<br>and cutting speed $v_c$ | 0.1 | 1.5 | 0.1 | 1.5 |
| | $a_p$ [mm] | 1–5 | | | |
| | $v_c$ [m/min] | 810 | 180 | 2080 | 930 |

In order to determine the required power $P_{\max}$ and the cutting resistance torque $M$, first maximum cutting component force $F_{c\max}$ was calculated. Specific cutting resistance $k_c$ determines the material properties which affect the above force. The resistance is not constant and depends mainly on the rate of feed. A computer program and relevant data contained in the Sandvik Coromant catalogue were used to calculate the force $F_{c\max}$ [3]. Maximum cutting component needed to calculate the machining power $P_{\max}$ is expressed by this relation:

$$F_{c\max} = k_c \cdot a_p \cdot f \text{ [N]}, \tag{1}$$

where:

$F_{c\max}$ – the maximum cutting component force,
$k_c$ – the specific cutting resistance,
$a_p$ – the depth of cut,
$f$ – the feed.

Maximum machining power $P_{\max}$ for force $F_{c\max}$ and recommended cutting speed $v_c$ is written as:

$$P_{\max} = \frac{F_{c\max} \cdot v_c}{1000 \cdot 60} \text{ [kW]}, \tag{2}$$

where:

$P_{\max}$ – the maximum machining power,
$v_c$– the cutting speed.

The cutting resistance torque $M$ can be expressed by:

$$M = \frac{P_{\max} \cdot 30 \cdot d}{v_c} \text{ [Nm]}, \tag{3}$$

where:

$M$ – the cutting resistance torque,
$d$ – the tool's or the workpiece's diameter for respectively milling and turning.

On the basis of the calculations the power demand and cutting torque diagrams for the machining parameters shown in Table 1 were drawn.

The milling power demand diagram (Figure 2) for steel (the darker area) and aluminium (the lighter area) shows that the load curve for steel differs significantly from that for aluminium. In the case of steel, power demand occurs at lower rotational speeds than in the case of aluminium. Thus a machine tool designed for machining steel will not be efficient in the machining of aluminium products since it is incapable of sufficiently high rotational speeds needed to achieve high productivity. Whereas a machine tool intended only for machining aluminium will not have a sufficiently high power in the lower range of rotational speeds in which the power demand for machining steel is high.

The main drive motor power diagram (broken line) was superimposed on the power demand diagram. The Mitsubishi SJ-P F7.5 motor was selected since most of its power demand diagram is under the line demarcating the motor operation area. It became apparent that as regards its power characteristic the motor quite well met the requirements in the case of steel. Unfortunately, quite a large portion of the power demand area for machining aluminium was outside the motor operation field. In order to expand the latter, a multiplying gear was employed. Such a gear ratio was selected so as to obtain the widest possible range of spindle speed at a constant power. Gear ratio $i$ equal to 3 was adopted:

$$i = \frac{n_{\max}}{n_p}, \tag{4}$$

where:

$n_{\max}$ – the maximum motor speed,
$n_p$ – the lowest rotational speed at which the motor attains the maximum power.

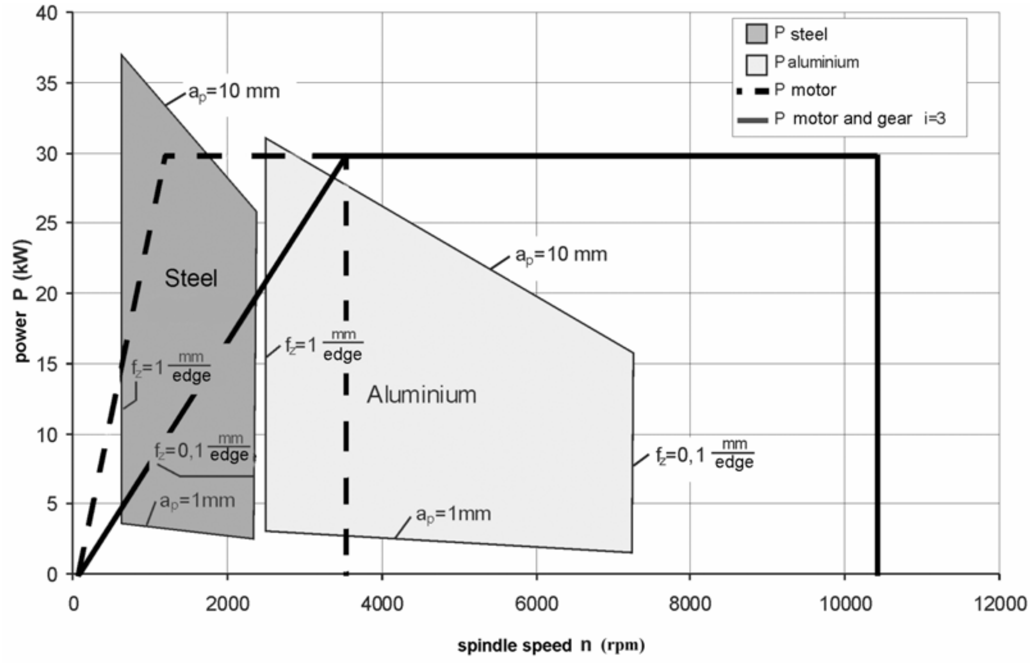

Fig. 2. Power demand versus spindle speed diagrams for milling steel and aluminium using Ø50 mm face milling cutter at different machining parameters $a_p$ and $f_z$. Power diagrams for Mitsubishi SJ-P F7.5 motor with and without gear with $i$ = 3

The power demand diagram for the motor with the gear is represented by a solid line. Thanks to the gear the main drive’s operation field expanded and covered the rest of the area of possible loads for machining aluminium.

Besides fitting the motor power characteristic to the power demand curve one should also choose proper motor torque characteristics. And so a torque diagram was made in a way similar to that of the power diagram for the machining parameters adopted (Figure 3).

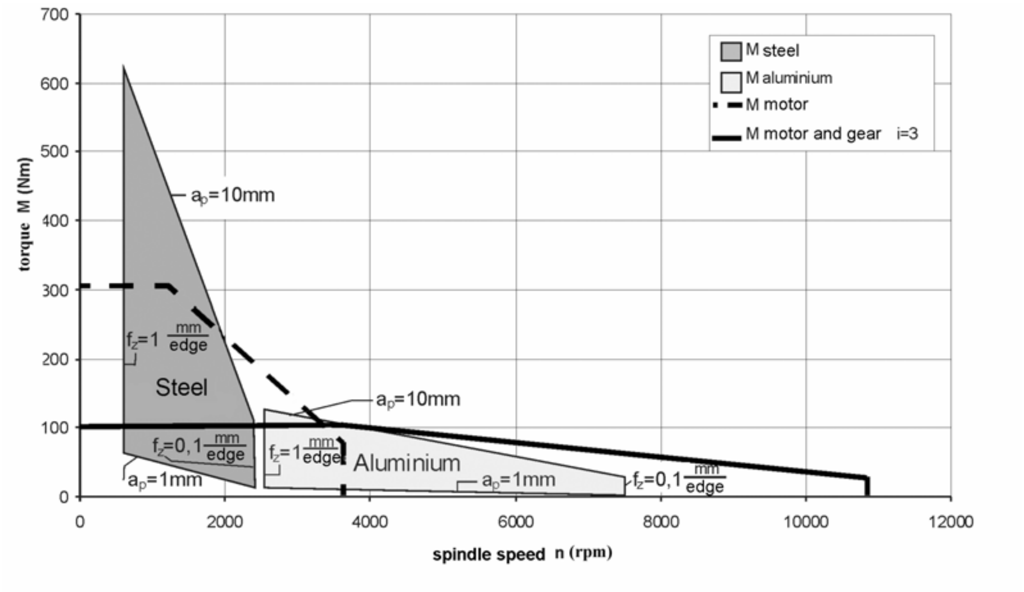

Fig. 3. Torque demand versus spindle speed diagrams for milling steel and aluminium using Ø50 mm face milling cutter at different machining parameters $a_p$ and $f_z$. Torque diagrams for Mitsubishi SJ-P F7.5 motor with and without gear with $i = 3$

As in the case of power demand curves, the torque demand characteristic for steel is different from that for aluminium. The machining of steel requires high torques at lower rotational speeds (the darker area), while the machining of aluminium results in much lighter loading of the main drive, but at higher rotational speeds (the lighter area). The situation is similar to that for power. A machine tool for machining steel will not be fully utilized when used for machining aluminium and vice versa.

Also here the motor mechanical characteristic (broken line) is superimposed on the torque demand curve. The motor’s torque versus its speed extends over a considerable part of the field corresponding to the possible drive loads during the machining of steel, but covers only a small part of the area representing the resistance during the machining of aluminium. This means that at limited machining parameters (the rate of feed and the depth of cut are located below the broken line) it is possible to machine steel and aluminium at insufficient speeds. When additional gear with the gear ratio $i = 3$ is employed, the range of useful spindle speeds (solid line) increases, which, in turn, results in the reduction of the spindle torque $M_i$ relative to the motor torque $M$:

$$M_i = \frac{M \cdot \eta}{i}, \tag{5}$$

where:

$M_i$ – the spindle torque,

*M* – the motor torque,
$\eta$ – the efficiency of the gear,
*i* – the gear ratio.

Although the torque decreases nearly three times, the drive operation range increases sufficiently to meet almost fully the torque demand for the machining of aluminium. This is due to the (5–8 times) lower specific cutting resistance.

A similar analysis was carried out for turning. As in the case of milling, power demand (Figure 4) and torque diagrams (Figure 5) were drawn.

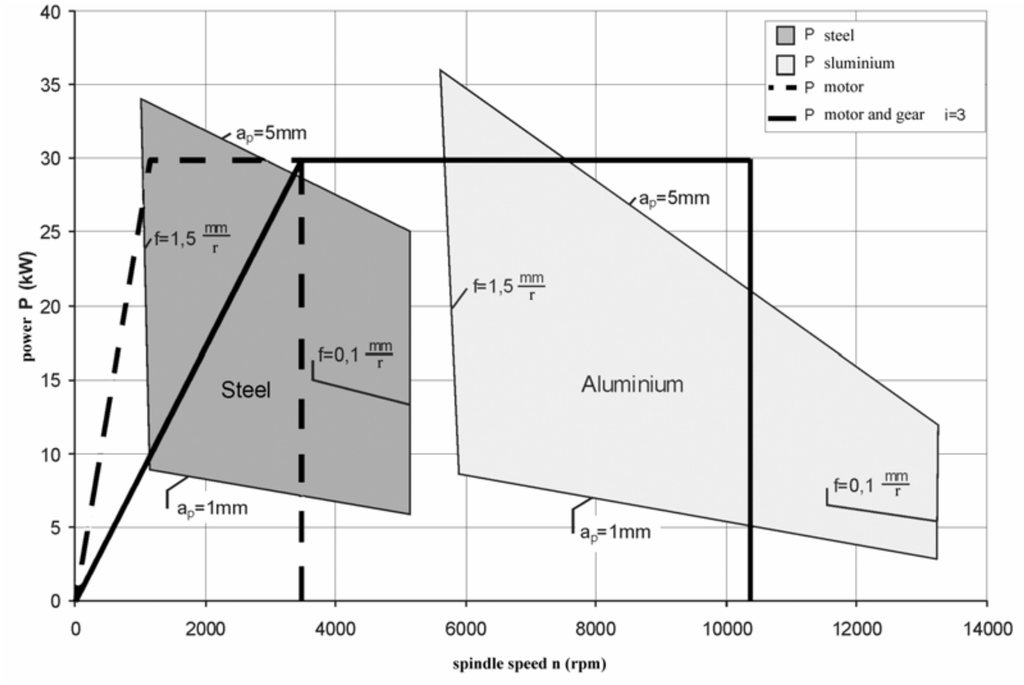

Fig. 4. Power demand versus spindle speed diagrams for straight turning of Ø50 mm steel or aluminium roller at different machining parameters $a_p$ and $f_z$. Power diagrams for Mitsubishi SJ-P F7.5 motor with and without gear with $i = 3$

Also here the load curves for machining steel differ much, both with regard to power and torque, from those for machining aluminium. By extending the range of useful rotational speeds for the main drive through the adoption of an additional gear one can meet the power and torque demand in a much wider range of possible loads at given parameters. The Mitsubishi SJ-PF7.5 motor without a transmission gear or at $i = 1$ enables the machining of steel at lower cutting speeds (operation at machining parameters located under the broken line representing the motor characteristic is possible), but no rotational speeds sufficiently high for machining aluminium at recommended parameters are attained. Neither a high-speed motor will ensure a sufficient

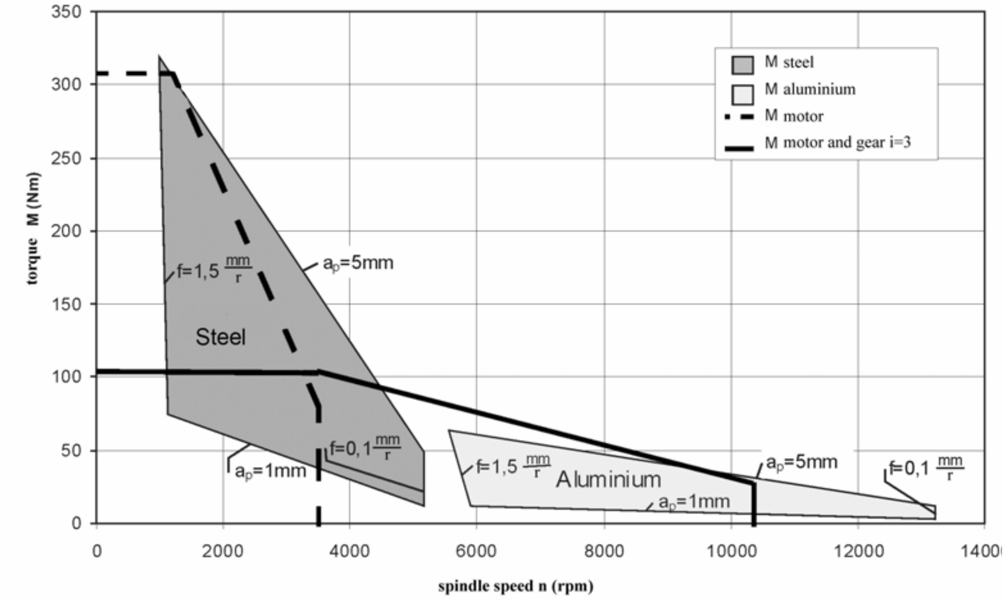

Fig. 5. Torque demand versus spindle speed diagrams for straight turning of Ø50 mm steel or aluminium roller at different machining parameters $a_p$ and $f_z$. Power diagrams for Mitsubishi SJ-P F7.5 motor with and without gear with $i = 3$

torque at the lower rotational speeds used for machining steel (the area of possible loads located under the solid line representing the characteristic of the motor with an additional gear). But the combination of the characteristics, which is possible thanks to the additional gear in the main drive's kinematic chain, increases the machine tool's operating capability by extending the range of useful spindle speeds.

## 4. Conclusions

The following conclusions can be drawn from the above analysis:

- The mechanical characteristics of motors show their torque or rated power within the entire range of rotational speed, which corresponds to the most unfavourable motor operating conditions: the motor may operate under the maximum permissible load for an extended time. This occasionally occurs during the drilling of deep boreholes, but prolonged operation under variable loading occurs much more often in practice. Then an *ED* (an index showing the permissible percentage of maximum load time in a specified time interval) characteristic is superimposed on the power demand curve. Such loading occurs in most universal and special-purpose machine tools [2].
- When designing a drive, one can choose a motor with a lower power but one must bear in mind the range of machining parameters will decrease. The parameters can be read from the diagram (feasible parameters are under the line representing the maximum power – Figures 2 and 4). One must take into account the costs of using

larger motors and electronic power supply devices. Thus the permissible machining parameters can be specified during the preliminary selection of the main drive.

- Motor overload is allowable for a short time only (depending on the motor thermal operating conditions), but the motor cannot be loaded with a torque higher than the peak catalogue torque since it will be stopped (its protection will be actuated or the motor may be damaged).

To verify the preselected motor one should do thermal stability calculations for it.

Due to their properties contemporary tool materials can be machined in a very wide range of machining parameters. But the existing NC machine tool main drive designs usually do not allow one to fully exploit this possibility. In order to extend the functionality of a machine tool, one can incorporate an additional gear into the main drive's kinematic chain. This will expand the range of rotational speed at a quite good power and torque characteristics and make the machining of materials with widely different cutting resistances more efficient. The solution proposed is suitable for two machine tools: one for machining materials at low speeds and high cutting resistances and the other for machining at high speeds and low cutting resistances. The introduction of an additional gear has the advantage that it reduces the power demand whereby a smaller power supply unit is needed.

The gear ratio can be changed by mechanically reconfiguring the machine tool. The most convenient solution is to control the gear through the machine tool's control system since the latter when analysing the set machining parameters will select the proper gear ratio.

## References

[1] Krzyżanowski J., Nitek W., Wojciechowski J.: *Rozwój napędów obrabiarek skrawających (The development of machine tool drives)*, Napędy i sterowanie, 2001, No. 5, pp. 12–16.
[2] Wrotny L. T.: *Projektowanie obrabiarek. Zagadnienia ogólne i przykłady obliczeń (Design of machine tools. General problems and examples of calculations)*, WNT, Warsaw, 1986.
[3] The Internet catalogue of Sandvik Coromant products: http://www.coromant.sandvik.com/pl.
[4] Mitsubishi General Catalogue, March 1999.

## Wybrane problemy projektowania głównych napędów uniwersalnych obrabiarek skrawających

W konstrukcji głównych napędów obrabiarek skrawających występuje tendencja do wzrostu obrotowych prędkości wrzecion związana z poszerzaniem się zakresu prędkości skrawania.

Maksymalne prędkości obrotowe wrzecion w okresie 1989–1999 zwiększyły się dziesięciokrotnie. Innym wymaganiem, wiążącym się z dążeniem do zwiększenia wydajności skrawania, jest możliwość bezstopniowej zmiany prędkości obrotowej. Jest to niezbędne z jednej strony do utrzymania, w każdych warunkach obróbki, optymalnej prędkości skrawania, z drugiej zaś – do minimalizowania drgań samowzbudnych [1]. Do istotnych wymagań należy także zapewnienie dużego, znacznie przekraczającego możliwości silnika napędowego, zakresu prędkości obrotowych wrzeciona przy stałej mocy. Moc ta jest niezbędna do wydajnego skrawania zarówno przy małych, jak i dużych prędkościach obrotowych wrzeciona. Wydajne skrawanie materiałów charakteryzujących się dużym właściwym oporem skrawania, takich jak np. stal, wymaga małej prędkości obrotowej wrzeciona przy stałej mocy. Zwiększenie zaś tej prędkości umożliwia wydajne skrawanie takich materiałów jak np. aluminium i jego stopy i innych materiałów o znacznie mniejszych właściwych oporach skrawania, a wymagających znacznie większych prędkości skrawania. Stosowane obecnie szybkoobrotowe elektrowrzeciona bardzo często nie odpowiadają w pełni tym wymaganiom. Mogą natomiast je spełnić, gdy w napędzie głównym zostaną zastosowane dodatkowe przekładnie mechaniczne zarówno redukujące, jak i zwielokratniające prędkość obrotową silnika. Możliwości zastosowania tych ostatnich przekładni w napędach głównych przykładowych obrabiarek uniwersalnych zaprezentowano w niniejszym artykule.

ARCHIVES OF CIVIL AND MECHANICAL ENGINEERING
Vol. VI 2006 No. 4

# The possibilities of applying of artificial neural networks in automatic diagnostic system of machine cutting process

M. MIERNIK, M. KOŁODZIEJ
Wrocław University of Technology, Wybrzeże Wyspiańskiego 25, 50-370 Wrocław

The causes of failures in contemporary automatic diagnostic systems working with use of neural networks in industrial conditions are given. It has been stated that one of the basic causes was the lack of opportunity to perform logical operations by the artificial neuron model of McCulloch and Pitts which makes the core of artificial neural networks programs. A new method of data gathering and initial preparation has been offered here, based on the methods derived from non-linear dynamics, fuzzy sets and the theory of chaos. The data processed in such a way are transferred to the neural networks of Feed Forward Back Propagation type, which allows shortening the network's training, increasing the calculations speed and shortening the reaction inertness time of the FFBP network (on-line mode).

Keywords: *neural networks, diagnostics, non-linear dynamics*

## 1. Introduction

Diagnostics and supervision of cutting tools and the machine cutting process itself are very important subjects of chip machining technology. Progressive wear of the cutting blade deteriorates the quality of the processed surface and may be the cause for interferences in the machine cutting process [10]. Unfortunately, evaluation of the technical conditions of the cutting blade during the machine cutting process is impossible in practice and may be carried out only when interrupting the machine cutting process. During the process the conditions of a cutting blade may be evaluated only on the basis of measurements of indirect values that depend, among others, on wear of the blade. The most common indirect values applied as a tool wear-off factors are: machine cutting force components, acoustic emission, vibrations and others.

In the diagnostics systems that are based on evaluation of wear off of the cutting blade, the most commonly used methods consist in measurements of machine cutting forces and derivative figures and measurement of acoustic emission. It should be stressed that phenomena occurring during the machine cutting process are connected not only with the value of the blade wear off, but also with, for instance, the shape of the blade wear, blade geometry, machine cutting conditions, blade material and object being cut. Moreover, the connection between natural wear off and value of the signal measured is very complex and is of rather statistical than determined character. The values of the parameters used in the models of the process are characterized by a definite uncertainty level, for example, the properties of the material may oscillate in a certain range. Hence, it is said that in the future, the monitoring systems that are based on more that only one value of measured signal obtained from a sensor will be used. However, the application of many sensors generates the problem of reduction of copious information to a few best, most reliable symptoms, which may be used in the monitoring systems [3, 4, 7, 8, 10].

Many researches have been carried out both in Poland and all over the world in order to solve that problem [4, 7]. Nowadays the methods of artificial intelligence seem to be the best solution. Among the models applied in damage detection, the analytic models, neural and fuzzy models are most significant. Models mostly describe the object in normal conditions (without any damage). They enable establishing the residua, which reflect the differences between watched functioning of the object and normal behaviour defined by the model. Residua are mostly calculated as the differences between the output signals measured and the output signals modelled. The values of the residua for the undamaged model approach the value of zero. The values of the residua differing from zero stand for damage symptoms [1, 2, 5, 8].

## 2. Models for the detection of wear off and the damages of a cutting blade

In order to detect the damage, the following analytical models are applied:

1. Physical model – it is applied to detect small-size damage because of the fact that physical equations describe connections between process variables in the most complete way. The objects shall be described by relatively simple relations because of difficulties in constructing this model.
2. Linear equations – they make the basis for designing diagnostic observer.
3. Condition observer – it stands for an algorithm that is used for the approximation of the description of dynamic object conditions on the basis of input and output signals.
4. Continuous or discrete transmittances – they define the relation of Laplace’s transform of the output signal to Laplace’s transform of the input signal at zero initial conditions. They are used for the description of dynamic properties of linear objects.

In the case where construction of analytical models is very difficult or even impossible task and our knowledge about the diagnosed object is vague, we may use fuzzy models to detect damages. The structure of such a model is based on three blocks: dispersion block, conclusion block and sharpening block. Input signals are sent to the input to the dispersion block in which a level of adherence of this signal to particular fuzzy sets is established. On the basis of established now relativity level of input signals, the conclusion block establishes the resulting output adherence function. The last block (of sharpening) establishes a detailed output value on the basis of the resulting output adherence function obtained. In order to set up the rules that define operation of the object, we may take advantage of the experience of a process technologist or operator as well as accessible measurement data. If, however, this knowledge is not complete or imperfect, we may obtain incorrect model of the process [8].

Neural networks are the most effective tool for modelling dynamic objects or in the case where the mathematic model of the diagnosed process is not known. They are useful for modelling any non-linearity, introduction of generalities and forecasting trends. Moreover, they are fast and resistant to interferences. Generally saying they do not require any mathematic rules or formulas.  The basic structure of the network may remain unchanged but its particular elements may be modified. Thus, a more and more precise model of the process considered may be constructed without interference with the network structure. Teaching the neural networks consists in calculating output values on the basis of input data. If the output values calculated by the network do not comply with the answer given, then values are corrected and new values of network's weight factors are established. This process of trials and errors lasts until the network learns the applied values of stimulation thresholds. The network may come into practical use only when it has been trained and tested.

Wear of the blade, geometry of the blade, machine cutting conditions, material of the blade and the object processed as well as the relations between natural wear off and the value of the signal measured are very complex and, as mentioned above, rather of statistical than determined character [1, 2, 5, 7]. That is why on the basis of the literature analysis of diagnosis, it may be stated that the best model for diagnosing the machine cutting process are FFBP (Feed Forward Back Propagation) type neural networks.

## 3. Network models

In 1943, W. McCulloch and W. Pitts presented the first model of an artificial neuron. Their model included only four basic elements of the biological origin: dendrites, synapses, cell body and axon. Despite such big simplifications in comparison with the biological model, their model was widely applied in many neural network models [9].

The model of artificial neuron shown in Figure 1 in the form of bivalent threshold element is composed of the adder of weighted signals and the threshold system. Inputs receive signals coming from neurons of preceding layer. Each signal is multiplied by adequate numeric value connected with it and called a *weight*. It influences the perception of a given input signal and its share in generation of an output signal by the neuron. A weight may be stimulating (positive) or retarding (negative). If there is no connection between the neurons then the weight equals 0. Summed up products of signals and weights make the argument of the neuron activation function. The response of an artificial neuron to the input signals may be described by the following formula:

$$y_i = \sum_{i=1}^{n} (x_i \times w_i) - p_i, \tag{1}$$

where $x_i$ stands for the impulses coming from other neurons and $w_i$ stands for the weights of neurons susceptibility. The sum of products ($x_i \times w_i$) makes the weighted sum of the external influence.

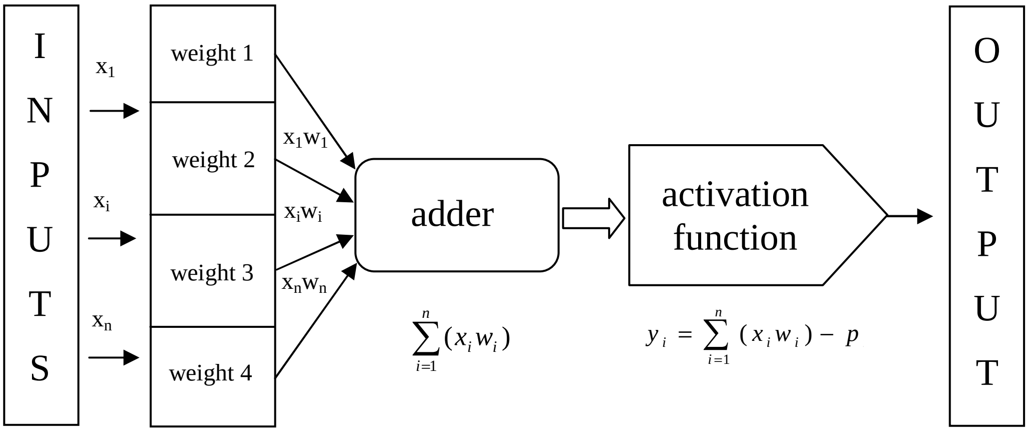

Fig. 1. Scheme of artificial neuron model's response to stimulating signals

In order to construct a neural network, neuron models are grouped in layers. Because of the training technique we distinguish between input, output and hidden layers. The system of neuron connections, their weights and stimulation thresholds make the network operation program.

The application of an adequate architecture poses a problem during designing such a network. If the network is too simple it may not be able to map adequate relations between the input and the output. But if the network is too compound it may be too sensitive and the dependence of a currently selected set of teaching data on network mapping will be too great.

The basic imperfection of this neural network model is that it does not have any feedback where an output signal $y_i$ may influence the susceptibility weights of the former layer neuron, which in turn may modify the output value $y_i$. For that reason examples known from the literature [7, 9] on the application of the neural networks to the solution of practical tasks in many cases worked slowly or gave trivial, formerly known, solutions.

## 4. Model of a network including a logical operator

Introduction of a feedback system into a simple neural networks model significantly extends the calculation time and presents a threat of "calculation looping" and hence it may disturb the operation of networks. When designing the network, additionally the following remarks should be taken into account:

• Signals collected by the measurement sensors are characterised by a certain dispersion spectrum.

• A set of input data may be a fuzzy set due to the inexact definition of the borders of the adherence of a given element to a set.

• A signal given to the adder's input may be estimated as improbable although it is true.

• A signal given to the adder's input may be faulty due to the fact of not tarrying readings or sensor's damage but it may be read in as probable.

Hence, starting from the basic rule of operation of a neural network with a logical operator "if–then" and bearing in mind all the above-mentioned properties of input signals, a new neuron model shown in Figure 2 has been put forward. It is composed of three operators realising various functions: an adder of weighted signals, a threshold element and a logical element [6].

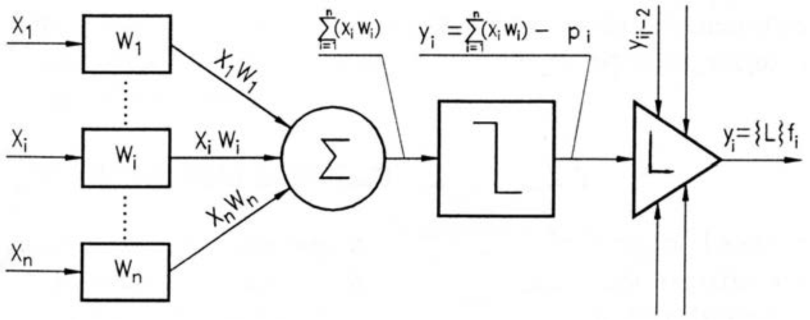

Fig. 2. Model of a neuron with a logical element [6]

In comparison to the neuron model shown in Figure 1, this model has also a logical operator that performs logical operations of checking out the correctness of network signals.

For an *i*-valued neuron in a *j*-valued layer of the neural network the weighted signals sum up in the adder ($x_i \times w_i$) together with the value of the stimulation threshold $p_i$ of this neuron, giving at the output a signal of the following value:

$$y_{ij} = \sum_{i=1}^{n} (x_{ij} \times w_{ij}) - p_{ij}\,. \tag{2}$$

A threshold element of this neuron establishes the value of the signal $y_{ij}$ on the level 0 or 1, according to the following rules:

$$y_{ij} = 0 \text{ when } y_{ij} \le 0, \qquad (3)$$
$$y_{ij} = 1 \text{ when } y_{ij} > 0.$$

In the neural network model including pseudo-operators, each neuron from a given layer is connected with all neurons from nearby layers. In addition, a signal from each neuron is transferred directly to the logical element of all neurons two layers further. The presence of an inter-layer signal transfer slightly blurs the borders between input, hidden and output layers. A necessary condition for a proper operation of such a network states that a given input layer is made of signals of the same sort, e.g., power or translocation.

Thanks to pseudo-logical operators we observe the control of signals introduced to the network in hidden layers, self-control of network's operation and interfered signals. A next important quality of such a network consists in high effectiveness of applying the basic teaching algorithms, e.g., error backward propagation algorithm. Due to inter-layer connection of neurons with pseudo-logical operator an "intelligent" data processing system was obtained in faraway layers. As early as at the learning stage, the system can point at errors that may appear in standard data sets used to train the network [6].

## 5. Application of the FFBP networks to supervise the machine cutting process

The use of neural networks of FFBP type is the basic method of processing the measuring signals in diagnostic systems based on the concept of an intelligent sensor and integration of measuring signals features. The analysis of mistakes, i.e., the differences between the calculated and expected values, and the tests showing the resistance to the interference determined have clearly indicated superiority of this network over other data processing methods.

In addition, an FFBP network may be trained along with oncoming data, which allows the model represented by network to be constantly improved [7].

Unfortunately, on practical industrial grounds the diagnostic systems using artificial intelligence methods often fail. It happens even when the neural network obtains data from sensors (it may be even a single measuring signal) which does not belong to the so-called training facts set. This causes taking up a wrong decision by the diagnostic system, as neural networks are the only calculation programs without logical operators.

This effect has been known for a long time and many methods have been tried out to eliminate this effect. They consisted in selecting an adequate architecture of the network, applying a "moving average" from three next signal values to the network or applying random interferences to the network [7].

The authors are of the opinion that one of the methods of increasing the reliability of diagnostic systems operation consists in working out a method of collecting measuring values of machine cutting forces, their initial processing and working out a manner of transferring them to programs of artificial neural networks applied in automatic diagnostic systems (ADS). In order to neutralize the influence of accidental changes of the analyzed signals not belonging to the set of training facts, the Institute of Machine Technology and Automation at Wrocław University of Technology carries out research on working out such a method of initial data preparation based on methods drawn from non-linear dynamics and fractal analysis. These works are mainly focused on shortening the neural network training time, increasing the calculation speed and shortening the network response inertness time (on-line mode operation).

Experimental research covers the dynamics of the machine cutting process as well as a non-linear character of the changes of measurable wear-off factors. The analysis covers mainly the signals from piezoelectric sensors measuring machine cutting forces. Data collection is carried out by means of an universal piezoelectric dynamometer of KISTLER type 9257A. In order to achieve a more detailed evaluation of the machine cutting process, also the signals from translocation sensors and thermal sensors are analyzed and compared with technological effects of machine cutting in real time (on-line).

The research also used some methods derived from the chaos theory. The sets of the component values of the machine cutting force obtained during collection of data regarding the supervised object have many features that are typical of fractals. Hence, the research covers correlations between the values established such as: fractal dimensions and envelope dimension of the amplitude with the average value and common relationship between machine cutting forces and tool's wear off. At present the research carried out focuses on working out a new method of gathering, in defined time spans, the components of machine cutting forces and applying them in appropriate packets (sets) together with other calculated values straight to the neural network. The application of this method in practice will be possible thanks to significant growth in calculation speed of modern computer technology.

## 6. Summary

On the basis of the analysis of accessible methods and the ways of diagnosing the machine cutting process, the FFBP type network has been selected for future research.

The way of this network's operation is most satisfactory and useful to build a system diagnosing the condition of a cutting tool.

The authors state that further research should be focussed on the following:

- dynamics of machine cutting process with particular attention paid to the process resistance to external interferences and correlation between dynamic values of the machine cutting force and the blade condition,
- finding out a critical roughness of the blade and forecasting the end of blade life,
- continuation of research into the methods of collection, initial preparation of the measured signals coming from measurement sensors and their application to the neural network.

## References

[1] Cichosz P., Kuzinowski M., Miernik M.: *Diagnozowanie stanu zużycia ostrza za pomocą sieci neuronowych*, II Forum prac badawczych – *Kształtowanie części maszyn*, Koszalin, 1996.

[2] Gawlik J., Karbowski K.: *Prognozowanie stanu ostrza skrawającego z zastosowaniem sieci neuronowych*, Mechanik, 1997, No. 4.

[3] Honczarenko J.: *Elastyczna automatyzacja wytwarzania – obrabiarki i systemy obróbkowe*, WNT, Warszawa, 2000

[4] Jemielniak K.: *Automatyczna diagnostyka stanu narzędzia i procesu skrawania*, Oficyna Wydawnicza Politechniki Warszawskiej, Warszawa, 2002.

[5] Knosala R.: *Zastosowanie metod sztucznej inteligencji w inżynierii produkcji*, WNT, Warszawa, 2002.

[6] Miernik M.: *Zastosowanie operatorów logicznych przy projektowaniu sieci neuronowych nadzorujących proces skrawania*, Raporty Instytutu Technologii Maszyn i Automatyzacji seria: Sprawozdania nr 21/95, Wrocław, 1995.

[7] Praca zbiorowa pod redakcją J. Kosmola.: *Monitorowanie ostrza skrawającego. Metody konwencjonalne i sieci neuronowe*, WNT, Warszawa, 1996.

[8] Praca zbiorowa pod redakcją J. Korbicza, J Kościelnego, Z. Kowalczuka, W. Cholewy: *Diagnostyka procesów. Modele, metody sztucznej inteligencji, zastosowania*, WNT, Warszawa, 2002.

[9] Tadeusiewicz R.: *Sieci neuronowe*, Akademicka Oficyna Wydawnicza RM, Warszawa, 1993.

[10] Miernik M.: *Application of neural networks for chip-type prediction in the turning of cobalt alloys*, European Journal of Mechanical and Environmental Engineering, 1997, Vol. 42, No. 2.

## Możliwości zastosowania sztucznych sieci neuronowych w automatycznych systemach diagnostycznych procesu skrawania

W artykule omówiono przyczyny zawodności współczesnych automatycznych systemów diagnostycznych pracujących na sieciach neuronowych w warunkach przemysłowych. Za jedną z podstawowych przyczyn uznano brak możliwości wykonywania operacji logicznych przez model sztucznego neuronu McCullocha i Pittsa, który stanowi jądro programów sztucznych sieci neuronowych. Zaprezentowano metodykę wstępnego przygotowania danych, opartą na metodach pochodzących z dynamiki nieliniowej, logiki rozmytej i teorii chaosu oraz sposoby przekazywania tak przygotowanych danych do sieci neuronowych typu *Feed Forward Back Propagation*.

ARCHIVES OF CIVIL AND MECHANICAL ENGINEERING

Vol. VI 2006 No. 4

# Attempt to estimate fire damage to concrete building structure

B. STAWISKI
Wrocław University of Technology, Wybrzeże Wyspiańskiego 25, 50-370 Wrocław

Depending on fire duration, fire temperature (reaching several hundred degrees centigrade) leads to a damage (in varying degrees) to concrete. A structural damage assessment based on an inspection is highly unreliable, particularly when concrete heated up during a fire was rapidly cooled down with cold fire-fighting water. Because of this thermal shock the surface of concrete cracks heavily. The load-bearing capacity of such a building component can be estimated based on the strength of the fire-damaged concrete and the thickness of the cracked layer. However, the temperature affecting the structure is different at different places and therefore the decrease anticipated in concrete strength is different in different elements and also varies within them. For this reason, among others, a building structure after a fire must be examined in many places in order to properly determine its technical condition. For *in situ* investigations nondestructive methods are most suitable. The example provided shows that such methods can successfully be used to test fire damaged concrete and reinforced-concrete structures.

Keywords: *buildings, failures, fire, concrete, tests*

## 1. Kinds of structural damage caused by fire temperature

If the changes in the temperature of a building's structural components do not exceed 100 °C, damage may only result from thermal deformations and the lack of proper expansion joints in the building. Other kinds of structural damage occur when temperature rises to a few hundred degrees centigrade [1]. In non-flammable (reinforced concrete, steel) structures, the hot elements bend (the hot layer lengthens) and if not properly reinforced, crack [7]. The expelling of water at fire temperature leads to serious damage to concrete. The problem received new attention after the recent tunnel fires when it was found that concrete with open pores (e.g., where the plastic fibre reinforcement used to be) was damaged to a lesser degree than concrete without such pores (and thus devoid of the routes of escape for steam from deeper layers during a rapid temperature rise up to a few hundred degrees). Rapid cooling with fire-fighting water results in intensive cracking [2]. Cracks, as well as their depth and width, affect the load-bearing capacity of structural components. Therefore, the cracks (their orientation, width and depth) should be examined in order to evaluate the technical condition of the structure.

During investigations of an underground garage in which several cars had burnt down, the ceiling reinforced-concrete slabs over the fire centre and its vicinity were found to be strongly cracked (Figure 1). Some of the fire protections came off the steel beams on which the ceiling slabs rest and the reinforced concrete columns cracked in the regions where they support the steel girders.

Fig. 1. Strongly cracked concrete in ceiling slabs over the centre of fire

Also the concrete walls devoid of anti-shrinkage reinforcement cracked. In order to answer several arising questions, ultrasound, sclerometric and deflection tests, crack width measurements and other investigations were carried out.

## 2. Nondestructive tests of concrete

### 2.1. Strength tests

Since the columns were 30 × 30 cm in cross section and contained reinforcement, no samples for nondestructive tests could be bored from them and no calibration curves could be determined from such samples. Therefore two nondestructive methods were employed to evaluate concrete strength. A Schmidt sclerometer and an ultrasound probe with standard 40 kHz heads were used for this purpose.

At the places tested plaster was removed, the humidity of the concrete was determined and sclerometric and ultrasound measurements were carried out. An NR Schmidt device and a calibration curve expressed by the following equation

$$f_c = 0.0418L^2 - 0.932L + 7.5\ \text{[MPa]} \tag{1}$$

were used for the sclerometric measurements.

A calibration curve represented by this equation

$$f_c = 0.1\exp 1.38V\ \text{[MPa]}, \tag{2}$$

where: $L$ – the rebound measured by the sclerometer, $V$ – the ultrasound impulse velocity [km/s], was used in the ultrasound measurements.

As expected, the results obtained show a wide scatter (Table 1).

Examining the results, one can notice distinct trends. For the columns tested the sclerometric method yielded results showing a large amount of scatter. But if one takes into account the fact that each of the four sides of a column was differently exposed to fire and temperature and to pouring on water, the drops in strengths clearly correspond to the sustained destructive loads. Also the varying humidity of the concrete contributed to the scatter. The sclerometer is less sensitive to concrete cracking. In the ultrasound method, the opposite is true: marked drops in ultrasound velocity are registered in cracked areas. No readings are obtained in the direction perpendicular to the cracked plane. Zones on the fire side show lower impulse velocities, and so lower strengths. The two methods consistently indicate that the columns' upper parts are much weaker than their lower parts (Figure 2). This corresponds to the fact that during a fire the temperature is higher under the ceiling than near the floor.

Table 1. Summary of average concrete strengths $\bar{f}$ for a given height, determined on three surfaces for selected pillars at various distances from the fire source

| Column no. | Distance from floor [cm] | Sclerometric investigations | | Ultrasound investigations | | | |
|---|---|---|---|---|---|---|---|
| | | Direct exposure* [MPa] | Hidden exposure** [MPa] | Direct exposure* [MPa] | Hidden exposure** [MPa] | | |
| 3 | 180 | 11.8 | 18.3 | 6.4 | 9.2 | 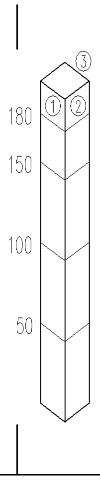 | $\bar{f}_{180} = \frac{f_1 + f_2 + f_3}{3}$<br>$\bar{f}_{150} = \frac{f_1 + f_2 + f_3}{3}$<br>$\bar{f}_{100}$<br>$\bar{f}_{50}$ |
| | 150 | 16.9 | 24.8 | 14.0 | 13.1 | | |
| | 100 | 21.1 | 25.6 | 12.6 | 15.9 | | |
| | 50 | 29.4 | 26.1 | 17.1 | 18.6 | | |
| 4 | 180 | 11.1 | 12.7 | – | | | |
| | 150 | 14.7 | 16.6 | 10.8 | | | |
| | 100 | 19.0 | 14.3 | 13.7 | | | |
| | 50 | 21.1 | 18.7 | 17.8 | | | |
| 11 | 180 | 15.7 | 11.3 | – | | | |
| | 150 | 40.3 | 28.2 | 21.5 | | | |
| | 100 | 37.8 | 26.4 | 21.5 | | | |
| | 50 | 38.3 | 26.8 | 21.6 | | | |

* Surfaces exposed to a direct fire.

** Surfaces shielded from a direct fire.

High fire temperature is the cause of larger deformations, stresses, thermal cracks, warping, etc. [3]. The severity of the effects of a fire is determined by the temperature to which the structure is heated up and the duration of the fire. It is assumed that the strength of steel begins to decrease above 350–400 °C. At a temperature of 500 °C the drop in strength amounts to 30–40%, at 600 °C to 50% and so on [4]. When temperature falls back to 20 °C, the one-time holding of 34GS and 18G2 grade steel at a temperature of 600 °C for 1–3 hours does not result in a lower ultimate strength. Only temperature higher than 600 °C results in a permanent strength reduction [3].

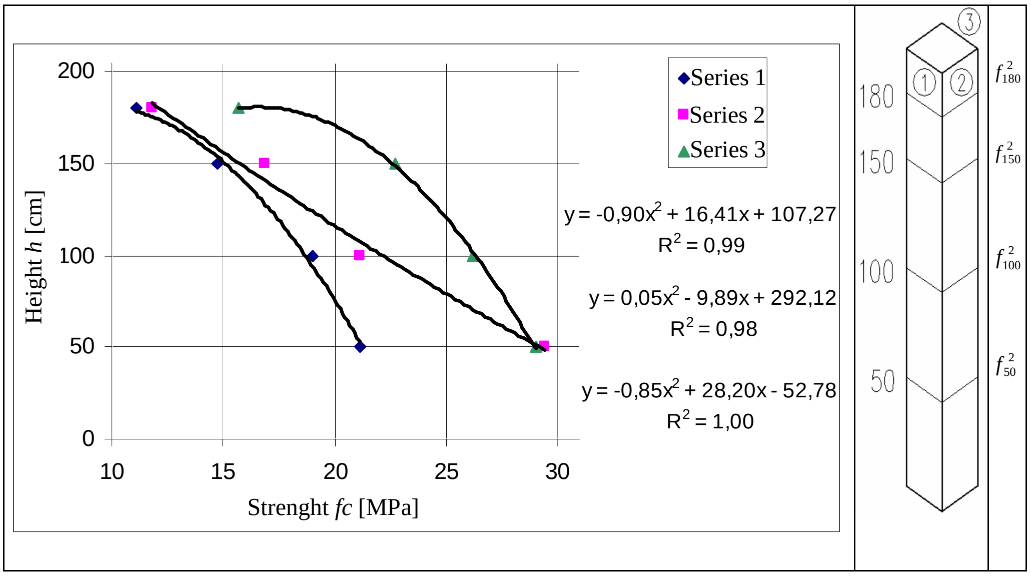

Fig. 2. Concrete strength $f^2$ determined for various heights of selected pillars only on one surface no. 2 with similar exposure to that of the fire source

In the case of reinforced concrete, the influence of temperature should be considered separately for steel, concrete and the interaction between both. As temperature and the time of its influence on concrete increase, the utility of the concrete and the reinforced concrete decreases [5] due to the following processes:

- the evaporation of chemically bound water at a temperature up to 100 °C,
- the dehydratation of the cement binder at a temperature of 400 °C and above,
- the decarbonation of the binder at a temperature of about 700 °C,
- thermal deformations of the aggregate minerals and of the reinforcing steel.

If water evaporates rapidly, this can result in a network of cracks [3]. Also rapid changes in temperature (e.g., when pouring on water) lead to concrete cracking and failure [5]. Different drops in strength are reported. For example, Nevile [5] quotes after other researchers that when concrete is heated up to 200 °C, 400 °C and 600 °C its strength decreases by 50–92%, 45–83% and 45–83%, respectively. This indicates that research on the strength of concrete in a structure after a fire is vitally necessary. The data reported so far in the literature should be regarded as approximate.

The literature data on the velocity at which temperature spreads in concrete and in steel enclosed in concrete are more definitive. The concrete which covers the steel protects it from high temperatures. At a constant ambient temperature of 1000–1100 °C the reinforcement in reinforced concrete heats up to about 550 °C during one hour if the concrete cover is 2.5 mm thick and if the latter is 5 cm thick the reinforcement heats up to this temperature within two hours [3]. Up to a temperature of 300 °C adhesion of smooth steel to concrete does not decrease and in the case of ribbed steel, no decrease in its adhesion to concrete is observed up to a temperature of 350 °C.

## 2.2. Other nondestructive investigations of structure after fire

Concrete humidity was measured using a UNI-2 gauge with an active B-50 ball probe. Humidity varied from 1.0% to 4.5% between different levels and areas of the columns. The influence of concrete moisture on ultrasound velocity and Schmidt sclerometer rebound was taken into account in the strength tests.

Geodetic measurements of the deflection of the concreted steel beams and the ceiling slabs located over the burning cars were carried out (Table 2). The deflections permissible for the slabs in the garage were calculated as for l/150 (512/150 = 3.4 cm) secondary elements.

Table 2. Deflections of steal beams and reinforced-concrete ceiling slabs resting on them, calculated from measurements

| Element no. | Deflections [cm] | | | $a_{\max}$ [cm] | Permissible deflection [cm] |
|---|---|---|---|---|---|
| | ¼ of span $a_2$ | ½ of span $a_3$ | ¾ of span $a_4$ | | |
| Beam U1 | 0.8 | 1.1 | 0 | 1.1 | 3.0 |
| Beam U2 | 0.8 | 0.8 | 0.3 | 0.8 | 2.8 |
| Beam U3 | 0.4 | 1.3 | 1.0 | 1.3 | 2.8 |
| Beam U4 | 3.0 | 4.1 | 3.2 | 4.1 | 3.4* |
| Beam U5 | 3.0 | 3.8 | 2.8 | 3.8 | 3.4* |
| Beam U6 | 3.5 | 4.5 | 3.4 | 4.5 | 3.4* |

Fig. 3. Verification of crack depth in shallow borehole (towards reinforcement)

As can be seen, the deflections of the fire-protected steel beams are smaller, whereas those of the strongly cracked reinforced concrete slabs are larger than the permissible ones. The temperature of the structural components during the fire was estimated at 300–350 °C (the colour of the concrete was natural [6]). At a temperature of 350 °C the thermal creep of steel begins. This led to ceiling slab deflections larger than the permissible ones.

The ultrasound crack depth measurements were verified by means of shallow boreholes (Figure 3). The depth of cracks reaches 1.5 cm (sometimes 2.0 cm) towards the reinforcement.

## 2.3. Repair work

After the fire some the investigated building's components needed repairing. The columns within a radius of 10 m from the fire source were strengthened since the strength tests had shown a serious reduction in strength in their upper parts. Also oblique cracks under the columns' heads had appeared. The fire protections on the steel beams whose ends rest on the columns had to be repaired. The cracked concrete in the ceiling slabs lost only its corrosion protection properties. The reduced strength in the tensile zone did not affect the load-bearing capacity of the slabs. The ceiling slabs were protected from below merely against carbon dioxide penetration and carbonatisation advance. The steel's estimated temperature (300–350 °C) and its dwell time at this temperature did not contribute to deterioration of its strength properties after cooling down. To sum up, the inferences and the ways of repair should be based on a thorough examination and analysis of the cracks, their pattern and width.

## References

[1] Stawiski B.: *The Use of Nondestructive Methods in Postfire Diagnostics* (in Polish), KKBN, Zakopane, 2005.
[2] Grabiec T.: *Reconstruction of Ackermann Floor after Fire* (in Polish), The 13th Symposium on Determination of Causes and Prevention of Failures, Szczecin, 1992.
[3] Kosiorek M. et al.: *Fire Resistance of Concrete Structures* (in Polish), Arkady, Warsaw, 1988.
[4] Grabiec K.: *Effect of Fire Temperatures on Safety of Building Structures* (in Polish), Przegląd Budowlany, 1987, 10.
[5] Neville A.M.: *Properties of Concrete* (in Polish), Polski Cement Sp. z o.o., Cracow, 1995.
[6] Jarmontowicz. A., Krzywobłocka-Laurow R.: *Guidelines for Estimating Post-heat Concrete Temperature on the Basis of Laboratory Tests* (in Polish), ITB, Warsaw, 1986.
[7] EN 1992-1-2: 2004 Eurocode 2: *Design of concrete structures* – Part 1–2 *General rules – structural fire design*.

## Próba rozpoznania uszkodzeń betonowej konstrukcji budynku po pożarze

Temperatura pożarowa sięgająca kilkuset stopni Celsjusza w zależności od czasu trwania pożaru prowadzi do uszkodzeń betonu w bardzo różnym stopniu. Ocena uszkodzenia konstrukcji na podstawie oględzin jest bardzo niepewna, szczególnie gdy beton nagrzewany w czasie pożaru został gwałtownie schłodzony zimną wodą używaną do gaszenia ognia. Przy takim szoku termicznym powierzchnia betonu ulega silnemu spękaniu. Nośność takiego spękanego betonowego komponentu budowlanego można szacować, opierając się na wytrzymałości uszkodzonego betonu po pożarze i grubości warstwy spękanej. Na ogół jednak temperatura działająca na konstrukcję jest różna w różnych miejscach, a w związku z tym spodziewane pogorszenie się wytrzymałości betonu będzie różne w różnych elementach, a nawet w ich częściach. Między innymi z tego względu obiekt budowlany po pożarze wymaga badań w wielu miejscach, aby można było dobrze określić jego stan techniczny. Do badań in situ najlepsze są metody nieniszczące. Na prezentowanym przykładzie pokazano, że metody te mogą być z powodzeniem wykorzystane również do badania konstrukcji betonowych i żelbetowych po pożarze.

ARCHIVES OF CIVIL AND MECHANICAL ENGINEERING

Vol. VI 2006 No. 4

# Fatigue life of reinforced concrete beams under bending strengthened with composite materials

W. DERKOWSKI
Cracow University of Technology, ul. Warszawska 24, 31-155 Kraków

The present paper focuses on the problem of the durability of bent RC beams strengthened with composite materials, subjected to cyclic loading. The theoretical model of determining fatigue life of the cross-section of the bent reinforced concrete beam strengthened with external, non-stressed CFRP strips is presented. The author's own proposal is to introduce the coefficient of the strip position effect on each individual bar and a way of taking into account the energy absorbed by the strengthening. The energy causes a decrease in the velocity of the crack propagation in the rebar, and consequently, an increase in its durability.

The theoretical model was verified in the experiments carried out on two series of reinforced concrete beams with different steel and strengthening ratios. For each group of the beams the value of fatigue load was matched to get similar stress in the tension bars.

**Keywords:** *fatigue life, strengthening, composite, CFRP, reinforced concrete, model, research*

## 1. Introduction

The strengthening of reinforced concrete structures is and will continue to be a relevant problem due to a continuous increase in live loads as well as corrosion and stress destruction. Rapid progress in the development of strengthening materials and technologies has been made in the last decades [1].

Since structures are being designed with the application of more and more precise calculating methods, using strength design values in the most stressed cross-sections which approach characteristic ones, and with an increase in the ratio of live to total loads, the fatigue strength and correlated fatigue life should not be neglected in the analysis of many structures – especially those of bridges.

The present paper focuses on the problem of the durability of a normal cross-section of bent reinforced concrete beams strengthened with non-stressed carbon fibre strips, subjected to cyclic loading.

Until now the number of tests carried out on reinforced concrete beams strengthened with composite laminates subjected to a fatigue load has been comparatively smaller than the number of such beams tested under a static load. In an available literature, there is no theoretical model for the fatigue life of a cross-section of bent RC beams strengthened with FRP strips. Analyzing the behaviour of non-strengthened and strengthened RC beams with non-stressed CFRP (Carbon Fibre Reinforced Polymers) laminates under the bending moment of the same magnitude, one can observe:

- a decrease in stresses in the reinforcing steel due to an increase in the amount of the tensile reinforcement which implies a rise in the fatigue life of the steel,
- enlargement of the internal arm of the resultant forces and, consequently, a decrease in the stresses in the compressed concrete and a rise in the fatigue life of the concrete.

As a result of the above, there is an increase in the fatigue life of the whole cross-section of strengthened beam in comparison to the fatigue life of non-strengthened one.

Additionally, according to Barnes and Mays [2], Heffernan [3] and my own research [4], even when increasing the live loads to the level at which the same stresses in the tension reinforcement are obtained, there is an increase in the fatigue life of the rebars of strengthened beam in comparison with the fatigue life of non-strengthened one.

## 2. Proposal of theoretical fatigue life model of bent RC cross-section strengthened with CFRP strips

Determination of fatigue life for a RC cross-section strengthened with CFRP laminates ($N_f$) is equal to the calculation of the smallest number of cycles after which the fracture of at least one of the following component materials may occur: concrete in the compression zone ($N_{f.c}$), reinforcing steel ($N_{f.s}$), CFRP laminate ($N_{f.f}$) or adhesive layer ($N_{f.a}$):

$$N_f = \min(N_{f.c}, N_{f.s}, N_{f.f}, N_{f.a}). \tag{1}$$

While designing the strengthening of bent RC structures by means of non-stressed CFRP strips, the maximum effort of composite material is low (the average level is about 0.2–0.4 of its tensile strength), so the fatigue life of this material is practically unlimited. According to FIB [5] regulations, fatigue strength of epoxy resin glues may be taken at the level of 50% of their static strength. Because tensile and shear strength of glue are over twice as great as these values for concrete cover, it may be stated that the delamination of the composite material never takes place within the layer of glue. In such a situation, Equation (1) is limited only to two terms relative to fatigue of concrete in compression and steel rebars in tension:

$$N_f = \min(N_{f.c}, N_{f.s}). \tag{2}$$

### 2.1. Computational assumptions

The theoretical model proposed is based on the following assumptions:

A. Maximum and minimum stresses in a load cycle, in strengthened cross-section, should be calculated taking into account:

- the changes in the geometric characteristics of the analyzed cross-section (an increase in cross-section area and moment of inertia, lowering the gravity centre),
- existing strain and stress states in the analyzed cross-section at the time of strengthening (with attention paid to element cracking, loads acting at the time of strengthening, the influence of concrete shrinkage and creep).

B. The number of repeated load cycles ($N_{f.c}$), which lead to the fatigue fracture of concrete in compression, is determined on the basis of the Aas–Jacobsen formula modified in 1979 by Tepfers and Kutti [6]:

$$\log N_{f.c} = \frac{1 - S_{\max}}{0.0685(1 - R)}. \tag{3}$$

C. Fatigue life of reinforcing steel in a strengthened beam is evaluated on the basis of fracture mechanics, using Paris Crack Propagation Law [7]. The propagation velocity of the crack of a length *a* is given by a function of the gain in stress intensity factor $\Delta K$, in the exponential form (4). The values of *C* and *m* are the material constants, established in tests (the constants *C* and *m* for the reinforcing rebars are given in [8]).

$$\frac{da}{dN} = C(\Delta K)^m. \tag{4}$$

D. The stress intensity factor *K* in the fracture process zone, in the front of the crack, for the ribbed reinforcing bar of a diameter *ø* in a reinforced concrete beam is determined on the basis of the formula given by Salah El Din and Lovegrove in 1982 [9]:

$$K = 0.886\, k_t \sigma_t \sqrt{\pi a}\, \alpha\left(\frac{a}{\phi}\right) f_b\left(\frac{a}{\phi}\right) \left[ f_t\left(\frac{a}{\phi}\right) + 0.76 \frac{\phi}{2 d_s \left(1 - \frac{x}{d_s}\right)} \right], \tag{5}$$

where:

$k_t$ – the parameter dependent on rebar geometry,

$\sigma_t$ – the tensile stress in rebar,

$\alpha\left(\frac{a}{\phi}\right)$ – the function of decay stress concentration,

$f_b\left(\frac{a}{\phi}\right)$ – the function of the concrete cover effect on the stress in the fatigue crack front region,

$f_t\left(\frac{a}{\phi}\right)$ – the function of the crack length effect on stress intensity,

$d_s$ – the effective depth of cross-section,

$x$ – the depth of cross-section compression zone.

## 2.2. Fatigue life of rebar in RC cross-section strengthened with CFRP strips

Fatigue life of the reinforcing bars embedded in the RC beam strengthened with non-stressed CFRP strips ($N_{f.s}$) is evaluated based on a transformed Paris Law formula (6). In calculations, only the first fracture mode (Mode I) is assumed:

$$N_{f.s} = N_0 + \int_{a_0}^{a_{\max}} \frac{1}{C \cdot \left(\Delta K_{\mathrm{I.str}}\right)^m} da, \tag{6}$$

where:

$N_0$ – the number of stress cycles required to form a crack of the size $a_0$,

$a_0$ – an initial crack length,

$a_{\max}$ – a maximal, final crack length,

$\Delta K_{\mathrm{I.str}}$ – the gain in stress intensity factor calculated for the rebar situated in the strengthened beam that allows the influence of work of the carbon fibre laminate on the stress field at the crack tip.

In fracture mechanics, the square of stress intensity factor is presented as a product of the modulus of elasticity and the integral $J$. The integral $J$ represents a change in the potential energy required to create a unit crack growth [10]. Thus, for the strengthened beam the following equation can be written:

$$K_{\mathrm{I,str}}^2 = E_s J_{\mathrm{str}}, \quad \Rightarrow \quad K_{\mathrm{I,str}} = \sqrt{E_s J_{\mathrm{str}}}. \tag{7}$$

In the case of beam strengthened with CFRP laminates, the integral $J_{\mathrm{str}}$ should take into account the work (energy) absorbed by the strengthening strips, for crack area and for elementary increment of crack opening:

$$J_{\mathrm{str}} = J_s - \overline{W_{FRP}}, \tag{8}$$

where the integral $J_s$ is evaluated for the non-strengthened reinforced concrete element on the basis of the value of stress intensity factor $K$ (formula (5)).

CFRP laminate work fraction in a potential energy $J_{\mathrm{str}}$ should be determined for each glued strip separately. When the strengthening is made of a few composite strips, the rule of superposition of the energy $W_{FRP}$ is adopted. For an individual strip the energy $W_{FRP}$ is calculated:

$$W_{FRP} = \frac{\zeta \cdot F_{FRP} \cdot \Delta u}{\Delta A_{sc}}, \tag{9}$$

where:

$\zeta$ – the coefficient of strip position effect,

$F_{FRP}$ – a tensile force transferred by the effective part of strip,

$\Delta u$ – an increase in crack opening corresponding to the increase in its length,

$\Delta A_{sc}$ – an increase in crack area corresponding to the increase in its length $\Delta a$.

The coefficient $\zeta$ results from the position of the strip relative to the individual bar. The value of $\zeta$ is calculated as follows:

$$\zeta = 0.25 \cdot \omega \cdot \lambda, \tag{10}$$

where $\omega$ is the coefficient which takes into account the distance from the laminate to the bar surface (in the direction perpendicular to the strip surface):

$$\omega = \frac{h_{\mathrm{eff}} - a_c}{h_{\mathrm{eff}}}, \tag{11}$$

where:

$h_{\mathrm{eff}}$ – the depth of the effective tension area of the reinforced concrete cross-section,

$\lambda$ – the coefficient which takes into account the localization of the strip relative to each individual rebar.

It is assumed that the range of the influence of the laminate spreads from the edge of the strip to the interior of the beam, at an angle of 45° (angle of stress spreading in reinforced concrete). The area of the effect for the individual rebar $A_{\mathrm{cos}}$ is determined based on the same assumption. The area $A_{\mathrm{cos}}$ is a right angle of triangle with its vertex in a centre of the rebar. The coefficient $\lambda$ expresses the ratio of this part of the area $A_{\mathrm{cos}}$ which is placed within the influence of the laminate to the whole area $A_{\mathrm{cos}}$. An example of the way of determining the coefficient $\lambda$ for rebars embedded in the beams strengthened with one or two strips is shown in Figure 1.

The tensile force transferred by the effective part of the strip is expressed by:

$$F_{FRP} = b_{FRP,\mathrm{eff}} \cdot t_{FRP} \cdot \sigma_{FRP}, \tag{12}$$

where:

$b_{FRP,\mathrm{eff}}$ – an effective width of the laminate which may affect the rebar durability,

$a_s$ – the distance between the centre of gravity of the rebar and strengthened edge of cross-section,

$t_a$ – the thickness of the adhesive layer (glue),

$b_{FRP}$ – the width of the FRP strip,

$t_{FRP}$ – the thickness of the FRP strip,

$\sigma_{FRP}$ – the tensile stress in the FRP strip.

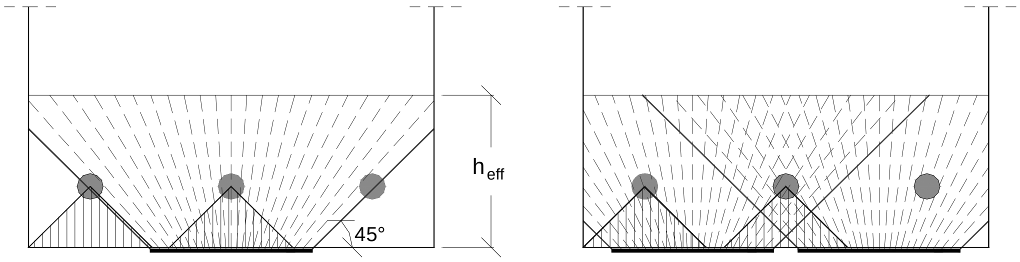

Fig. 1. Determination of the coefficient λ

An increase in the crack opening $\Delta u$ corresponding to the elementary increase in its length $\Delta a$ is determined in the following way:

$$u = \frac{2a}{E\sqrt{\pi a}} K_{I.s}.$$

## 3. Experimental verification of theoretical model

Experimental tests were carried out at a research laboratory of the Institute of Building Materials and Structures at Cracow University of Technology. A scheme of the special test stand is presented in Figure 2. The beams were loaded by the means of electronically controlled hydraulic pulsator from Instron Schenck Testing Systems Company.

Eight simply supported beams were tested. For all the beams the following geometric parameters were constant:

- rectangular cross-section, dimensions: $h$ = 40 cm, $b$ = 25 cm,
- total length of beam $l$ = 3.50 m,
- beams were simply supported over a 3.20 m span,
- three cracks were formed in the central part of the beam by placing small pieces of zinc plated steel sheet across a full width of the beam, before casting the concrete; the initiators were welded to the stirrups, spaced in the distance of 80% of medium calculated crack spacing.

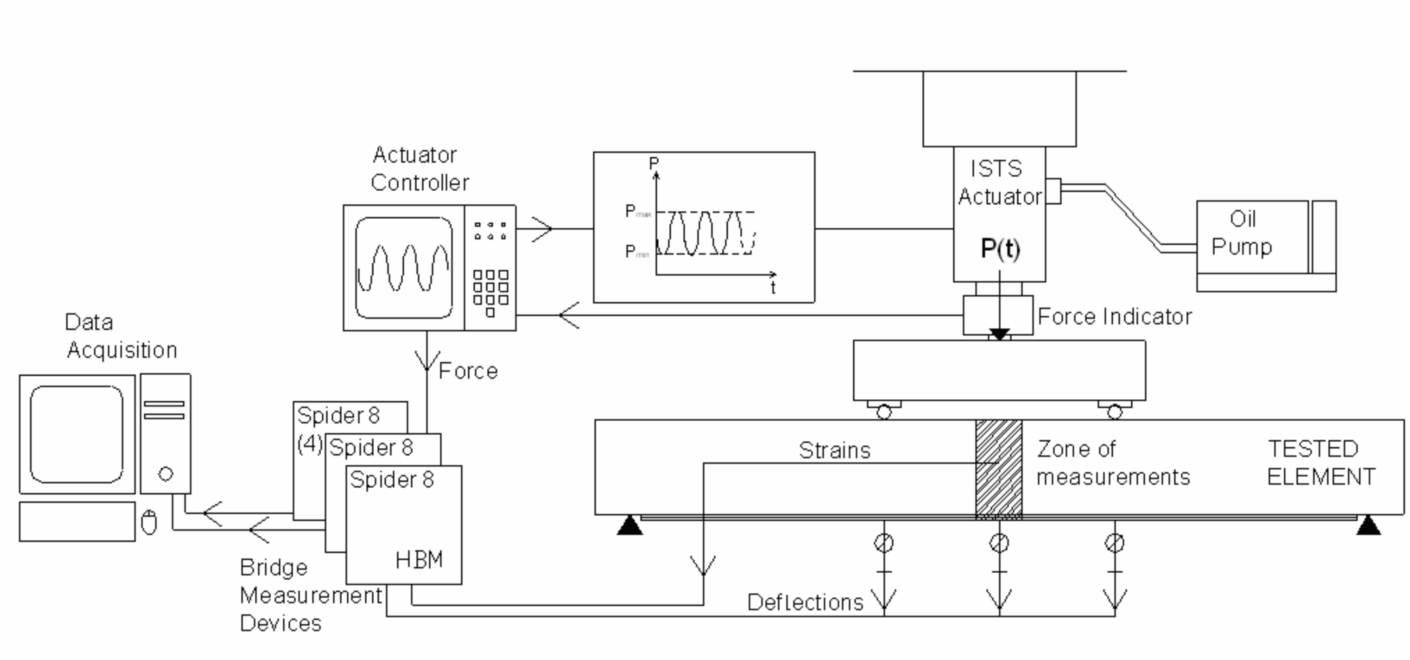

Fig. 2. Scheme of test stand

The reinforcement of the elements tested was designed so as to make it possible to run a comparative analysis of beams of the same reinforcement ratio $\mu_s$ and $\mu_{FRP}$, and strengthening ratio $\rho_{FRP} = \mu_{FRP} E_{FRP} / \mu_s E_s$ (see Table 1).

Table 1. Basic parameters of the beams tested

| | Beams denotation | $\mu_s$ [%] | $\mu_{FRP}$ [%] | $\rho_{FRP}$ [-] |
|---|---|---|---|---|
| Control beams | P1-0.1 | 0.67 | 0.00 | 0.00 |
| | P1-0.2 | 0.67 | 0.00 | 0.00 |
| Series P1 | P1-0 | 0.67 | 0.00 | 0.00 |
| | P1-1 | 0.67 | 0.12 | 0.16 |
| | P1-2 | 0.67 | 0.24 | 0.32 |
| Series P2 | P2-0 | 1.38 | 0.00 | 0.00 |
| | P2-1 | 1.38 | 0.12 | 0.08 |
| | P2-2 | 1.38 | 0.24 | 0.16 |

The longitudinal reinforcement was made from the steel grade 34GS (the yield strength tested $f_y$ = 430 MPa). The beams were precast with two types of tension reinforcement: type P1 reinforced with three # 16 mm bottom rebars and type P2 reinforced with four # 20 mm bottom rebars.

The transverse reinforcement was made from steel grade RB500W (design yield strength $f_{yd}$ = 500 MPa) and the amount of stirrups was selected so as to ensure a flexural failure of the beam.

The bottom face of the beam was prepared for the strengthening by sand blasting. The strengthening system (external reinforcement) consisted of one or two CFRP strips (SikaCarboDur S1012) glued on a two-part cold curing paste epoxy SikaDur-30. Additionally, in shear zones of the beams (between the load point and the end of the strip), one layer of CFRP sheet (SikaWrap 230C) was glued on SikaDur-330 in order to improve the anchorage of the strips. The direction of the sheet fibres was perpendicular to the beam axis. The sheets were wrapped around bottom and side faces of the beam.

Two non-strengthened beams (P1-0.1 and P1-0.2) were tested in the preliminary phase of the research. The goal of these control tests was to determine the fatigue life for beams under a different level of cyclic load and based on this determination to calibrate main parameters of a final research programme. The essential tests were carried out on two series of three reinforced concrete beams each. The elements tested, steel ratio $\mu_s$, CFRP laminate ratio $\mu_{FRP}$ and the beam strengthening ratio $\rho_{FRP}$ have been tabulated in Table 1.

The beams were loaded with two equal concentrated forces at the points located 110 cm from the support. Before the fatigue test, each beam was cracked under a static load, equal to the medium value of the planned cyclic loading. Strengthened beams were precracked before gluing the CFRP laminates.

Cyclic loading was programmed with the following assumptions:

- the value of maximum and minimum forces in a load cycle was constant during the whole beam test,
- the load wave shape: sine,
- the load frequency: 1.5 Hz,
- for each group of the beams the values of forces were selected so as to obtain similar stresses in the rebars under tension.

A loading plan was determined in such a way as to obtain the results that allow an analysis of the effect of strengthening with CFRP laminates on fatigue life of the elements tested. By adopting the normal load ranges experienced by bridge structures (according to load codes) for the test beams, the stress ranges in steel reinforcement would be well below their endurance limit. To ensure that fracture of the rebar occurs, it was necessary for the stress range to be sufficiently high, so as to ensure failure of the members after a practical number of load cycles.

The final value of maximum and minimum forces of cyclic load was determined in the first cycles of fatigue load on the basis of measured strain of steel reinforcement in a crack cross-section.

Data acquisition (the values of strains, deflections, external force and the number of load cycles) was carried out with an electronic measuring apparatus, composed of three bridge measurement devices SPIDER 8 connected with PC (with CATMAN 3.0 software). This apparatus allows the simultaneous recording of data from 20 channels, with measurement rate equal to 300 Hz. All the measurements were taken within 6 second periods of time. During the first 40,000 cycles in the last part of the test, measurements were taken every 15 minutes (1350 cycles). In the middle part of test, measurements were taken every 2 hours (10,800 cycles). In the last part of the test, when an increase in measured values was observed, measurements were taken as often as possible. The tests were carried out continuously up to the point of beam failure.

The strains were measured by foil electric resistance strain gauges placed in two cross-sections: middle crack cross-section and cross-section between the initiated cracks. 60 mm length extensometers were used for concrete strain measurements and 5 mm length ones were used for steel and CFRP strips. The strain gauges were placed at the middle crack cross-section and the cross-section between the initiated cracks.

The deflections were recorded with three linear voltage displacement transducers located at the midspan of the beam and under the load forces.

## 4. The analysis of experiments and the results of theoretical calculations

Maximum and minimum stresses as well as the range of stress in the tensile reinforcement steel (bottom rebars) for the beams tested within the fatigue load are presented in Table 2. The effort of the tension reinforcing bars (stress related to the measured yielding point of steel) is also given in Table 2.

Table 2. Stress and effort of reinforcing bars in tension in the beams tested

| | | P1-0 | P1-1 | P1-2 | P2-0 | P2-1 | P2-2 |
|---|---|---|---|---|---|---|---|
| $\sigma_{s,\min}$ | [MPa] | 64 | 65 | 56 | 40 | 51 | 52 |
| | [% of $f_y$] | 15 | 15 | 13 | 10 | 12 | 12 |
| $\sigma_{s,\max}$ | [MPa] | 327 | 330 | 326 | 294 | 306 | 313 |
| | [% of $f_y$] | 75 | 76 | 75 | 70 | 73 | 74 |
| $\Delta\sigma_s$ | [MPa] | 263 | 265 | 270 | 254 | 255 | 261 |
| | [% of $f_y$] | 60 | 61 | 62 | 60 | 61 | 62 |

In any of the elements tested, the fatigue fracture of composite material or adhesive layer has been observed. The failure of all the beams tested was always initiated by the brittle fatigue fracture of reinforcing steel. The fracture initiation site on the individual rebar is usually located in the region of the intersection of longitudinal and transverse ribs. This is the result of local stress concentration at the place of sudden change of bar geometry (notch effect). A view of the crack in the side rebar, which was cut out on the beam P2-1 after the test, is shown in Figure 3.

Fig. 3. Fatigue crack in side rebar of beam P2-1

The numbers of cycles to fatigue fracture of individual reinforcing bars in each tested beam of the series P1 and P2 are presented in Tables 3 and 4, respectively. The rebars are numbered in the sequence from one edge side to other. Additionally, in Tables 3 and 4 the number of cycles to beam failure with the description of failure mode are given.

Table 3. Fatigue life of the beams of series P1

| Rebar number | P1-0 | P1-1 | P1-2 |
|---|---|---|---|
| 1 | 286.885 | 374.288 | 659.595 |
| 2 | – | 390.775 | 662.338 |
| 3 | – | 390.150 | 661.905 |
| | | 390.780<br>(debonding of CFRP) | 663.400<br>(concrete crushing) |

Table 4. Fatigue life of the beams of series P2

| Rebar number | P2-0 | P2-1 | P2-2 |
|---|---|---|---|
| 1 | 446.100 | 443.000 | 459.100 |
| 2 | – | 457.808 | – |
| 3 | – | – | 478.980<br>480.730 |
| 4 | – | 450.550 | 482.114 |
|  |  | 457.808 (concrete crushing, debonding of CFRP) | 482.114 (concrete crushing, debonding of CFRP) |

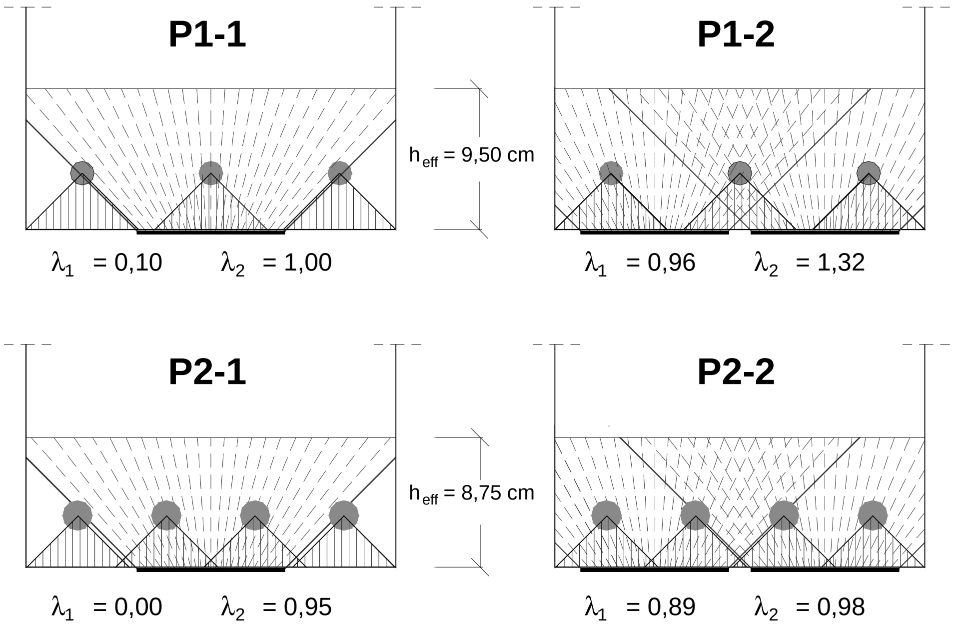

Fig. 4. Range of the influence of strips on individual rebars

The experiments showed that in the beams strengthened with one central strip, side rebars (situated outside of the outline of the strip) fractured earlier than the central ones. In both beams strengthened with two strips, one of the central rebars was not destroyed (the rebar No. 3 in the beam P2-1 and No. 2 in the beam P2-2). Such a behaviour is due to a limited influence of the laminates on improving work conditions of different rebars.

In the author's theoretical model, the limitation of the effect of the laminate is included in the coefficient of the strip position effect ($\zeta$). The coefficient $\zeta$ is the function of the coefficient $\lambda$, taking into consideration the strip position related to an individual rebar (see Equation (10)). The range of the influence of the CFRP laminate and the values of the coefficient $\lambda$ on the side rebar ($\lambda_1$) and central rebar ($\lambda_2$) in all the elements tested are given in Figure 4. As shown in Figure 4, side rebars of the beam P2-1 are located outside the influence of strips ($\lambda_1 = 0$). Only in the beam P2-2 were all the bars under almost identical influence of strengthening laminates ($\lambda_1$ and $\lambda_2$ values are close to each other).

The percentage of an increase in fatigue life obtained in research related to beam strengthening ratio $\rho_{FRP}$ is presented in Table 5. The numbers in brackets are related to the real range of stresses in the reinforcing bars in each beam – this correction was done using the Corley formula [11]. This formula was chosen due to positive convergence of calculations with experimental results.

Table 5. Increase in the fatigue life of strengthened beams

| Series | Beam strengthening ratio $\rho_{FRP}$ | | |
|---|---|---|---|
| | 0.08 | 0.16 | 0.32 |
| Series P1 | – | P1-1<br>30% (33%) | P1-2<br>130% (136%) |
| Series P2 | P2-1<br>–1% (5%) | P2-2<br>3% (17%) | – |

The graphic comparison of the beam lives tested and calculated is presented in Figure 5, whereas the safety margins obtained (in percentages) are shown in Table 6. The positive notation means that the tested life of the beam was longer than the calculated one.

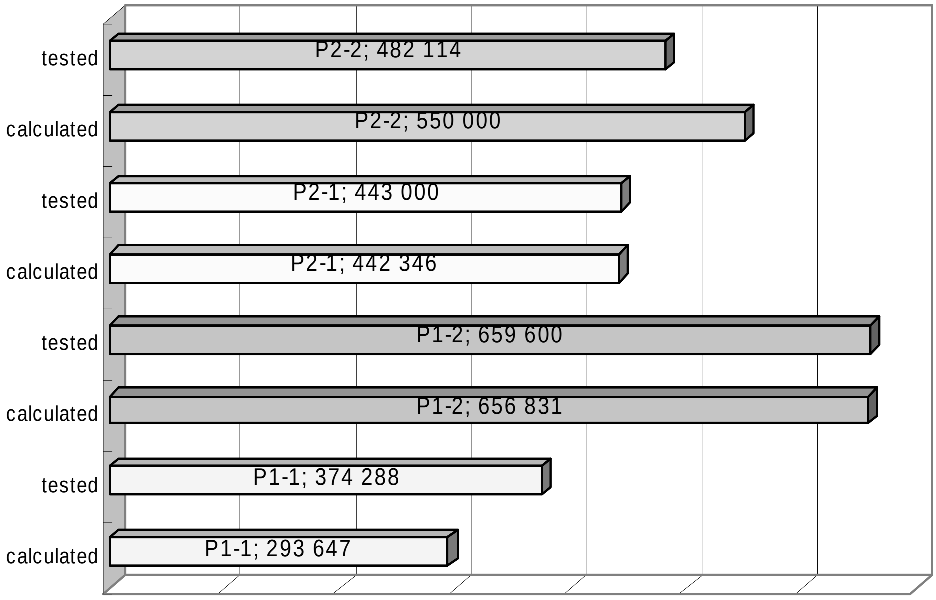

Fig. 5. Comparison of the beams life tested and calculated

Table 6. Comparison of the beams lives tested and calculated

| | P1-1 | P1-2 | P2-1 | P2-2 |
|---|---|---|---|---|
| The safety margin obtained | 21.5 % | 0.4 % | 0.1 % | –14.1 % |

## 5. Conclusions

The author's own theoretical model for determining the fatigue life of the cross-section of the bent reinforced concrete beam strengthened with external, non-stressed carbon fibre strips is presented. The estimation of durability of concrete is based on the Aas–Jacobsen formula modified by Tepfers and Kutti. The essential part of this model is the evaluation of the fatigue life of the rebar, for which the influence of the strengthening is the slightest. This is done on the basis of fracture mechanics, using Paris Crack Propagation Law, including the influence of the work of the carbon fibre laminate on the stress field in the crack tip region. The author's proposal is to introduce the coefficient of the strip position effect on each individual bar and a way of taking into account the work (energy) absorbed by the strengthening. The energy causes a reduction of the velocity of the crack propagation in the rebar, and consequently, an increase in its durability.

The theoretical model was verified in the experiments carried out on two series of reinforced concrete beams with different steel ratio. In each series, three beams were tested: non-strengthened, strengthened with one strip and strengthened with two strips. For each group of the beams the value of fatigue load was matched to get similar stresses in the tension bars.

On the basis of the analysis of the results of the experiments and calculations using the theoretical model proposed the following conclusions have been drawn:

- the strengthening of reinforced concrete beams by gluing non-stressed CFRP strips increases their fatigue life;
- an increase in fatigue life of the normal cross-section of the strengthened reinforced concrete beam results from an increase in the durability of the reinforcing bars;
- the beam strengthening ratio depends on the area of the external CFRP strips used and localization of those strips according to individual rebars;
- the results of computational analysis of fatigue life according to the theoretical model proposed show positive agreement with the test results.

### References

[1] Derkowski W., Zych T.: *Modern Composite Materials for Strengthening of Building Structures* (in Polish), Czasopismo Techniczne Z. 14-B, Kraków, 2004, pp. 15–25.

[2] Barnes R.A., Mays G.C.: *Fatigue Performance of Concrete Beams Strengthened with CFRP Plates*, Journal of Composites for Construction, 1999, No. 5, pp. 63–72.

[3] Heffernan P.J.: *Fatigue Behavior of Reinforced Concrete Beams Strengthened with CFRP Laminates*, Royal Military College of Canada, Kingston, Ontario, 1997.

[4] Derkowski W.: *Fatigue Life of Bent RC Cross-Sections Strengthened with Caron Fiber Strips*, Doctoral Thesis (in Polish), Cracow University of Technology, Cracow, 2005.
[5] *Externally Bonded FRP Reinforcement for RC Structures*, FIB Bulletin, No. 14, July 2001.
[6] Tepfers R., Kutti T.: *Fatigue Strength of Plain, Ordinary, and Lightweight Concrete*, Journal ACI, May 1979, 76(5).
[7] Paris P., Erdogen F. A.: *Critical analysis of crack propagation laws*, Journal of Basic Engineering, Transactions of ASME, December 1963, D 85(4).
[8] Salah El Din A.S., Lovegrove J.M.: *Formation and Growth of Fatigue Cracks in Reinforcing Steel for Concrete*, Fatigue of Engineering Materials and Structures, 1990, 3(4), pp. 315–323.
[9] Salah El Din A.S., Lovegrove J.M.: *Fatigue of Cold Worked Ribbed Reinforcing Bar, a Fracture Mechanics Approach*, International Journal of Fatigue, January 1982, 4(1), pp. 15–26.
[10] Kocańda S.: *Fatigue Fracture of Metals* (in Polish), Wydawnictwa Naukowo-Techniczne, Warszawa, 1985.
[11] Corley W.G. et al.: *Fatigue of Steel and Concrete Structure, Background of American Design Procedure for Fatigue of Concrete*, JABSE Coll., July 1991, Vol. 3, Lausanne.

## Wpływ wzmocnienia zginanych belek żelbetowych materiałami kompozytowymi na ich trwałość zmęczeniową

Stosowanie coraz dokładniejszych metod obliczeniowych, zbliżenie wartości wytrzymałości obliczeniowych do wartości naprężeń rzeczywiście występujących w najbardziej wytężonych przekrojach oraz zwiększający się udział zmiennych obciążeń (związanych z eksploatacją obiektu) w obciążeniach całkowitych sprawiają, że nośność zmęczeniowa oraz związana z nią trwałość nie mogą być pomijane w analizie pracy wielu konstrukcji – zagadnienie to szczególnie dotyczy obiektów mostowych.

Niniejsza praca dotyczy zagadnienia zmęczenia belek żelbetowych wzmocnionych za pomocą materiałów kompozytowych. Zaproponowano w niej teoretyczny model określania trwałości zmęczeniowej zginanego przekroju żelbetowej belki wzmocnionej zewnętrznymi, nienaprężonymi taśmami z włókien węglowych. Autorskim rozwiązaniem jest zarówno wprowadzenie współczynnika wpływu położenia taśmy na poszczególne pręty zbrojenia zwykłego, jak i sposób uwzględniania energii przejmowanej przez wzmocnienie. Energia ta wpływa na zmniejszenie prędkości rozwoju pęknięcia w pręcie obciążonym cyklicznie, a więc na zwiększenie jego trwałości.

Zaproponowany model teoretyczny został zweryfikowany doświadczalnie na dwóch seriach belek żelbetowych o różnych stopniach zbrojenia oraz wzmocnienia. Obciążenie cykliczne belek zaprogramowano, zakładając, że wytężenie rozciąganego zbrojenia zwykłego w danej grupie belek jest stałe.

Na podstawie analizy przedstawionego modelu teoretycznego oraz wyników przeprowadzonych badań doświadczalnych można stwierdzić, że:

- wzmacnianie zginanych konstrukcji żelbetowych przez doklejenie do krawędzi rozciąganej taśm z włókien węglowych zwiększa ich trwałość zmęczeniową;
- zwiększenie trwałości zmęczeniowej przekroju normalnego żelbetowej belki wzmocnionej jest wynikiem zwiększenia trwałości prętów zbrojeniowych;

- stopień wzmocnienia belki żelbetowej zależy od przekroju taśm zastosowanych do jej wzmocnienia oraz od lokalizacji tych taśm względem prętów zbrojeniowych belki;
- uzyskano dużą zgodność wyników obliczeń według zaproponowanego modelu z wynikami badań doświadczalnych.

ARCHIVES OF CIVIL AND MECHANICAL ENGINEERING

Vol. VI 2006 No. 4

# Analysis of support zones in composite concrete beams using MCFT

ANNA HALICKA
Lublin University of Technology, ul. Nadbystrzycka 40, 20-618 Lublin

The paper presents the method of analyzing static work of support zones in concrete composite structures. This method is based on MCFT (Modified Compression Field Theory). While designing composite beams, the author allows only such cases, where the appearance of the interface crack is precluded by the diagonal crack. The case of support zones with diagonal cracks and locally cracked interface has been examined in detail. The distribution of strains, important from the viewpoint of bearing capacity of the sheared zones, at the height of the model beam, which was the subject of author's research, has been developed. The method of evaluating the bearing capacity of composite elements with locally cracked interface based on MCFT is proposed.

Keywords: *concrete composite structures, shear, support zones*

## 1. Introduction

The interface between the component parts constitutes a specific feature of concrete composite structures. The interface fundamentally influences a static work of the whole structure, and especially the bearing capacity of the support zone of the composite beam.

In the paper [1], the author relying on the results her own tests [1, 2] and these reported in literature classified the damage mechanisms of composite concrete beams and stated that the design of such structures should be allowed only in the case where the appearance of the interface crack is precluded by the diagonal crack. Otherwise, when the damage to a beam begins with interface cracking, the gradually enlarging delamination leads to the separation of component parts, which begin to work ”independently” of each other. This means that composite element will never acquire the potential flexure of shear bearing capacity.

If, instead, the diagonal crack appears first, the three cases are possible after reaching the interface by this crack:

- the diagonal crack crosses the interface, and the beam behaves as a monolithic one, therefore this it is the optimal case, where full bearing capacity of flexure and shear can be efficiently used,
- the crack propagates locally within the interface (the interface is the place of the weakest strength parameters and determines the direction of diagonal crack), and then propagates into the upper layer of a composite beam,

- the crack propagates locally within the interface, and when the load is close to the ultimate value, it expands to the upper layer of a composite beam and at the same time it propagates within the interface towards the front of the beam; such a situation occurs only when the maximum stress in the interface exceeds the value of stress cracking the interface.

This paper discusses only the case of local cracking of the interface, and especially bearing capacity of composite beams with such a crack. For this purpose, the MCFT (Modified Compression Field Theory) [3, 5] was adapted, originally created for the analysis of cross sections subject to shear in concrete monolithic beams.

## 2. Assumptions of MCFT

### 2.1. Basic relations

Contemporary theories which describe the mechanisms of shear in reinforced concrete structures [3, 4, 5] assume that each section of sheared zone is subject to normal stresses $\sigma_x$ (in the direction of longitudinal reinforcement) and $\sigma_y$ (in the direction of transverse reinforcement) as well as to tangential stress $\tau_{xy}$. The stresses exist in concrete and the reinforcement, the principal stress $\sigma_{c1}$ and $\sigma_{c2}$ occur in concrete, while the reinforcement is subjected only to axial tension ($\sigma_{sx}$ and $\sigma_{sy}$). The angle $\alpha$ between the $x$-axis and the axis of principal stress 2 is regarded as fixed, i.e., independent of the load level and corresponding to the arrangement of principal axes in an uncracked element (*fixed angle softening truss model*), or as changing during a load increase and creation of new cracks, which is confirmed by the results of experiments (*variable angle model*).

In MCFT method, the model of variable angle was adopted [3, 5]. Furthermore, it was assumed that after cracking the direction of concrete trusses separated by diagonal cracks, described by the angle $\theta$ of inclination of diagonal cracks to longitudinal axis, is the same as the angle determining the axes of the principal stress $\alpha$. The angular difference between the position of principal axes in uncracked and cracked elements depends on the proportion of stresses in longitudinal and transverse reinforcements. When these stresses are equal, the principal axes in these two cases overlap. Relations describing the stress–strain state are the following:

- Equations of equilibrium

$$\begin{aligned}
\sigma_x &= \sigma_{c2} \cdot \cos^2\alpha + \sigma_{c1} \cdot \sin^2\alpha + \rho_x \sigma_{sx}, \\
\sigma_y &= \sigma_{c2} \cdot \sin^2\alpha + \sigma_{c1} \cdot \cos^2\alpha + \rho_y \sigma_{sy}, \\
\tau_{xy} &= (-\sigma_{c2} + \sigma_{c1}) \cdot \sin\alpha \cos\alpha.
\end{aligned} \tag{1}$$

- Equations of strains equality

$$\begin{aligned}
&\varepsilon_x = \varepsilon_{c2} \cdot \cos^2 \alpha + \varepsilon_{c1} \cdot \sin^2 \alpha, \\
&\varepsilon_y = \varepsilon_{c2} \cdot \sin^2 \alpha + \varepsilon_{c1} \cdot \cos^2 \alpha, \\
&\frac{\gamma_{xy}}{2} = (-\varepsilon_{c2} + \varepsilon_{c1}) \sin \alpha \cos \alpha,
\end{aligned} \tag{2}$$

where $\rho_x$ and $\rho_y$ are the reinforcement ratios in *x* and *y* directions.

Authors of MCFT [3, 5] propose to calculate all parameters of stress-strain state of the cross section, i.e. stresses in concrete $\sigma_{cx}$, $\sigma_{cy}$, $\sigma_{c1}$, $\sigma_{c2}$, $\tau_{xy}$, stresses in reinforcement $\sigma_{sx}$, $\sigma_{sy}$, strains $\varepsilon_x$, $\varepsilon_y$, $\gamma_{xy}$ as well as the angle $\theta$ (determining the direction of diagonal cracks and direction of principal stresses) after previous division of the cross-section into horizontal layers (*m* concrete layers and reinforcing bars arranged in *n* layers). These layers are analysed one after another iteratively after initial assumption of the distributions along the height of the cross-section of shear stress $\tau_{xy}$ and longitudinal strain $\varepsilon_x$, and assigning the values $\tau_{xy,i}$ and $\varepsilon_{x,i}$ to each layer. While solving this issue, one arrives at the following relations: three equations of Mohr's Circle for stresses (1), three equations of Mohr's Circle for strains (2) and four equations relating strains to stresses (section 2.2). In order to verify ultimately that the assumptions and the parameters calculated are valid, the equations of equilibrium are checked for the whole cross-section:

$$\begin{aligned}
&\sum_{i=1}^{m} \sigma_{cx,i} \cdot b_i h_i + \sum_{j=1}^{n} \sigma_{sx,j} \cdot A_{sj} = N, \\
&\sum_{i=1}^{m} \sigma_{cx,i} \cdot b_i h_i \cdot (y_{ci} - \overline{y}) + \sum_{j=1}^{n} \sigma_{sx,i} \cdot A_{sxj} \cdot (y_{sj} - \overline{y}) = M, \\
&\sum_{i=1}^{m} \tau_{xy,i} \cdot b_i h_i = V,
\end{aligned} \tag{3}$$

where:

$y_{ci}$ – the distance of *i*-layer from the upper edge of the cross-section,

$y_{sj}$ – the distance from reinforcing bars in *j*-layer to the upper edge of the cross-section,

$\overline{y}$ – the distance from the center of gravity of the cross-section to the upper edge of the cross-section.

Two cross-sections are considered in the cracked element: the plane along the crack and the plane of the area between cracks (Figure 1). It is assumed that the values of tensile stress change along the distance between the cracks from 0 on the edge of the crack to the maximum value in the middle of this distance, and therefore average value of this stress is considered. Whereas along the edge of the crack the tangential stress is generated, which is the result of aggregate interlocking.

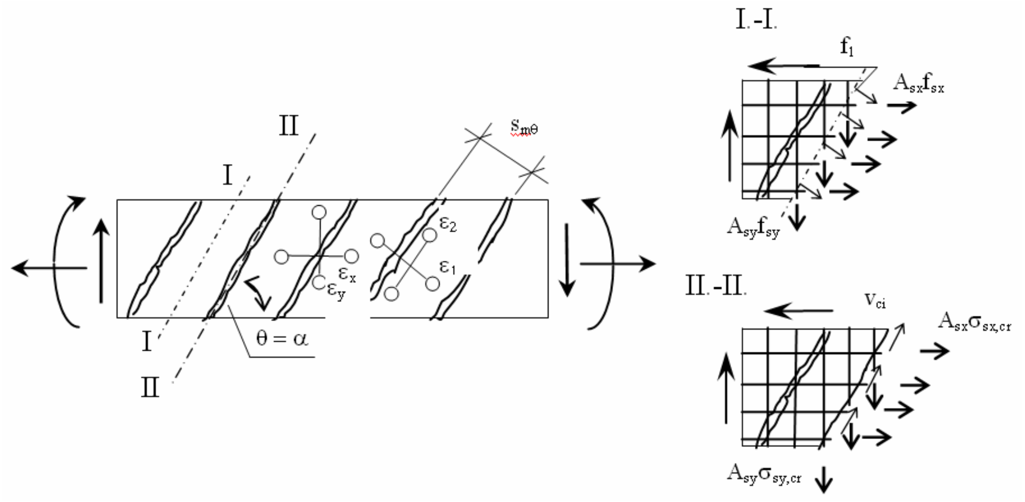

Fig 1. The diagram of forces and stresses in the element with diagonal cracks adopted in MCFT (Modified Compression Field Theory) according to [3]

## 2.2. Constitutive relations for the steel and concrete

The essential assumption of the shear theory in the reinforced concrete beams is that areas lying between the diagonal cracks work in the combined stress state: compression (in direction ‘2’) and tension (in direction ‘1’). In order to solve the issue, it is necessary, apart from recording relations (1), (2), to assume the stress–strain characteristics of compressed concrete (relating $\sigma_2$ to $\varepsilon_2$), tensioned concrete (relating $\sigma_1$ to $\varepsilon_1$), sheared concrete (relating $\tau_{21}$ to $\gamma_{21}$) and steel. Since compressed trusses of concrete are also tensioned perpendicularly, the relations $\sigma$–$\varepsilon$ for compressed concrete include the so-called ‘tension stiffening effect’. MCFT method assumes the following relations:

- in steel

$$\sigma_{sx} = \varepsilon_x \cdot E_s, \tag{4}$$

$$\sigma_{sy} = \varepsilon_y \cdot E_s; \tag{5}$$

- in tensioned concrete

$$\sigma_{c1} = \varepsilon_1 \cdot E_c, \text{ (before cracking)}, \tag{6}$$

$$\sigma_{c1} = \frac{\sigma_{cr}}{1+\sqrt{200\varepsilon_1}}, \text{ (after cracking)}; \tag{7}$$

- in ‘softened’ compressed concrete:

$$\sigma_{c2} = \sigma_{c2,\max}\left[2\left(\frac{\varepsilon_{c2}}{\varepsilon'_c}\right) - \left(\frac{\varepsilon_{c2}}{\varepsilon'_c}\right)^2\right], \tag{8}$$

where:

$\sigma_{c2,\max}$ – maximum value of compressive stress in concrete working in the combined stress state calculated on the basis of the relation:

$$\frac{\sigma_{c2,\max}}{f'_c} = \frac{1}{0.8 + 170\varepsilon_1},$$

in which

$f_c'$ – a compressive strength of concrete in uniaxial stress state,

$\varepsilon_c'$ – the strain at peak stress $f_c'$,

$E_c$ – the modulus of elasticity of concrete, $E_c \cong \frac{\sim 2 f'_c}{\varepsilon'_c}$,

$\sigma_{cr}$ – tensile stress upon concrete cracking, whose value according to code [6] is assumed as $f_{cr} = 0.33\sqrt{f'_c}$,

$E_s$ – the modulus of elasticity of steel.

### 2.3. Complementary assumptions

Complementary assumptions of the theory are the relations of tangential stress $v_{ci}$ that can be transmitted across the crack to its width *w* and aggregate size *a* (*w* and *a* are in mm, and $f_c'$ is in MPa):

$$v_{ci} = \frac{0.18 \cdot \sqrt{f'_c}}{0.3 + \frac{24 \cdot w}{a_{\max} + 16}}, \tag{9}$$

and the assumption of the equivalence of stresses in the I–I and II–II planes (Figure 1), leading to the inequality which limits the value of the stress $\sigma_{c1}$:

$$\sigma_{c1} \le v_{ci} \cdot \tan\theta + \frac{A_{sy}}{b \cdot s}(\sigma_{sy,cr} - \sigma_{sy}), \tag{10}$$

where:

$A_{sy}$ – the cross-section area of one stirrup in the $y$-direction,
$b$ – the width of layer,
$s$ – the spacing of stirrups,
$\sigma_{sy,cr}$ – the stress in the stirrups in the crack,
$\sigma_{sy}$ – the stress in stirrups outside the crack.

If the yield point is achieved in the stirrups, the process of flow begins and the stress $\sigma_{c1}$ is limited to:

$$\sigma_{c1} \le v_{ci} \cdot \tan\theta\,. \tag{11}$$

### 2.4. Criteria of damage

The damage of cross-section may be caused by bending moment, when the stress $\sigma_{x,i}$ achieves the compressive strength, or by shear. In the second case, the criterion of damage is yielding of stirrups. When the condition $\sigma_{c1,i} \le v_{ci} \cdot \tan\theta$ is not fulfilled in the layer of concrete, the unbalanced stress $\sigma_{1,i}$ is taken over by stirrups, which consequently yield. This means that a layer is not able to carry the increasing load and the redistribution of stress occurs. Consequently, the load of adjoining layer increases leading to yielding of stirrups in the next layer.

The bearing capacity of cross-section can be calculated as follows:

$$V_R = \sum_{i=1}^{n} \left( \frac{\sigma_{c1,i} \cdot b_i \cdot h_i}{\tan\theta_i} + \frac{A_{sy} \cdot f_y \cdot h_i}{s} \cdot \frac{1}{\tan\theta_i} \right), \tag{12}$$

regarding that

$$\sigma_{c1,i} \le v_{ci} \cdot \tan\theta_i = \frac{0.18 \cdot \sqrt{f_c{}'}}{0.3 + \dfrac{24 \cdot w_i}{a_{\max} + 16}} \cdot \tan\theta_i. \tag{13}$$

Denotations in formulas (12) and (13) are the same as in expressions (3)–(11).

## 3. The analysis of support cross-sections in composite elements using MCFT method

### 3.1. Algorithm of calculation

During the analysis of the support cross-sections of concrete composite structures the MCFT method which employs ‘layering’ of the element was used, as it considers the differences in material parameters at the level of the cross-section. Different ways

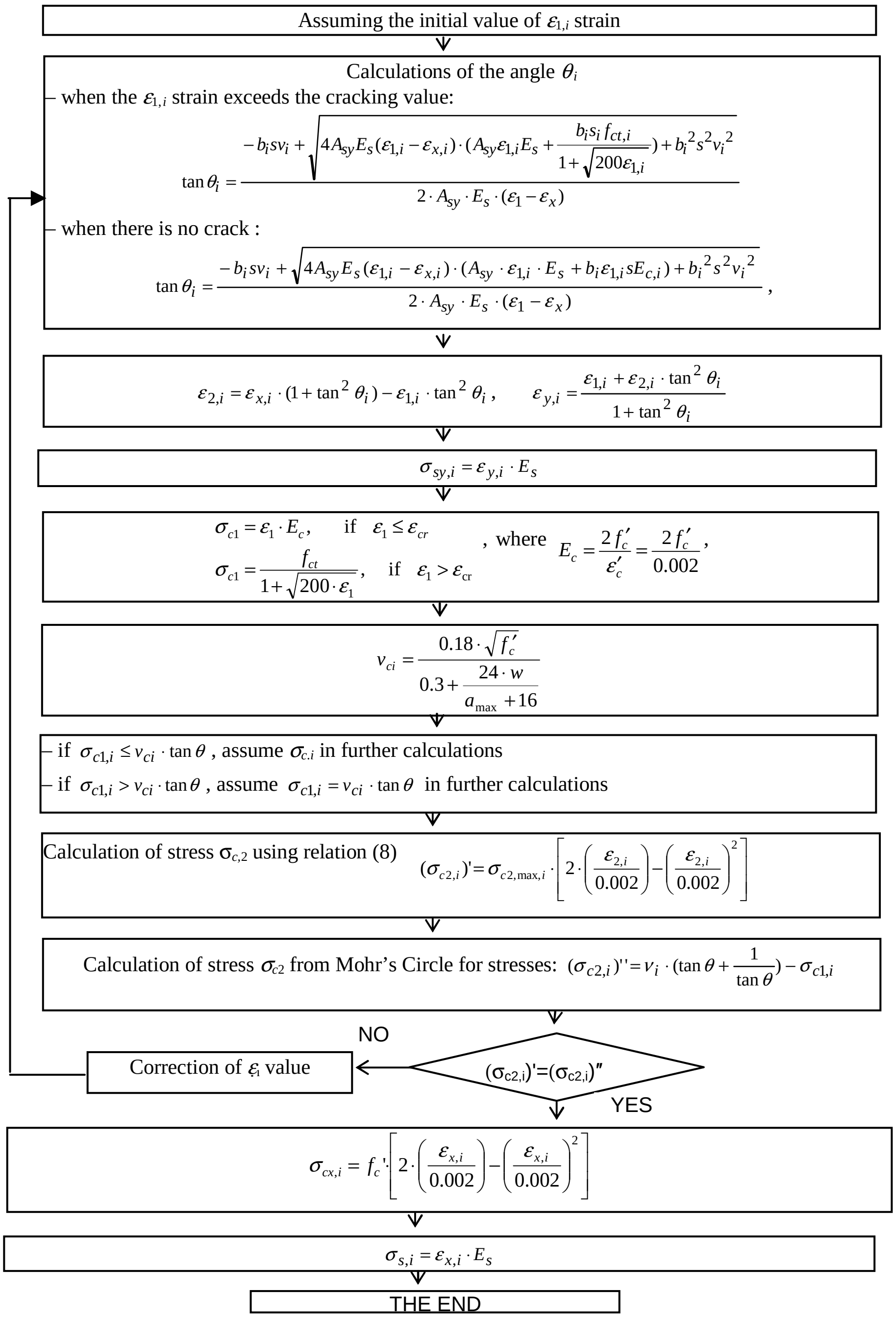

Fig. 2. The block diagram of the calculation of stress–strain state in the *i*-layer, drawn up on the basis of [8]

of the stress–strain state calculations in the individual layers based on this theory, including among others [3, 5, 7, 8], were analysed. The Nakamura and Hagai's [8] algorithm was chosen as optimal. Block diagram of this algorithm is presented in Figure 2. Before starting the calculations according to this algorithm, the values of $\varepsilon_{x,i}$ and $\tau_{xy,i}$ should be assigned to the analysed layer.

### 3.2. The stress–strain state in the support zones of a model composite beam

The calculations exemplifying the stress–strain state were carried out for a model composite beam which was the subject of author's own experimental research. The goal of this research was to examine the static work of composite beams with different joints between the two connected concretes. Three series of tests were carried out for a lot of three beams: BZ/P series – beams with adhesion in the interface, BZ/P+S series – beams with joining stirrups and adhesion in the interface, BZ/S series – beams with stirrups and broken adhesion in the interface (Figure 3). Beams were loaded with two forces pointwise applied. During the process of loading, the following parameters were measured: deflection, stress in the stirrups, longitudinal strains of concrete elements and the displacement of connected elements in relation to each other at the end of the beam.

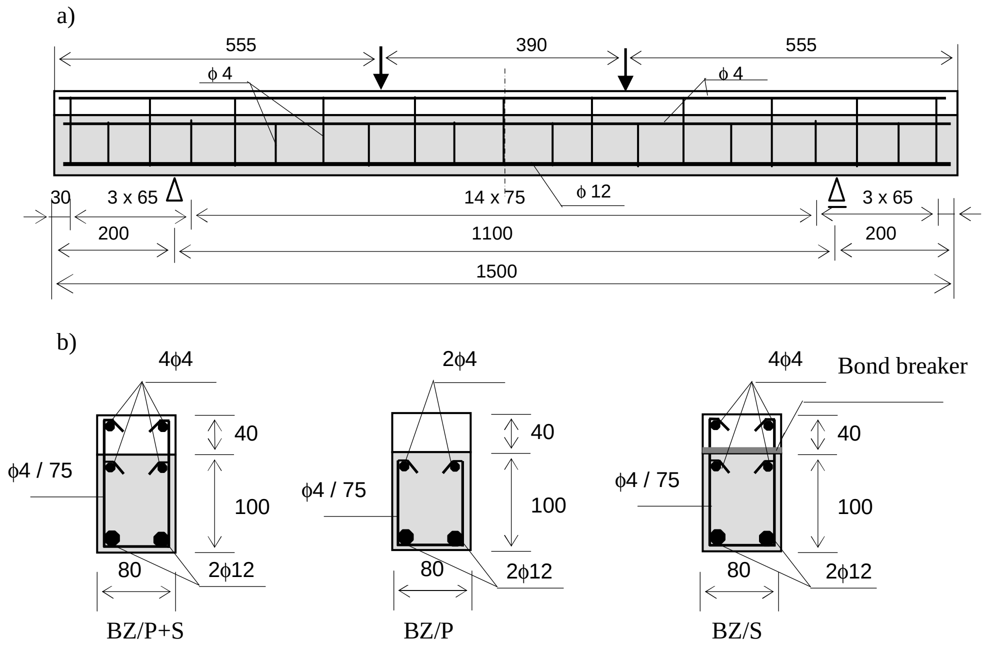

Fig. 3. Model composite beams used in author's own research:
a) longitudinal section, b) cross-sections of beams of particular series

All beams were damaged in support zones; however, the crack patterns of each series were different. Detailed results of the research are published elsewhere (including [1, 2]), whereas this paper quotes only the data important for static work of support zones of beams with contact area cracked locally of BZ/P+S series beams (Figure 4). The diagonal crack appeared in beams from this series, when the average value of loading force $P$ amounted to 16.66 kN, the crack reached the interface at the average value of forces $P$ = 17.5 kN, and the damage occurred, when the average value of forces $P$ was 25.66 kN.

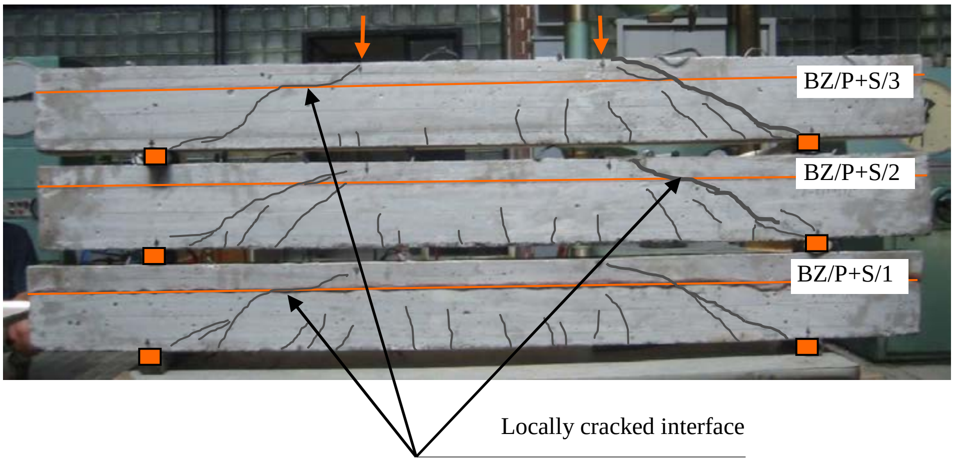

Fig. 4. Crack pattern of beams of the BZ/P+S series with locally cracked interface

The analysis of the beams examined was carried out for the cross-section located within the shear zone at the distance of 12.5 cm from the support. Calculations were made for the loading force $P$ = 17.5 kN (i.e., the value of cracking force) in accordance with the assumptions stipulated in section 2. Successive stages of calculations included:

1. Dividing the cross-section into 7 layers of the height $h_i$ = 2 cm and the width $b_i$ = 8 cm.

2. Assigning the material parameters to each layer according to the results of auxiliary tests – uniaxial compressive strength (bottom layer $f'_{c,p}$ = 22.8 MPa, upper layer $f'_{c,n}$ = 41.3 MPa) and tensile strength (bottom layer $f_{ct,p}$ = 1.92 MPa, upper layer $f_{ct,n}$ = 2.88 MPa).

3. Establishing shear stress distribution along the height of the cross section, using ‘two cross-section method’ recommended by Vecchio and Collins [5] (this distribution is presented in Figure 5, where, for the purpose of comparison, the distribution in monolithic beam is presented).

4. Assuming the line distribution of longitudinal strain $\varepsilon_x$ at the height of the beam and assigning the value of the strain $\varepsilon_{x,i}$ to each layer.

5. Assessing the stress–strain state of each layer according to the algorithm presented in Figure 3.

6. Examining the equilibrium conditions (3) – if they are not fulfilled, correction of the assumed distribution of longitudinal strain $\varepsilon_{x,i}$ and repetition of the calculations of stress–strain state.

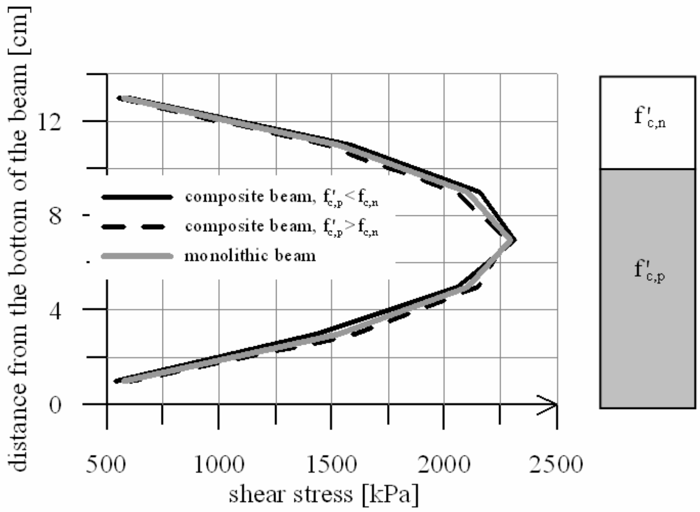

Fig. 5. Shear stress distribution at the height of the model beam under the loading force of 17.5 kN, at the distance of 12.5 cm from the support, obtained using ‘two cross-sections method’

As a result of calculations, the distributions of the strains $\varepsilon_1$, $\varepsilon_2$, $\varepsilon_x$ and $\varepsilon_y$ at the height of the beam in the analysed cross-section were obtained. For the purpose of comparison, the same calculations were carried out for the beam of the same size, but with the reverse order of layers: the thickness of bottom layer amounted to 4 cm and the thickness of the upper layer – 10 cm, and for monolithic beams alternatively made of concrete with the strength $f_c' = 22.8$ MPa and $f_c' = 41.3$ MPa. On the basis of these calculations, one can infer that the distribution of the strains $\varepsilon_x$ in a composite beam is identical as that in a monolithic beam made of concrete of the same strength as the upper layer. Figure 6 presents the distributions of strains which determine the shear bearing capacity $\varepsilon_1$ and $\varepsilon_y$.

Analysing the above-mentioned distributions in the beams with interface placed in the upper half of the cross-section one may conclude that they resemble the distributions of monolithic beam made of the same concrete as the bottom layer. On the other hand, in the case of beams with interface placed in the bottom half of the cross-section, one may observe the following: the strains $\varepsilon_1$ and $\varepsilon_y$ in the bottom layer are identical to these in a monolithic beam produced of the same concrete as the bottom layer, in upper fibres of the upper layer they are identical to these in a monolithic beam made of the same concrete as the upper layer and in the interface zone they assume intermediate values. This means that, for instance, in a zone, where the strains analysed are the largest (the zone where the destruction caused by shear begins) – they are larger than the strains in the case of monolithic beam made of the stronger of the connected concretes.

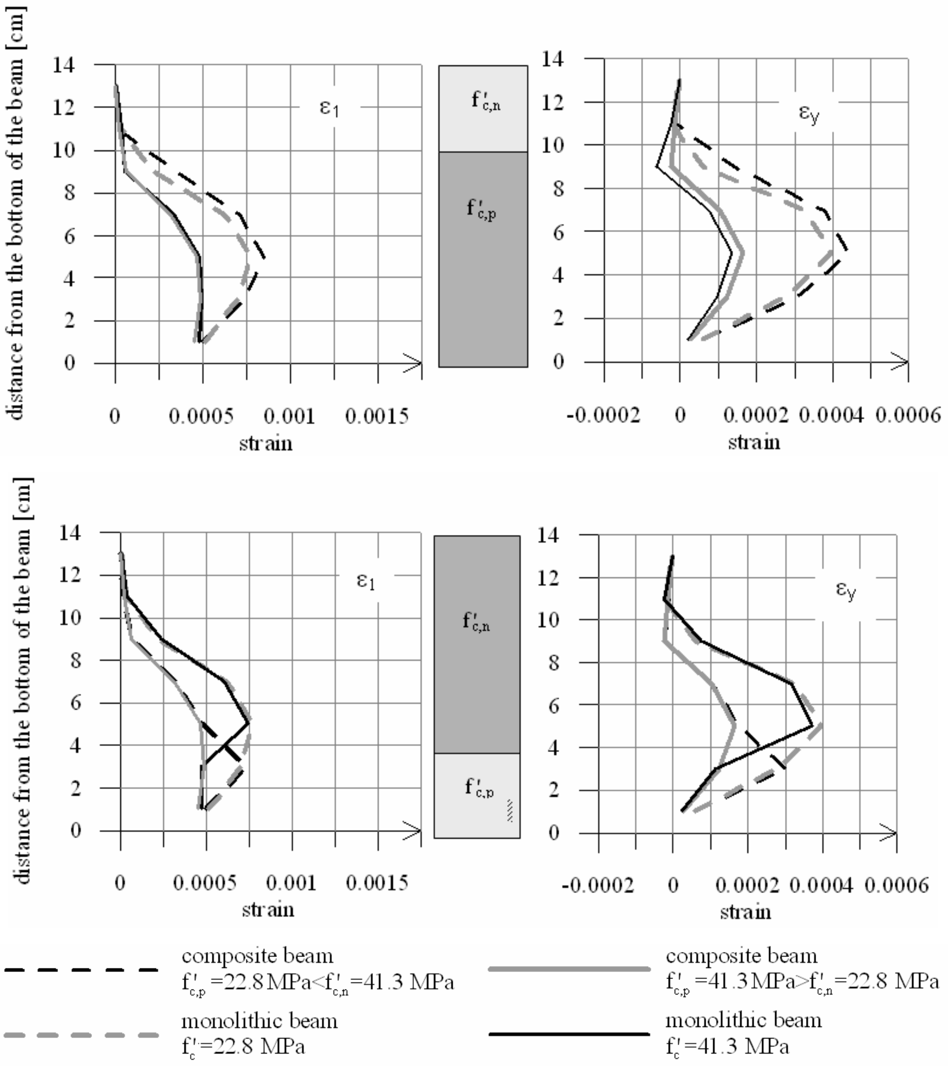

Fig. 6. Distributions of the strains $\varepsilon_1$ and $\varepsilon_y$ at the height of model beams of the same size as examined beams at the distance of 12.5 cm from the support under the force $P$ = 17.5 kN, obtained through calculations using MCFT

## 4. The influence of local delamination of the interface on the static work of support zones

### 4.1. The length of the local crack in the interface

In the uncracked interface between the bottom and the upper layers of concrete, we deal with adhesion, which counteracts the shear and tension of the interface. In the described case of the cracked interface, there occurs a disturbance in the uniform transmission of forces between the two connected layers. Outside the crack, the interaction of the connected parts is undisturbed again, which means that the crack propagates into the upper layer at an angle being correlated with the existing stress–strain state.

In order to estimate the length of the local crack in the interface, the analytical model shown in Figure 7 was applied. It presents the situation, where diagonal crack in the bottom layer has reached the interface level. In the section crossing the crack in its vertex, there exist longitudinal internal forces, caused by the bending moment: compression in the concrete (its resultant equals $D_{c,n}$ in the upper layer and $D_{c,p}$ in the bottom layer) and tension both in concrete (resultant value $Z_c$) and in steel (force $Z_s$).

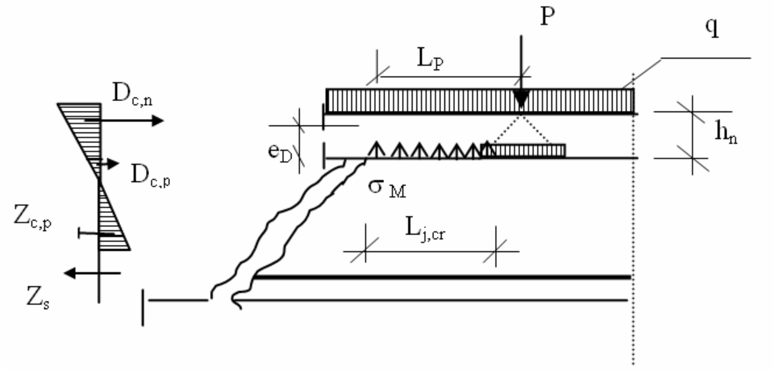

Fig. 7. The model adopted for calculation of the length of the local crack in the interface

The force $D_{c,n}$ acts eccentrically in relation to the interface (eccentricity equals $e_D$), and along the zone of the interface adjoining the vertex of the crack there occurs tensile stress generated by the moment:

$$M_D = D_{c,n} \cdot e_D. \tag{14}$$

The moment $M_D$ achieves its full value calculated with formula (14) only when the stiffness of the upper layer is very small compared to the stiffness of the bottom layer. If the bottom part is deformable, then the value of the moment $M_D$ is smaller and is the function of the ratio of stiffness of the upper layer $E_n J_n$ to stiffness of the bottom layer $E_p J_p$:

$$M_D = \alpha \cdot D_{c,n} \cdot e_D, \tag{15}$$

where α is the coefficient dependent on the ratio of stiffness $\dfrac{E_n J_n}{E_p J_p}$.

At the same time the interface is compressed by a continuous load $q$ and the stress resulting from the force $P$ applied at the distance $L_p$ from the vertex of the diagonal crack (the angle of stress propagation was assumed to be 45°):

$$M_d = 0.5 \cdot q \cdot b \cdot L_{j,cr}^2 + \frac{P}{b_j \cdot (h_n \cdot \tan 45°)} \cdot b_j \cdot \frac{[h_n - (L_p - L_{j,cr})]^2}{2}. \tag{16}$$

These stresses caused by the moment ($M_D - M_d$) are counteracted by adhesion. Cracking in the interface occurs along the interval $L_{j,cr}$, where tensile stress $\sigma_M$ exceeds tensile strength of the interface $\sigma_{ct,j}$. The moment counteracting the separation of layers, on a simplified assumption that the distribution of adhesion stress is uniform, equals:

$$M_{L_{j,cr}} = \sigma_{ct,j} \cdot \frac{b_j \cdot L_{j,cr}^2}{2}. \tag{17}$$

The length of local crack of the interface can be calculated by equation of moments:

$$M_D - M_d = M_{L_{j,cr}}, \tag{18}$$

which results in the expression:

$$L_{j,cr} = \frac{\dfrac{P}{h_n}(L_p - h_n) - \sqrt{\dfrac{P^2}{h_n^{\,2}}\left(L_p - h_n\right)^2 - \left[\left(q + \sigma_{ct,j}\right)b_j + \dfrac{P}{h_n}\right]\left[\dfrac{P}{h_n}\left(L_p - h_n\right)^2 - 2\alpha D_{c,n} e_D\right]}}{(q + \sigma_{ct,j}) \cdot b_j + \dfrac{P}{h_n}}. \tag{19}$$

If the value obtained fulfills the condition: $L_{j,cr} \le L_p - h_n$, the force $P$ does not influence the length of the crack. Therefore the value $L_{j,cr}$ should be calculated again, but without considering the force $P$, and expression (19) takes the following form:

$$L_{j,cr} = \sqrt{\frac{2 \cdot \alpha \cdot D_{c,n} \cdot e_D}{(q + \sigma_{ct,j}) \cdot b_j}}. \tag{20}$$

In order to verify the expression obtained, the calculations were carried out using the model beams tested, described in the section 3.2. In the calculations, we adopted the load of $q = 0$ and $P = 25$ kN which was applied in the stage preceding the damage to beams from BZ/P+S series. In the calculations based on MCFT method, in the cross-section located in the centre of the shear zone, the resultant force $D_n = 39.11$ kN was obtained. The tensile strength of the interface was assumed to be equal to tensile strength of weaker of the connected concretes $\sigma_{ct,j} = 1920$ kPa. The length of the local crack in the interface calculated according to formula (20), assuming $\alpha = 1$, equals to 11.5 cm. In the test, this length ranged from 7.5 to 11.6 cm.

### 4.2. Bearing capacity of support zones of composite structure with locally cracked interface

As described above, the stress $\sigma_{c1}$ determines the possibility of carrying the shear force. In the MCFT method, the value of this stress must be smaller than the limit value $\sigma_{c1,i} \le v_{ci} \cdot \tan\theta$. Exceeding this value causes the takeover of the unbalanced stress by stirrups and, as a result, their yielding. Limit value corresponds to the possible value of tangential stress, which can be carried by the diagonal crack due to aggregate interlocking. This value is described by expression (9) and depends on the width of the crack (the wider the crack, the smaller the limit value). Therefore, in order to estimate the bearing capacity of support zones, one needs to know the width of the crack.

Bhide and Collins [9], while analysing the sheared cross-section using MCFT, recommend calculating the width of diagonal crack as the product of the strain $\varepsilon_1$ and the spacing of diagonal cracks $s_{m\theta}$.

$$w = \varepsilon_1 \cdot s_{m\theta} \tag{21}$$

and the spacing, measured perpendicularly in relation to cracks, is established based on the spacing in the *x*- and *y*-directions $s_{mx}$, $s_{my}$ in line with relation (the same as in the code [10]):

$$s_{m\theta} = \frac{1}{\dfrac{\sin\theta}{s_{mx}} + \dfrac{\cos\theta}{s_{my}}}. \tag{22}$$

When calculating the spacing of the cracks in the *x*- and *y*-directions, it is reasonable to use the relationships stipulated in the code [10]:

$$s_{s(x,y)} = 50 + 0.25 \cdot k_1 \cdot k_2 \cdot \frac{\phi_{(x,y)}}{\rho_{r,(x,y)}}, \tag{23}$$

where:

$k_1$ – the coefficient dependent on the kind of reinforcement (smooth or ribbed),

$k_2$ – the coefficient dependent on the longitudinal strain distribution in the tensile zone (bending, tension),

$\phi_{(x,y)}$ – the diameter of reinforcing bars in the $x$- and $y$-directions,

$\rho_{r,(x,y)}$ – the reinforcement ratio in the $x$- and $y$-directions in the relation to effective tensile area.

The calculations of test beams under the load of $P$ = 25 kN (the stage of load preceding the damage to beams of BZ/P+S series) were carried out according to the above-mentioned rules. The values of strains obtained by means of MCFT method were used, and they include: $s_{m,x}$ = 71 mm, $s_{m,y}$ = 85 mm, spacing between diagonal cracks in individual layers equal to $s_{m,\theta}$ = 55–77 mm, widths of cracks $w$ = 0.06–0.10 mm. Whereas, in the tests at this stage of load, the width of diagonal cracks achieved considerably higher values (0.40–0.80 mm). At the same time, the cracks in the interface also achieved high values (0.4–0.55 mm). Therefore it may be concluded that the width of interface crack influences the width of a diagonal crack (Figure 8). This influence can be described by the relation:

$$w' = w + \frac{w_s}{\cos\theta}. \tag{24}$$

In the calculations carried-out, the maximum width value of diagonal crack, i.e., 0.10 mm, was obtained in the third layer from the bottom of the beam, at the angle of $\theta$ = 35°, thus $w' = 0.10 + \frac{0.4 - 0.55}{\cos 35°} = 0.59 - 0.77\text{mm}$. It is very close to the widths measured.

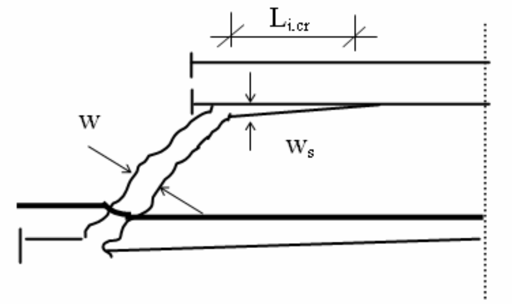

Fig. 8. The influence of the width of interface crack on the width of diagonal crack

Based on a calculation model presented in Figure 7, the width of interface crack can be treated as a result of the deflection of model cantilever, which amounts to:

$$w_s = \frac{(M_D - M_d) \cdot L_{cr}^2}{2 \cdot EJ}. \tag{25}$$

The width of the interface crack $w_s$ calculated for parameters as in section 4.1 and $\alpha$ = 1 is equal to 0.48 mm and corresponds to the values obtained in tests, i.e., $w_s$ = 0.4–0.55 mm.

Finally, it can be inferred that local interface crack influences the bearing capacity of support cross-sections of composite element by increasing the width of diagonal crack and diminishing the limit stress $\sigma_{c_1}$, which leads to the yielding of stirrups. Therefore, the MCFT method may by used in the case of beams with locally cracked interface; however, the calculations of the limit value of the stress $\sigma_{c1} \le v_{ci} \cdot \cot\theta$ should be carried out with consideration of the correction of diagonal crack width $w'$:

$$v_{ci} = \frac{0.18 \cdot \sqrt{f_c'}}{0.3 + \frac{24 \cdot w'}{a_{\max} + 16}}. \tag{26}$$

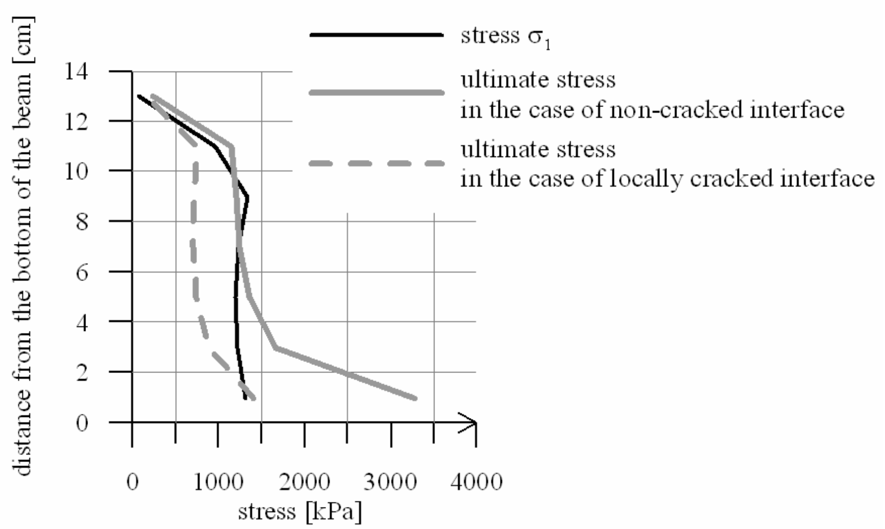

Fig. 9. Stress determining the carrying capacity of support cross-sections

Figure 9 presents the distribution of the stress $\sigma_1$ obtained while using the MCFT method under the load $P$ = 25 kN, the distributions of the limit values $v_{ci} \cdot \cot\theta$ calculated for uncracked interface ($w$ = 0.06–0.10 mm) and locally cracked interface ($w'$ = 0.61–0.71 mm). In the case of uncracked interface, the stress $\sigma_1$ is smaller than the limit value. If the interface cracks locally, an increased width of diagonal crack causes the diminishing of limit value of stress $\sigma_1$ and consequently the stress $\sigma_1$ is higher than the limit value. As mentioned above, this causes a gradual involvement of stirrups, which at the increasing width of the crack leads to their yielding.

Next, the same cross-section was considered, but under the load $P = 27.5$ kN, equal to the bearing capacity damaging the beams tested. It has been calculated that in this case, the width of diagonal crack equals 0.75 mm, which causes yielding of stirrups and leads to damage to the beam. This bearing capacity predicted in calculations is confirmed by the tests – the beams from BZ/P+S series with locally cracked interface were damaged under the load $P = 25$ kN or 27.5 kN.

## 5. Conclusions

On the basis of the calculations done and referring to the results of the tests carried out on model beams, the following conclusions can be drawn:

1. Producing concrete beam as a composite one influences the bearing capacity of its sheared cross-sections in comparison to monolithic beam. This manifests itself in the changes in the distributions of shear stress and the strains $\varepsilon_1$ and $\varepsilon_y$ along the height of the beam. The changes are especially disadvantageous in the case of beams with an interface placed in the bottom half of the cross-section: in a zone where the destruction caused by shear begins – the strains $\varepsilon_1$ and $\varepsilon_y$ are larger than the strains in the case of monolithic beam made of the stronger of the connected concretes.
2. The MCFT method is an effective tool for the analysis of composite cross-sections. However, the calculations should be carried out for the distribution of the stress and strains considering the differences of material parameters of connected elements.
3. Local cracking of interface affects the width of diagonal cracks. The length of such cracking can be calculated using formulae (19), (20).
4. The diagonal crack width should be calculated regarding its extension, in accordance with formulae (24), (25).

### References

[1] Halicka A.: *Damage mechnism of concrete composite beams* (in Polish), Inżynieria i Budownictwo, 2005, No. 8, pp. 438–441.

[2] Halicka A.: *Influence of factors affecting the bearing capacity of the interface on static work of concrete composite beams* (in Polish), Proceedings of VII Conference *Composite structures*, Zielona Góra, 2005, pp. 155–162.

[3] Collins M.P., Mitchell D., Adebar P., Vecchio F.J.: *A general shear design method*, ACI Structural Journal, January–February 1996, pp. 36–45.

[4] Pang X.B., Hsu T.T.C.: *Fixed angle softened truss model for reinforced concrete*, ACI Structural Journal, March–April 1996, pp. 197–207.

[5] Vecchio F.J., Collins M.P.: *Predicting the response of reinforced concrete beams subjected to shear using modified compression field theory*, ACI Structural Journal, May–June 1988, pp. 258–268.
[6] ACI 318-02, ACI-318R-02: *Building Code Requirements for Structural Concrete and Commentary*.
[7] Grabias M.: *Influence of expansive concrete on bearing capacity of support zones in concrete composite structures*, Ph. Thesis, Lublin University of Technology, 2001.
[8] Nakamura H., Higai T.: *Evaluation of shear strength of RC beam section based on extended modified compression field theory*, Concrete Library of Japan Society of Civil Engineers, No. 25, June 1995, pp. 93–105.
[9] Bhide S.B., Collins M.P.: *Influence of axial tension on the shear capacity of reinforced concrete members*, ACI Structural Journal, September–October 1989, pp. 570–581.
[10] Eurocode 2: *Design of concrete structures* – part 1–1: *General rules of buildings prEN 1992-1-2001* (final draft).

## Obliczanie stref przypodporowych żelbetowych elementów zespolonych z zastosowaniem metody MCFT

Zaprezentowano metodę analizy pracy statycznej stref przypodporowych w żelbetowych elementach zespolonych opartą na MCFT (*Modified Compression Field Theory*). Dopuszczając w projektowaniu belek zespolonych jedynie takie sytuacje, w których przy wzrastającym obciążeniu najpierw pojawi się rysa ukośna, a dopiero później – rysa w styku, rozważono szczegółowo stan strefy przypodporowej z lokalnie zarysowanym stykiem. Sporządzono rozkłady odkształceń, istotnych dla nośności stref przypodporowych, na wysokości belki modelowej będącej przedmiotem badań własnych. Zaproponowano sposób obliczania nośności na ścinanie metodą MCFT elementów z lokalnie zarysowanym stykiem.

ARCHIVES OF CIVIL AND MECHANICAL ENGINEERING

Vol. VI 2006 No. 4

# Comparative method of thermovision temperature measurement in single-pass internal cylindrical grinding

K. NADOLNY, J. PLICHTA

Koszalin University of Technology, ul. Racławicka 15–17, 75-620 Koszalin

This paper presents the results of thermovision temperature measurement in the contact zone of grinding wheel and workpiece during single-pass internal cylindrical grinding process. Such a kinematic form of grinding process is characterized by very difficult machining conditions. In order to control grinding temperature in this process, the authors developed a special measurement method which enables the usage of thermovision camera. The essence of a new method and the results of investigations were presented. In tests, the influence of abrasive grain kinds (alundum 99A, sintered corundum SG) and their size (46, 60) on grinding temperature was determined.

Keywords: *termovision measurement, single-pass internal grinding, grinding wheels*

## 1. Introduction

Temperature is one of the most important factors which affect the conditions of material removing in grinding process. It is particularly meaningful in single-pass internal cylindrical grinding, where we deal with large machining allowance and long contact zone of grinding wheel with workpiece. Thermal conditions determine the intensity of such elementary wear effects as: abrasive wear, strength wear and thermo-fatigue. In order to record temperature in this kind of grinding process, new method was developed and thermovision camera was used as measuring instrument.

## 2. Single-pass internal cylindrical grinding

In single-pass axial internal cylindrical grinding, all machining allowance is removed in only one pass of grinding wheel and simultaneously a proper quality of workpiece surface layer is guaranteed (Figure 1) [1–6].

The grinding wheel used in this process had conic chamfer which allows functional division of active surface of abrasive tool into rough and finish grinding zones. The width $T_1$ and a conic chamfer angle $\chi$ are matched to distribute uniformly a total machining allowance in large range of grinding wheel active surface. Simultaneously adequately wide cylindrical zone $T_2$ should be maintained to assure a desired quality of workpiece surface layer.

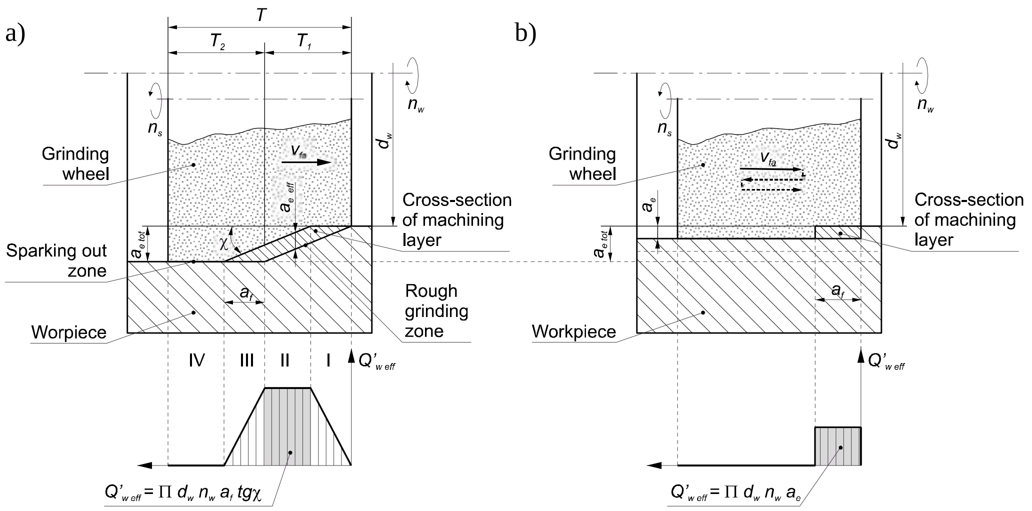

Fig. 1. Comparison of grinding wheel load in single-pass internal cylindrical grinding using grinding wheel with conic chamfer (a) and conventional multi-pass grinding (b) [4–6]

## 3. Experimental investigation

The purpose of our investigation was to define the influence of abrasive grains' kind and size on temperature in machining zone of single-pass internal cylindrical grinding [6].

### 3.1. Investigation conditions

The measurements in machining zone during single-pass internal cylindrical grinding were carried out with thermovision camera, type Raytek ThermoView Ti30 (Figure 2).

Device used for measurements belongs to long-wave spectral-range cameras (7–14 μm). Measuring range of this camera varies from 0 to 250 °C and the size of detectors matrix is 160×120 pixels. Thermovision camera was placed on tripod, perpendicular to measured surface, at a minimum possible distance (24 inches), in accordance with instruction [8, 7].

The emissivity $\varepsilon$ of grinded sleeve made of steel 40H was found in an emissivity table being given in instructions supplied with a device. It ranged from 0.4 to 0.6 [7]. During the analysis of recorded thermograms for the measurements of workpiece temperature, an average value of $\varepsilon = 0.5$ was taken from the specified range. The emissivity of grinding wheels was chosen from the same table, being the value for ceramics $\varepsilon = 0.95$.

The accuracy of temperature measurement made with thermovision camera was defined as the sum of errors arising from measurement conditions (distance from source and source size) and the precision of device. A total measuring error calculated in this way did not exceed ±3%.

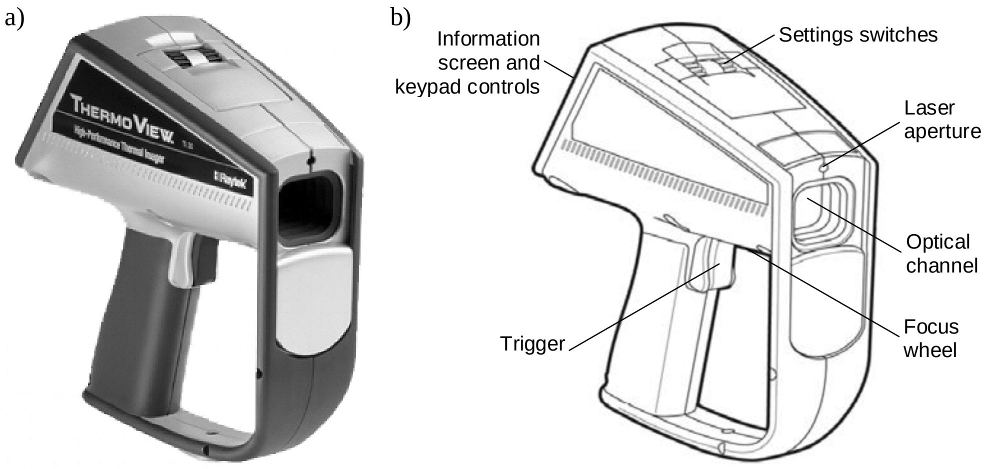

Fig. 2. Thermovision camera of Raytek ThermoView Ti30 type: a) overall view; b) functional elements [7]

In order to measure temperature directly in grinding zone, that is in the place where grinding wheel comes into contact with workpiece, special measurement sleeve was designed (Figure 3).

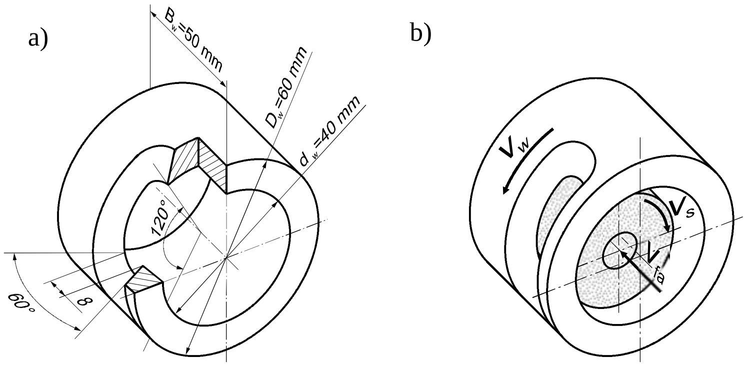

Fig. 3. Sleeve for thermovision temperature measurement in single-pass internal cylindrical grinding: a) dimensions of sleeve, b) kinematics of grinding

A special slot was made on the one third of sleeve circumference. Slot flanks were inclined at an angle of 60° to enable registering temperature in a direct proximity to grinding zone. Workpiece was made of 40H steel of hardness 53±2 HRC. Additionally, a rotational speed of workpiece was maximally reduced ($n_w$=18 rpm) to allow single measurement exactly at the moment when sleeve slot was opposite to infrared detector and working zone was uncovered.

Investigations were carried out without cooling liquid ($Q_{CCS} = 0$). That is why the thickness of machining allowance removed in single-pass of grinding wheel was decreased to $a_e = 0.025$ mm. The angle ($\chi = 0.14°$) and the width ($b = 10$ mm) of conic chamfer were matched to the value of working engagement.

Three grinding wheels with characteristics shown below were investigated:

- 1-35×20× 10-SG/F60 K 7 V DG – short designation: SG F60;
- 1-35×20×10-SG/F46 K 7 V DG – short designation: SG F46 (Figure 4);
- 1-35×20×10-99A/F46 K 7 V DG – short designation: 99A F46.

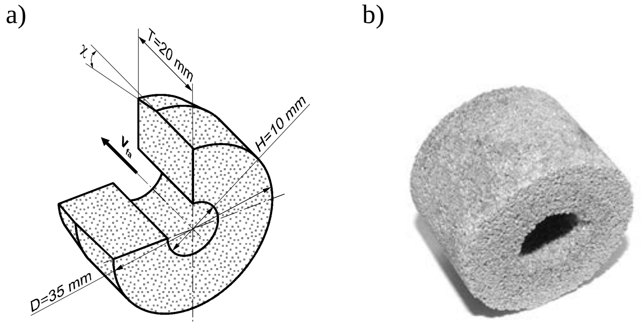

Fig. 4. Construction scheme (a) and overall view (b) of grinding wheel shortly named SG F46

Before grinding, during machining and just after it the thermograms were recorded with the frequency of one measurement during about 3 seconds. For each of grinding wheels the measurement was repeated three times.

### 3.2. Measurement results

The example of thermograms recorded during observation of single-pass internal cylindrical grinding with SG F46 grinding wheel is presented in Figure 5.

The results of all thermovision measurements were given in the Table and presented in Figure 6.

The most favourable (the lowest) temperatures in grinding zone were recorded for grinding wheel built of SG grains size 46 (average value $\Theta_p = 169$ °C). The temperature measured for analogous grinding wheel with grains size 60 was by about 15% higher ($\Theta_p = 194$ °C). This means that an increase in the grain size has been caused the reduction of thermal load in the process examined. This can be explained by larger intersections of layers machined by single grain. Bigger chips formed under these conditions allow us to throw the heat out, and as a result the workpiece had lower temperature. When on an active surface of grinding wheel the number of bigger grains is small, friction is reduced. Bigger intergranular spaces ensure effective removal of chips from machining zone and deliver cooling medium into it (in our investigations grinding wheel was cooled by air).

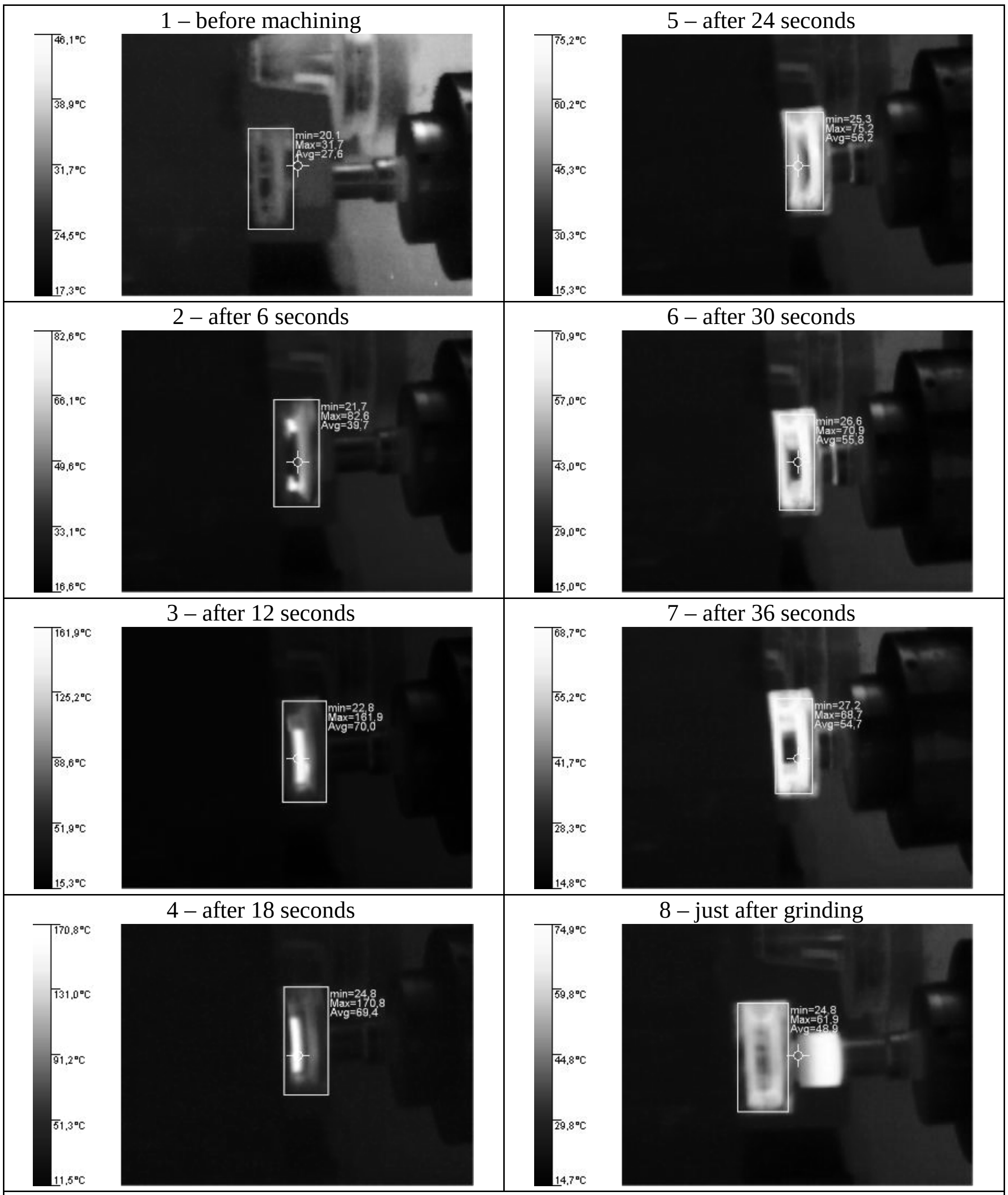

$v_s$ = 60 [m/s] $v_w$ = 0.04 [m/s] $a_e$ = 0.025 [mm] $q$ = 1517
$n_s$ = 40600 [rpm] $n_w$ = 18 [rpm] $v_{fa}$ = 1.0 [mm/s] $Q_{CCS}$ = 0 [l/min]

Fig. 5. The example of thermograms recorded during single-pass internal cylindrical grinding

Table. The results of temperature measurements in machining zone during single-pass internal cylindrical grinding process

| Grinding wheel | Measurement series | The highest temperature recorded $\Theta_p$ [°C] | Average value $\Theta_p$ [°C] |
|---|---|---|---|
| SG F60 | 1 | 177.4 | 194 |
| | 2 | 189.8 | |
| | 3 | 216.1 | |
| SG F46 | 1 | 144.3 | 169 |
| | 2 | 170.8 | |
| | 3 | 192.4 | |
| 99A F46 | 1 | 196.4 | 200 |
| | 2 | 175.9 | |
| | 3 | 228.5 | |

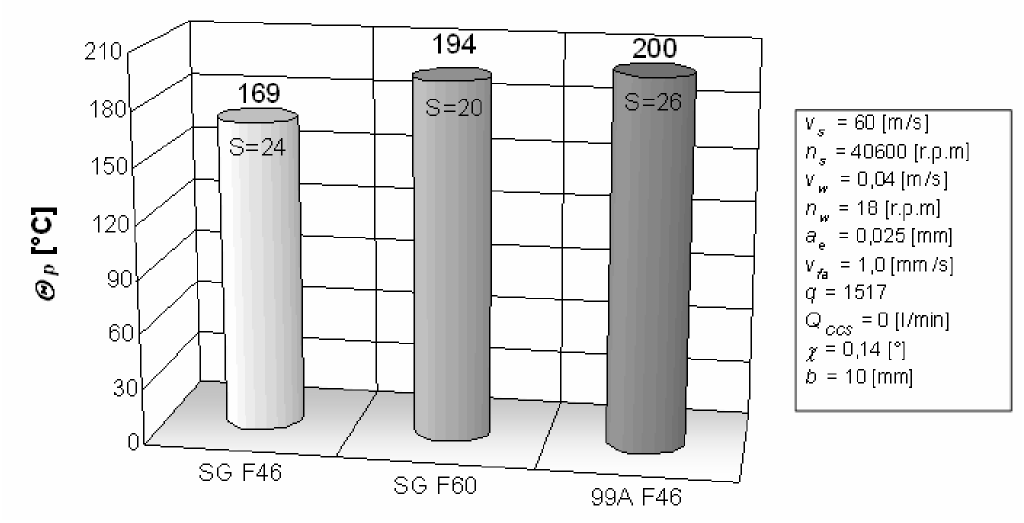

Fig. 6. Average maximum temperatures $\Theta_p$ and standard deviation $S$ recorded in the grinding process with three different grinding wheels

The comparison of the results of testing the grinding wheels SG 46 and 99A F46, i.e., grinding tools built of identical grain sizes but different kind of grains, indicate that better thermal conditions of machining were ensured by sub-microcrystalline grains of sintered corundum. The temperature in grinding zone with grinding tool 99A F46 was by about 18% higher ($\Theta_p$=200 °C) than that in grinding zone with grinding wheel SG F46. First of all it was due to the difference in thermal conductivity $\lambda$ which is ~14 W/m·K for alundum 99A [9] and ~30 W/m·K [10, 11] for sintered corundum SG. Also better cutting ability of SG grains, which was due to microcrystalline structure of this abrasive material, affected the values being registered.

The thermograms of grinding wheel before and after machining (Figure 7) show that temperature increases from initial 26.4 °C to 53.8 °C. Low temperature measured after grinding was caused by air cooling effect of grinding wheel whose speed was over 40 000 rpm. Although maximum temperature values measured in the grinding process were above 200 °C, after several seconds needed to stop grinding wheel, the grinding tool temperature was four times lower.

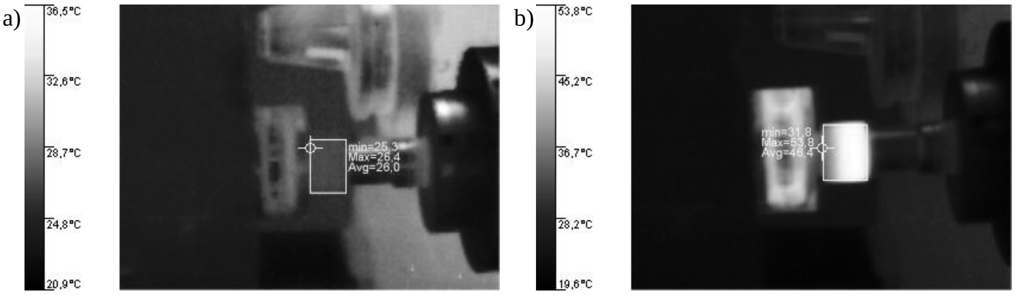

Fig. 7. Thermograms of grinding wheel SG F46: a) before grinding; b) after grinding

## 4. Conclusions

The temperature measurement in the grinding zone during single-pass internal cylindrical grinding was only a trial of measurements by means of thermovision methods. The method of observing machining conditions with slot in workpiece allowed us to collect information about temperature during grinding process. Taking account of the measurement method and the fact that the image registered during machining shows not only workpiece and grinding wheel but also chips, we can infer that the executed measurements did not give information about real temperature in grinding zone. The measurements allow only a comparative analysis of thermal conditions during grinding with different abrasive tools. However, if a camera with the detector of higher resolution is applied, the precision of measurements will improve.

### References

[1] Oczoś K.E.: *Development of innovative machining technologies*. Part II, Grinding Mechanics, 2002, 75, 10, pp. 627–637.

[2] Klocke F., Hegener G., Deacu L.: *Hochleistungs-Aussenrund-Formschleifen. Innovatives Fertigungsverfahren vereint hohe Flexibilität und Produktivität*, ZWF, 1996, 91, 4, pp. 164–167.

[3] Klocke F., Hegener G.: *Schnell, gut und flexibel: Hochleistungs-Aussenrund-Formschleifen*, IDR, 1999, 33, 2, pp. 153–160.

[4] Weinert K., Finke M.: *Innenrund-längsschleifen von futterteilen – bohrungen in einem überschliff fertig schleifen*, Materials of XXVI Scientific School of Abrasive Machining, Łopuszna, 2001, pp. 37–44.
[5] Weinert K., Finke M., Kötter D.: *Wirtschaftliche Alternative zum Hartdrehen. Innenrund-Schälschleifen steigert Flexibilität beim Schleifen von Futterteilen*, Maschinenmarkt, 2003, 109, 48, pp. 44–47.
[6] Nadolny K.: *Investigation of efficiency in single-pass internal cylindrical grinding process with grinding wheels whose structure is zonally diversified*, Dissertation, Koszalin University of Technology, 2006.
[7] *Raytek ThermoView Ti30 User's Manual*.
[8] Minikina W.: *Thermovision measurements – instruments and methods*, Publishers of Częstochowa University of Technology, Częstochowa, 2004.
[9] Oczoś K.E.: *Characteristic of development trends in grinding wheels grinding*, Materials of XXIII Scientific School of Abrasive Machining, Rzeszów-Myczkowce, 2000, pp. 13–62.
[10] Antoniewicz J.: *Dielectric prosperities. Tables and charts*, WNT, Warszawa, 1991.
[11] Dobrzański L.A.: *Lexicon of materials technology. Practical memorandum of Polish, foreign and international standards*. Volume IV, Verlag Dashöfer Publishers, 2005.

## Porównawcza metoda termowizyjnego pomiaru temperatury w procesie jednoprzejściowego szlifowania walcowych powierzchni wewnętrznych

Przedstawiono wyniki pomiarów termowizyjnych temperatury w strefie kontaktu ściernicy z przedmiotem obrabianym w procesie jednoprzejściowego szlifowania walcowych powierzchni wewnętrznych. Warunki takiej odmiany kinematycznej szlifowania skłoniły autorów do opracowania specjalnej metody pomiaru, umożliwiającej użycie kamery termowizyjnej. Przedstawiono istotę nowej metody oraz wyniki przeprowadzonych badań, w których określono wpływ rodzaju (elektrokorund szlachetny 99A, korund spiekany SG) i wielkości (46, 60) ziaren ściernych na temperaturę szlifowania.

ARCHIVES OF CIVIL AND MECHANICAL ENGINEERING

Vol. VI 2006 No. 4

# Aspects of bond layer role in concrete repairs

T. BŁASZCZYŃSKI, J. JASICZAK, B. KSIT, M. SIEWCZYŃSKA
Poznań University of Technology, ul. Piotrowo 5, 60-965 Poznań

The paper presents the role of a bond layer in the repair process of concrete and reinforced concrete elements as well as the place of its laying. For the purpose of a detailed analysis of the above problems two series of tests were carried out. In the first series of the tests, the influence of the state of the surface under repair (wet, oiled) on the adhesion of the bond layer is taken into account. In the second series, the influence of surface modification, grade of concrete and the placement of layers on the adhesion of bond layer to the surface was tested. It was shown that the use of a proposed polymer surface layer was possible both on wet and oil-contaminated surfaces. It was also proved that the adhesion of levelling layer (polymer–cement filler) to concrete is lower after sandblasting. The usage of the levelling layer under the polymer bond layer weakens their adhesion.

Keywords: *bond layer, polymer–cement filler, epoxy resin, pull-off test*

## 1. Introduction

For the repair of a given object or structure a diverse approach, depending on the kind of object, its sizes and function, is needed. In view of environmental influence and structural solutions, also a separate repair procedure is often required. If one assumes that concrete is the product of a simple technology and advanced knowledge which begins to be only mastered, then right prognoses are that the XXI century can be in large measure the age of repairs, rehabilitations and demolitions of building construction [1]. Concrete is relatively cheap as a construction material; however, its repair during the use of a house is very costly. Especially troublesome and expensive, and sometimes even operationally impossible, is the repair of already completed repair. Repairs became a civilisationwide problem [2].

The needs for repairs can be met in every kind of building construction, both in public buildings and industrial buildings. Most often the example of concrete structure repair in public buildings are balconies and loggias. In this case, the rain water is not always appropriately caught and carried and the selection of materials, especially damp- and waterproof materials, is not always carefully made. This influences the durability of building elements, which leads to their corrosion and repairs (Figure 1). A strong element dampness and consequently the dampness of the repaired surfaces pose a serious problem.

In industrial constructions, we deal with a considerably greater scale of structures which can suffer extensive damage and need repair. The largest group is formed by different industrial buildings, from engine rooms to the rooms for food-processing and chemical processes. It is especially important in the case of the works which are based on complicated technologies, where we deal with mixed corrosive environment [3]. The dampness of surfaces (Figure 2) is often the cause of damage which needs repair and reconstruction.

Fig. 1. Example of loggia structure damage

Fig. 2. Floors in room for protein hydrolysis and neutralisation (food-processing technology)

Another group of constructions subjected to destruction are industrial structures, e.g., machine foundations, especially turbine foundations (Figure 3).

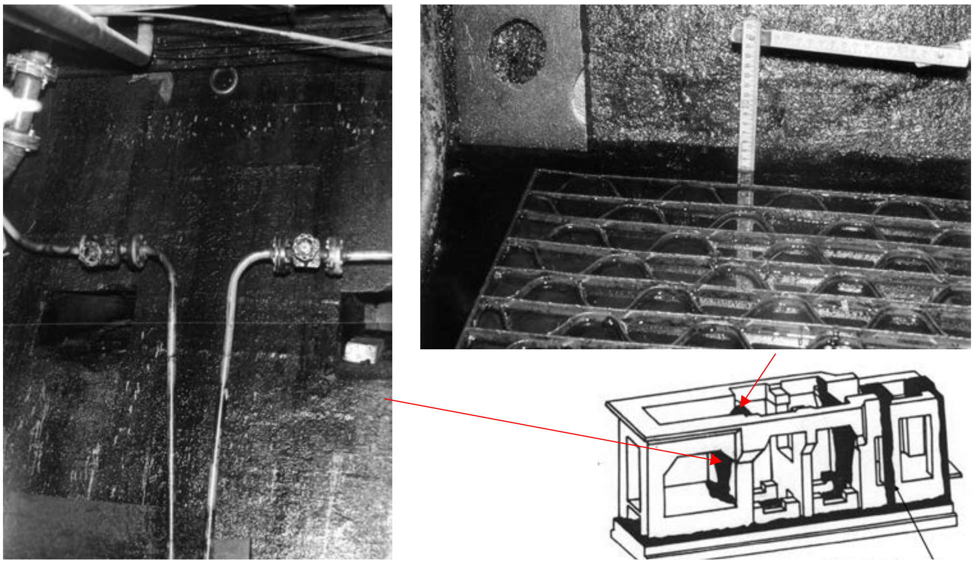

Fig. 3. Oiling in the case of frame turbine foundation (200 MW turbine)

A serious problem in the case of these structures repair is their considerable contamination with mineral oil [4]. These structures are subjected to the gradual cracking and oiling. Serious cracking, especially in oiled zones, causes a decrease in dynamic stiffness of these structures, which can lead to a serious damage to turbines, and even to disasters. That is why, apart from the place of their occurrence, cracks must be each time repaired. All surface defects and other surface damages have to be repaired as well. The lower level of such foundations is considered to be especially difficult place, where biological corrosion as a result of water–oil environment takes place (Figure 4).

Fig. 4. The lower level of 200 MW turbine foundation

## 2. Bond layer role

Before a proper placing of layers often grounding must be done, and also impregnation, which strengthen and tighten the concrete surface. The purpose of these superficial treatments was to assure a proper adhesion of repair material to concrete. This often affects greatly the efficiency of repair. The importance of adhesion is underlined in the standards EN 1504. In a technical sense, adhesion depends on the kind of material, the manner of surface treatment and the course of bond and hardening processes. The required adhesion, measured by pull-off test, for structural repairs and for non-structural repairs exceeds 0.5 MPa and 1.5 MPa, respectively. For structural repairs the usage of bond layers is recommended, and even required by ENV 1504-9 [5].

The placement of repair material directly on the surface under repair allows their proper adhesion. However, most often adhesion is improved by using suitable bond layers. The arrangement of bond layers must be done in such a way as to comply with technological conditions, because they can transform into their own opposition, i.e., to anti-adhesion layers. In the case of putting multi-layer systems, especially important is the maintenance of proper technological intervals, which can be a decisive factor in the efficiency of accepted material [6].

Materials used for of bond layers are usually modified cement pastes or cement micromortars or epoxy resins, which improve adhesion of mineral repair material to a concrete surface. In the case of concrete, adhesion of repair and protective coatings is relative to the degree of surface development, the kind of materials and their interactions. The greater a concrete surface roughness, the better the adhesion of the coating. Many epoxy bond products are available on the market. However, it must be remembered that fully useful are only these, which do not cause the steam-proof barrier, and consequently do not cause damages during their use.

In order to analyse in detail the above problems, two series of tests were carried out. In the first series of tests, the influence of the state of the surface under repair (wet, oiled) on the adhesion of the bond layer was taken into account. In the second series, the influence of surface modification, the grade of concrete and the placement of layers on the adhesion to the surface was tested.

## 3. Influence of concrete surface condition on bond layer adhesion

As we mentioned above, in the case of construction repairs, the surfaces under repair are in different states (i.e., wet, oiled). Therefore we tested adhesion of the accepted bond layer for three different surfaces (Figure 5): air-dry surface (variant A), wet surface, where the accepted moisture was >8% (variant B) and the oiled surface (variant C). Additionally the surface being oiled for six years was tested (variant C1).

Experiments were carried out on concrete slabs with the dimensions of 300 mm × 300 mm × 40 mm, made from concrete B30, with the maximum aggregate granulation of 8 mm. As the bond layer a solvent-free, two-component epoxy resin ASODUR-SG2

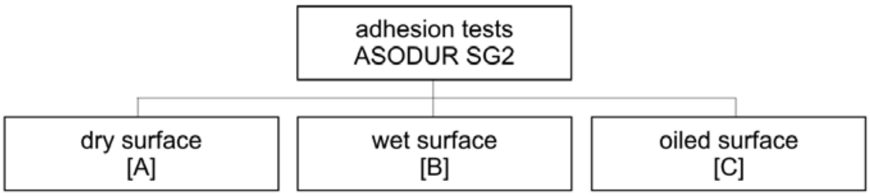

Fig. 5. Adhesion tests in the first series of tests

was used, as emulsifying medium ASO-ROO8 was applied. The epoxy resin ASODUR-SG2 was chosen because of its high coefficient of the diffusive resistance $\mu$. The tests were conducted for two layer thickness dependent on the quantity of spreading (spreading done twice and quadruple was assumed).

### 3.1. Surface preparation

On the air-dry and wet surfaces, bond layer was spread directly after the preparation of resin according to a manufacturer instruction. Before spreading resin on the oiled surface, the surface was cleaned with ASO-R008 emulsifying medium (Figure 6).

| air-dry [variant A] | wet [variant B] | long term oiling<br>[variant C1] |
|---|---|---|
|  | 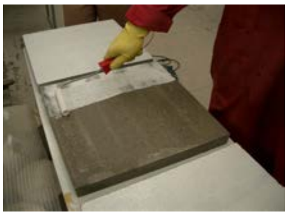 |  |

Fig. 6. Spreading of bond layer on concrete surfaces

Samples with an oiled surface were immersed in oil TU-20 at half height, and then at ¾ height, until a full immersion was achieved. The sample immersion was continued of 14 days, then the sample was taken out of the oil, dried, and before spreading epoxy resin its surface was rinsed with emulsifying medium. The wet sample was prepared in a similar way, and for spreading the bond layer it was taken out of the water environment directly before the investigation and dried superficially. Finally it was covered with resin coating. In the case of dry surface, the sample was kept for 14 days in standard laboratory conditions, i.e., at the temperature of 18 ºC and relative humidity of 55%.

### 3.2. Tests and results

Adhesion of bond layer (epoxy resin) to the concrete surfaces described above was examined by means of pull-off test. The method of testing consisted in measuring the minimal force applied perpendicularly to sample layers (Figure 7).

Fig. 7. Examination of bond layer adhesion to concrete surface

The results obtained prove that, irrespective of the surface state, the values of bonding force are higher than those in technical specifications (Figure 8, oiled state variant C).

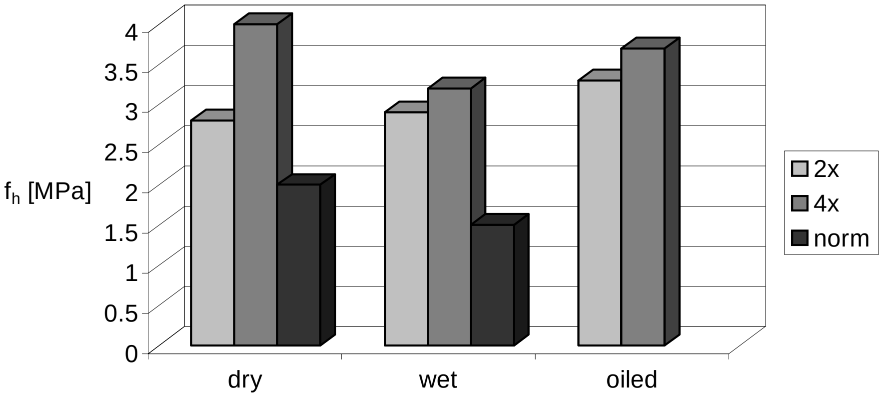

Fig. 8. Adhesion (separation) stress $f_h$ results, where: 2× – coating being two times spread, 4× – coating being four times spread, norm – non spread

The bond layer used adhered firmly to wet and oiled surfaces. It should be stressed that the destruction of all samples followed between concrete surface and the bond layer, both in the case of twice and quadruple spreading of resin (Figure 9).

| | air-dry [variant A] | wet [variant B] | oiled [variant C] |
|---|---|---|---|
| coating 2x spreading |  |  |  |
| coating 4x spreading |  |  | 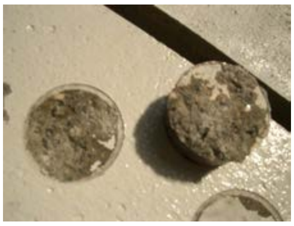 |

Fig. 9. The view of examined surface after the separation

During the experiments it was also observed that the use of emulsifying medium on oiled surface gives the layer blocking with oil in the contact zone (between grounding coat and concrete surface); though the sample is still in oiled state, oil does not cover the concrete surface. Separate test was prepared: after the use of emulsifier the surface of the sample C was wiped with white material. The spots of oil did not appear on a material surface.

## 4. Influence of surface preparation technology method, concrete grade and repair technology on bond layer adhesion

In order to assess a protective coatings adhesion to concrete, depending on the degree of surface development, the pull-off tests were carried out. The tests were conducted with concrete cube specimens (15 cm × 15 cm × 15 cm). In all examinations, the following grades of concrete were chosen: B5, B10, B15, B20, B25, B30, B35, B45, B50, B60 and B65 (according to [7]). Concretes of grade B35 were produced using gravel aggregate with the fraction of particle maximum size of 8 mm; granite aggregate was additionally added to concretes of grade above B35.

### 4.1. Preparation technologies

Two-sided faces of samples were cleaned by means of a stream-oriented sandblasting method, and then all surfaces became washed off by water under pressure, to obtain respectively two sandblasted surfaces and four surfaces, which were non-sandblasted (Figure 10).

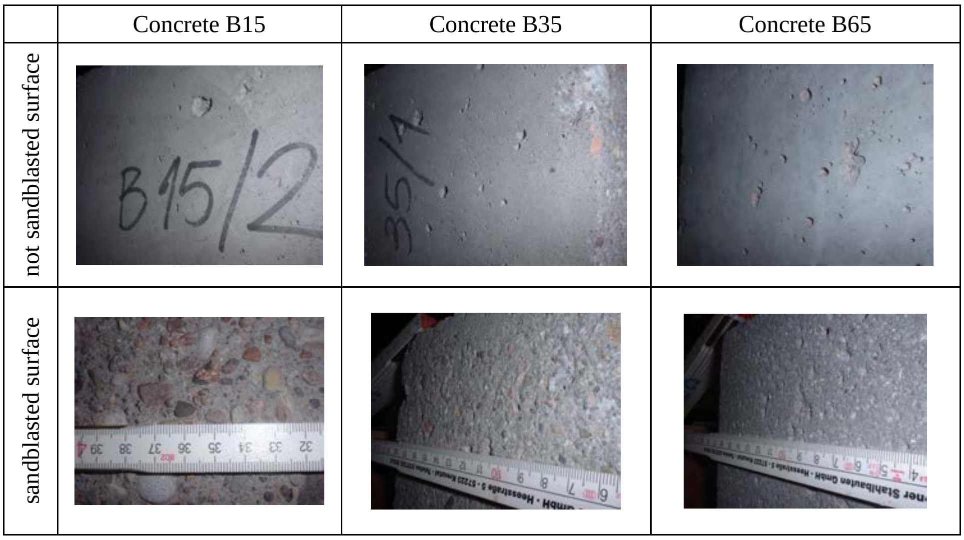

Fig. 10. Sandblasted and non-sandblasted surfaces of selected concrete grades (B15, B35, B65)

Non-sandblasted surfaces are smooth with small pores (near the surface) and with irregularities due to inaccurate fulfilment of formworks with concrete mixture. The sandblasting of cleaned surfaces is responsible for their roughness due to crumbling up the cement matrix and knocking-out smaller grains of the aggregate. The lower the grade of concrete and the size of aggregate grains more diverse, the more rough the surface after sandblasting.

The coats tested were put on the surfaces prepared in the way described. On the first sandblasted surface and the first non-sandblasted surface, only the bond layer was put on in the form of the resinous (ASODUR-BI) coat, and on the second sandblasted surface and the second non-sandblasted surface the first equalizing face polymer–cement-fill (ASOCRET-P/FS) was put on, and then the bond layer was spread. On the remaining two sides of cubes any coating was not put. The appearance of all kinds of surfaces, for all grades of concretes, after putting an equalizing layer and bond layer did not differ. In the case where only bond layers were put, the difference in the appearance of surfaces, depending on the grade of concrete and the surface treatment, was noticed (Figure 11).

Surface sandblasting increased the depth and the range of bond layer penetration, because the pores which are not present at the shuttering contact layer were opened; however, even after sandblasting a resin will not penetrate deeper than in the case of open pores. The penetration depth depends on concrete structure: the more porous (lower grade) concrete, the deeper the resin penetration. When concrete is more tight (higher grade), then resin is left on the concrete surface. The depth of resin penetration was examined by adding to it a red dye. In Figure 12, cube sections after coat spreading are presented.

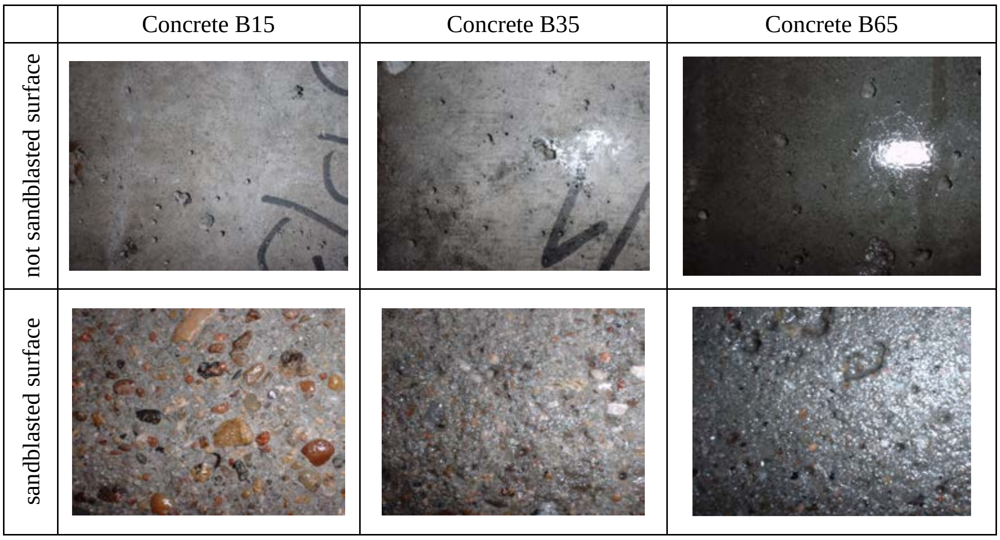

Fig. 11. Sandblasted and non-sandblasted surfaces after bond layer spreading

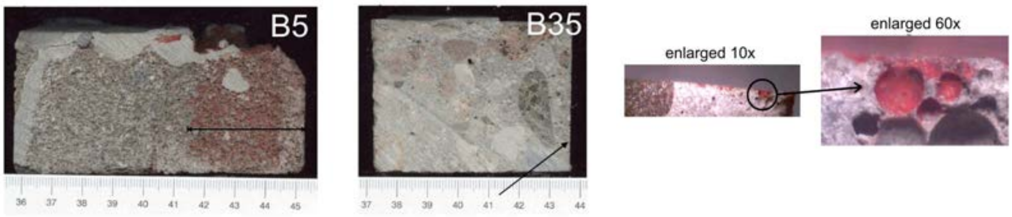

Fig. 12. Different-grade cube sections after bond layer spreading

## 4.2. Tests and results

Because many manufacturers recommend putting an equalizing layer before a proper bond layer spreading, two kinds of coating were investigated: resin spread directly on concrete and resin put on equalizing layer. The coating adhesion (separading force) was investigated by “pull-off” method. The findings of separating force for equalizing and bond layers are given in Figure 13, and these for bond layer only – in Figure 14.

In Figure 15, the relationship between tensile strength and compression strength of chosen concrete grades is presented.

An increase in the separating tension by about 1 MPa in the bond layer is observed in the case of non-sandblasted surface and surface lacking coatings. During the pull-off tests cracking always occurred in the concrete structure. No essential difference in separating tension between sandblasted and non-sandblasted surfaces was observed.

Sandblasting was of no importance in the case of bond layer only, because resin did not penetrate into concrete structure, but into open surface pores, which is shown in Figure 13. The increase in the value of separating tension was observed for low-grade concretes. For high-grade concretes further increase in separating tension value was not observed, it reached the value of about 6 MPa.

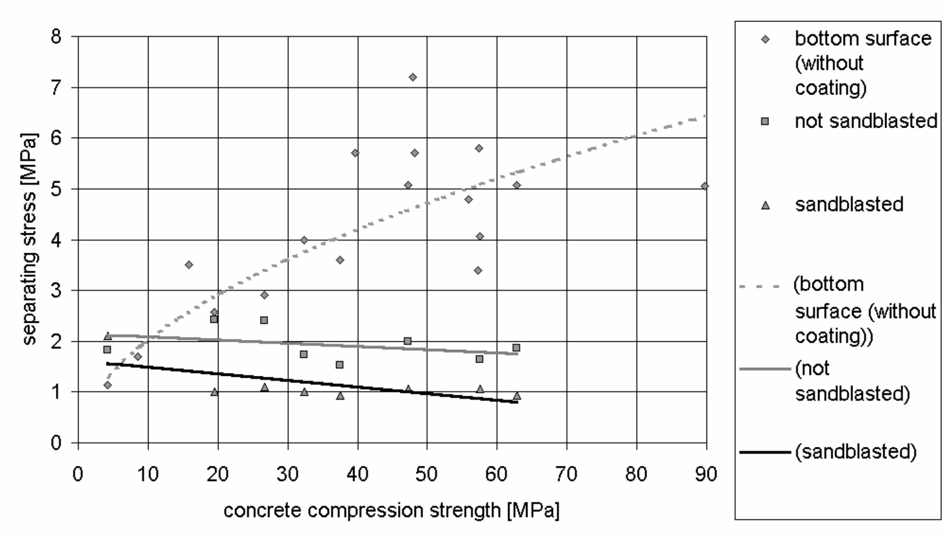

Fig. 13. Spreading stresses for equalizing and bond layers

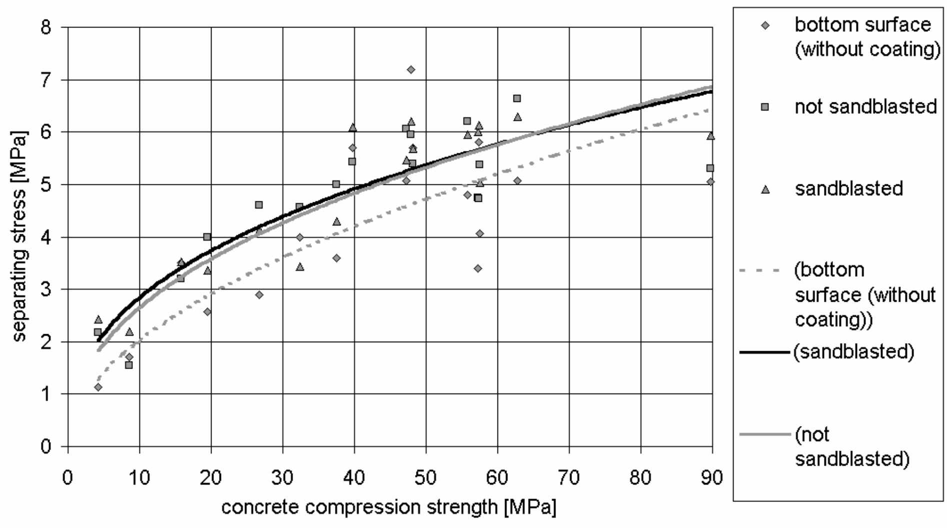

Fig. 14. Spreading stresses for bond layers only

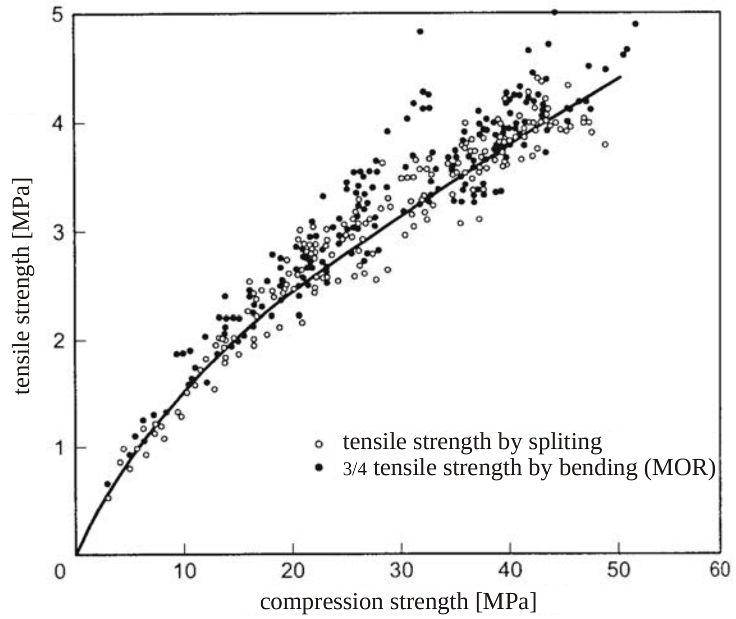

Fig. 15. Relationship between tensile strength and compression strength of chosen concrete grades

In the case of two-layer coatings, resin (bond layer) had no essential influence on the adhesion of equalizing layer, because it covered only the surface and did not penetrate into the concrete structure. During the pull-off tests, cracking was always observed in the equalizing layer structure, when the latter was formed on sandblasted surface, or in concrete–equalizing layer interface, when the equalizing layer was put on a non-sandblasted surface. The value of coating separating tension ranged from 1 MPa to 2 MPa, irrespective of concrete grade. Dry surface before spreading an equalizing layer was not grounded, so it absorbed moisture from the new layer before its setting. Thus surface sandblasting deteriorated the coating adhesion through the opening of surface pores, which absorbed water. Sandblasting developed the contact surface of both materials and improved adhesiveness, also due to mechanical adhesion.

## 5. Conclusions

A proper adhesion of repair material is a decisive factor in repair efficiency. In the technical sense, adhesion depends on the kind of material, surface preparation and the process of bonding and hardening.

The research showed that the bond layer in the form of epoxy material with a high coefficient of the diffusive resistance $\mu$ can be used for wet and oiled surfaces. This kind of bond layer, due to its molecular construction, penetrates deeply into the background, filling up pores and capillaries. In the case of bond layer, the coat should be spread at least twice. The second layer should be spread perpendicularly to the first one in order to assure its proof spreading on a given surface.

Putting the resin bond layer on a concrete improves mechanical features of concrete surface. Putting the equalizing layer under the bond layer is effective in low-grade concretes only. In the case of two-layer coatings, i. e., resin bond and equalizing layer, the latter influences greatly adhesion. If separating tensions in equalizing layer are compared it can be concluded that worse adhesiveness is observed for sandblasted surface. Resin does not penetrate into concrete structure, only into open surface pores, so in the case of resin bond layer the usage of sandblasting is not of essential importance. The usage of equalizing layer under the bond layer is effective at weak adhesion of coatings to concrete (from 1 MPa to 2 MPa).

**Acknowledgements**

The paper financed from budget resources for science in years 2005–2007.

## References

[1] Kucharska L.: *Failures and damages of concrete structures and their development* (in Polish), Proceedings of XX Structural Failure Conference, Szczecin-Międzyzdroje, 2001, 89.
[2] Czarnecki L.: *Selection of materials for repair of the reinforced concrete structures – compatibility criterion* (in Polish), Proceedings of XX Structural Failure Conference, Szczecin-Międzyzdroje, 2001, 145.
[3] Błaszczyński T., Zgoła B.: *Failure state of RC structure under mix corrosion environment* (in Polish), Proceedings of Structural Failure Conference, Szczecin-Międzyzdroje, 1997, 355.
[4] Błaszczyński T.: *Some effects of crude oil environment on RC structures*, Foundation of Civil and Environmental Engineering, 2002, No. 2, 7.
[5] ENV 1504-9: *Products and systems for the protection and repair of concrete structures. Definitions, requirements, quality control and evaluation of conformity* – Part 9: *General principles for use of products and systems.*
[6] Czarnecki L., Emmons P.H.: *Repair and protection of concrete structures* (in Polish), Polski Cement, Kraków, 2002.
[7] PN-B-03264:2002. *Plain, reinforced and prestressed concrete structures. Analysis and structural design* (in Polish).
[8] Jasiczak J., Grzelczak M.: *Influence of concrete surface cleaning on adhesion of repair layers* (in Polish), Proceedings of XLIX Scientific Conference, Krynica, 2003.

## Rola warstwy sczepnej w naprawach betonu

Przedstawiono rolę warstwy sczepnej w procesie naprawczym elementów betonowych i żelbetowych, jak również miejsca jej zastosowania. Aby szczegółowo zanalizować powyższe zagadnienia, badania przeprowadzono w dwóch seriach. W pierwszej zajęto się wpływem stanu naprawianej powierzchni (zawilgocenie, zaolejenie) na przyczepność warstwy sczepnej. Badania wykazały, że zastosowanie proponowanej warstwy sczepnej jest możliwe zarówno na powierzchniach mokrych, jak i skażonych olejem. W drugiej serii badań uwzględniono klasę betonu, wpływ obróbki powierzchni oraz wpływ rodzaju i technologii układu warstw na przyczepność warstwy sczepnej. Udowodniono, że przyczepność gładzi do betonu zmniejsza się po spiaskowaniu powierzchni. Stosowanie warstwy gładzi pod powłokę żywiczną skutkuje słabą przyczepnością powłok.

ARCHIVES OF CIVIL AND MECHANICAL ENGINEERING

Vol. VI 2006 No. 4

# Use of calibration chamber as a large triaxial apparatus

L. BAŁACHOWSKI
Gdańsk University of Technology, Narutowicza 11/12, 80-952 Gdańsk

A segment of a gravel column, 1 m high and 0.53 m in diameter, was modelled in a calibration chamber. The reconstituted sample was consolidated at a given confining pressure and then subjected to axial load exerted by the upper and lower membranes. Volumetric changes in both membranes and in internal chamber were measured. Up to 2% vertical strain was reached and internal friction angle was evaluated. Secant modulus of deformation was determined at considerable strains and at intermediate strain level in the unloading–reloading cycle. For the latter several times higher modulus was found.

Keywords: *calibration chamber, triaxial test, friction angle, deformation modulus, gravel*

## 1. Introduction

In laboratory determination of the shear strength and deformation characteristics of the gravelly soils or composite materials, a large-scale apparatus is indispensable since it allows grain size. To be accommodated large-size direct shear box was constructed to study the shear strength of railway ballast (Bolt [2]) or of gravelly surface layers in slope stability analysis (Fannin et al. [6]). The tests performed at small vertical stress applied to the box give an internal friction angle of gravelly soils even higher than 50 degrees. A new in-situ direct shear test was devised and applied to study the resistance of the block samples of coarse grained material to translation forces (Matsuoka et al. [12] and Fannin et al. [6]). Here, the shear strength of an undisturbed material in its natural state can be determined.

In order to evaluate the deformation characteristics of gravels at small strain, a large triaxial cell equipped with local strain gauge was used (Flora et al. [9]). The need for local strain measurements in gravel specimen is even more important than for the tests on sand. Here, some LDT-based systems are used (Flavigny et al. [8], Tatsuoka et al. [13], Da Re et al. [5]) or seismic wave propagation methods with bender elements (Brignoli et al. [3]), Fioravante et al. [7]), within a small-strain elastic region. The stiffness of gravelly soils subjected to small strains was also studied in calibration chamber using compression and shear wave propagation (Brignoli et al. [4]).

Gravel columns are often used to reinforce soft subsoil and to improve its drainage characteristics (Gryczmański [11]). A one-meter segment of a gravel column was modelled in the calibration chamber at Gdańsk University of Technology (GUT). Laboratory determination of the shear strength and deformation characteristics of gravel columns at considerable and intermediate strains is the objective of this study.

## 2. Test description

### 2.1. Calibration chamber device

The calibration chamber built at GUT enables large-size soil samples (Figure 1) to be tested in well defined boundary conditions. It is double-wall chamber with independent pressure control in internal and external chambers, which permits complex boundary conditions to be applied. The mass of the soil is confined by a rubber membrane. Vertical stress is applied to the specimen by the top and the bottom membranes filled with water. The water pressure in internal chamber is transmitted to the sample as a lateral stress. In this way, some kind of triaxial system is realised. Due to a substantial size of the specimen the vertical pressures in the upper and lower membranes are different and the lateral stress changes along its height. While at high confining stress this increase can be considered negligible, it is quite important in the case of the physical modelling of gravel column executed at small depths. The section of a gravel column with a length of 1.0 m and 0.53 m in diameter is modelled in the calibration chamber. The behaviour of the column section at a given depth can be analysed using different horizontal stress and increasing vertical stress applied in the chamber.

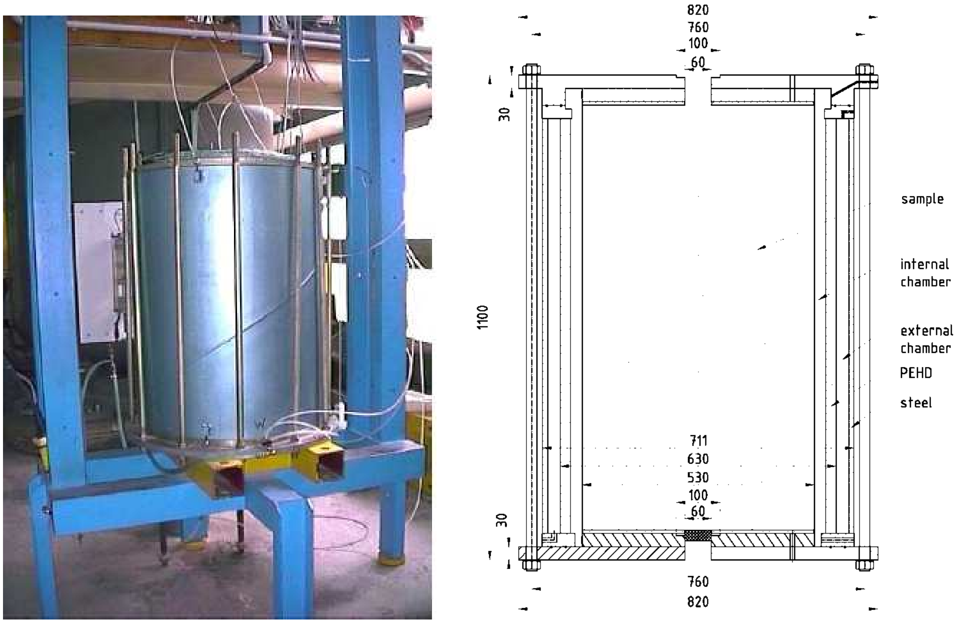

Fig. 1. View and cross-section of the calibration chamber at Gdańsk UT, Bałachowski and Dembicki

Volumetric changes of the specimen are measured in air–water columns mounted on the control panel (Figure 2) and equipped with micropulse transducers BTL2. The position of a floating element in the column is used to determine the water volume removed from the soil specimen or injected into it. Level monitoring with floating element is characterized by high precision and linearity. Double-wall construction of the air–water column compenstates for its deformations.

Fig. 2. Air–water column with level monitoring with micropulse transducers

### 2.2. Sample preparation

Well-graded ($U$ = 11.1) sandstone material consisting of angular grains with $d_{10}$ = 1.8 mm, $d_{50}$ = 9.5 mm and $d_{90}$ = 21.0 mm was used. The gravel specimen was reconstituted with five layers, each of them was mechanically compacted at natural water content of 3%. Special care was taken to avoid the membrane cut during compaction. The sample was consolidated at a given confining pressure. Three values of confining pressure $\sigma_3$ applied in the mid-hight of the sample were used: 30 kPa, 50 kPa and 70 kPa. Volumetric changes and water pressure in the upper and lower membranes and within internal chamber were measured during consolidation and loading phase.

## 3. Test results

Vertical stress (membrane pressure) applied to the specimen was steadily increased with horizontal stress kept constant in the internal and external chambers. Vertical strain $\varepsilon_1$ was expressed as the sum of volumetric changes in the upper and lower membranes (Figure 3). The volumetric changes recorded were bigger in the upper membrane than in the lower one.

At equal stress applied in the internal and external chambers, the measuring (internal) chamber does not deform laterally. As vertical deformations of the chamber are also restricted, the volumetric changes within the specimen can be precisely determined based on the measurements in the internal chamber. After initial contractancy some dilatancy of the specimen is obtained at larger strains (see volumetric changes recorded in the inner chamber).

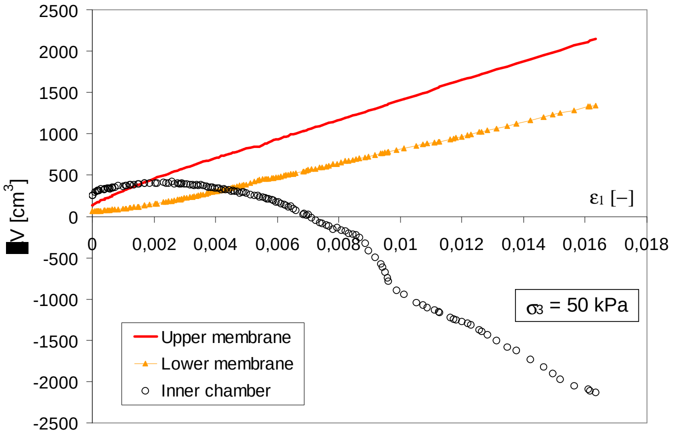

Fig. 3. Volumetric changes recorded during consolidation and shearing at a confining pressure of 50 kPa

The sample section during the shearing was corrected according to formula:

$$A_i = A_0(1-\varepsilon_1)\,, \tag{1}$$

where $A_0$ is the sample section after consolidation.

The compression test was carried out until relative stabilisation of the deviator stress, observed for $\varepsilon_1$ close to 2%, was achieved (see Figure 4). Each peak stress was reached within this strain range. Further membrane inflation could induce, however, non-uniform stress distribution on the lower and upper surfaces of the soil mass. Moreover, big volumetric changes observed in the membranes and internal chamber could not be accommodated to the measuring system designed for smaller volume variation during typical calibration chamber test on sand specimen. During the loading test the measuring chambers (Figure 2) were filled up with water a few times. These experimental difficulties induced some irregularities (Figure 4 and Figure 5) in the recorded values of volumetric changes. While a gravel column is steadily contracted at the horizontal stress of 70 kPa (Figure 5), some dilatancy is observed at lower confining pressures.

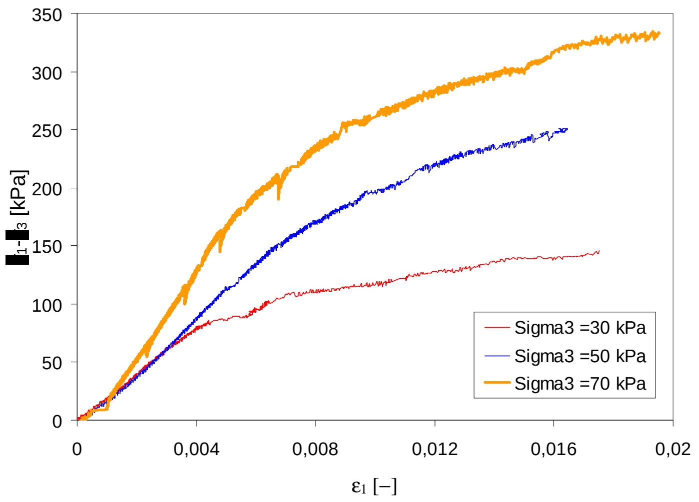

Fig. 4. Deviator stress at different confining pressures

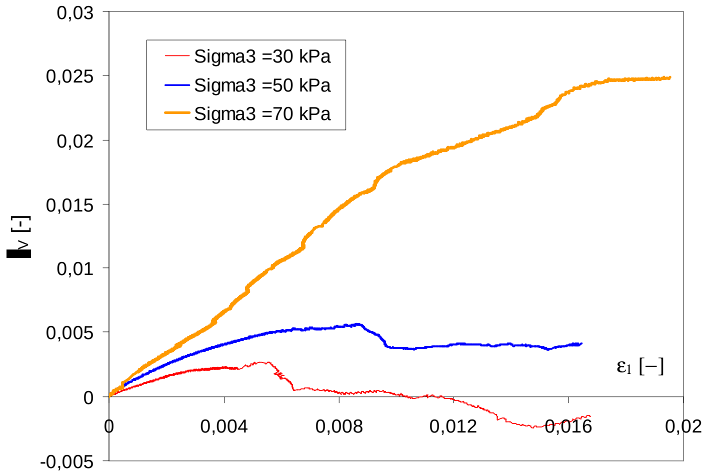

Fig. 5. Volumetric strain at different confining pressures

When the loading begins the membrane adjustment is observed due to grain rearrangement and grain penetration. This initial part of stress–strain curve is omitted in the calculation of deformation modulus. The tangent deformation modulus $E_t$ (Table 1) is calculated:

$$E_t = \frac{\dot{\sigma}_1 - \sigma_3}{\dot{\varepsilon}_1}, \qquad (2)$$

where:

$\dot{\sigma}_1$ – the increment of vertical stress,

$\dot{\varepsilon}_1$ – the increment of vertical strain.

Large strain tangent modulus is determined at the vertical strain increase of about 0.2%. Deformation modulus increases generally with confining pressure (Table 1). During some compression tests small unload–reload loops, with the amplitude of 20 kPa, were also made (Figure 6). The unloading–reloading secant modulus at a lateral stress of 70 kPa corresponds to the vertical strain increase of about 0.01%. Higher unload–reload modulus is found in each following loop due to soil compaction, grain rearrangement and vertical stress increase during the loading. This intermediate strain modulus is several times higher than the corresponding large strain modulus.

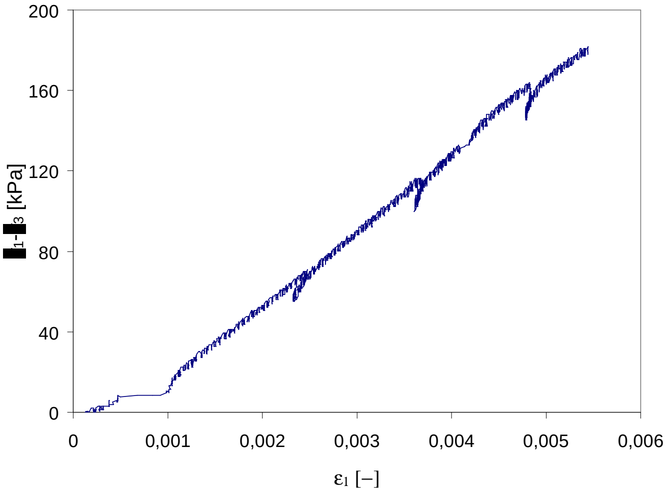

Fig. 6. Deviator stress with unloading–reloading loops at confining pressure of 70 kPa

Table 1. Deformation moduli of the gravel column

| $\sigma_3$ [kPa] | Modulus of deformation | |
|---|---|---|
| | Tangent $E_{0.2\%}$ [MPa] | Secant $E_{0.01\%}$ [MPa] |
| 30 | 21.6 | – |
| 50 | 26.5 | – |
| 70 | 38.5 | 85.6 at $\varepsilon_1 = 0.24\%$<br>109.8 at $\varepsilon_1 = 0.37\%$<br>136.0 at $\varepsilon_1 = 0.48\%$ |

The angle of internal friction was evaluated (Table 2) at the maximum vertical strain according to the formula:

$$\phi = \arcsin\frac{\sigma_{1\max} - \sigma_3}{\sigma_{1\max} + \sigma_3}, \tag{3}$$

where:

$\sigma_3$ – the confining pressure,

$\sigma_{1\max}$ – the maximum vertical stress applied to the sample.

Table 2. Values of internal friction angle

| $\sigma_3$ [kPa] | 30 | 50 | 70 |
|---|---|---|---|
| $\phi$ [°] | 44.4 | 45.6 | 44.6 |

## 4. Discussion

Quite low values of tangent deformation modulus of the gravel column are found in the calibration chamber. Embedding conditions on the upper and lower surfaces of the specimen play here an important role. Flavigny et al. [8] studied the effect of friction conditions and sample elongation on the shear strength mobilisation and volumetric changes in triaxial tests on fine Hostun sand. For the top and bottom surfaces of friction and elongated samples, the deformation modulus was from 1.2 to 1.35 times higher than for the specimen with the height to diameter ratio equal unity and with lubricated ends. The difference observed was larger for tangent modulus than for the secant one. An intermediate condition between the rough and lubricated ends is met on the top and bottom surfaces of the specimen in the calibration chamber. More uniform stress distribution over the upper and lower surfaces of the sample should be expected for the membrane filled with water than in the case of rigid end plates.

The membranes were additionally protected against grain penetration; however, some penetration can still occur. This phenomenon is responsible for the increase in the calculated vertical strain and the decrease in the estimated deformation modulus. Quasi-elastic deformation modulus determined in the unloading–reloading cycle is not practically influenced the grain penetration.

One should notice that the deformation moduli of a real gravel column will be higher than these determined in the calibration chamber due to:

- Higher compaction of the executed column than that reconstituted at laboratory.
- More rigid conditions on the boundaries applied to a real column segment than these applied to the soil mass in the calibration chamber.
- The surrounding soft soil which will restrict to some extent the lateral deformations of the column. We should apply the conditions that are intermediate between constant lateral stress and non-volume changes. The test with an imposed lateral stiffness will model the influence of the surrounding soil. This influence does not seem to be essential in the modelling of the gravel column.

- The transfer of vertical load not only on the column head, but to the surrounding soft soil as well. This complex transfer mechanism, i.e., the function of the column distribution, distance, a relative stiffness of the soft soil and column, depends also on the consolidation of the soft soil, Gryczmański [11]. It can be thus time-dependent.

Only global volumetric changes were recorded during the tests. Some local strain measurements would be however possible with displacement gauges or proximity transducers mounted on the membrane. Contrary to triaxial apparatus, in the calibration chamber neither the failure mode nor deformation localisation within the specimen can be observed.

Calibration chamber could also be applied to study some composites like tire chips/shreds–sand mixtures, Gotteland et al. [10]. Some CPT/DMT penetration tests could be performed in the composite mass which was not possible in the compacted gravel column. The deformation characteristics of the composite could be related to the deformation modulus from DMT and the internal friction angle–to the cone resistance in the calibration chamber.

## 5. Conclusions

As the gravel characteristics have hardly been studied in a typical triaxial test, they were determined during a loading test in the calibration chamber. A segment of the gravel column was modelled in the calibration chamber under constant lateral stress conditions. The behaviour of the column segment at a given depth was analysed using different horizontal stress applied in the chamber. Deformation moduli were determined at large and intermediate strains. The deformation modulus determined at unloading–reloading cycle was several times higher than that at large strains. The angle of internal friction of the gravel was estimated at the maximum vertical strain of about 2%. High values of internal friction angle close to 45 degrees were obtained.

The tests on gravel specimen in the calibration chamber are however time-consuming and troublesome, with a possible membrane cut and big volumetric changes not accommodated by the measuring system. The application of the calibration chamber as a large-size triaxial device is limited to relatively small about 2% vertical strain imposed by the membranes filled with water. Bigger volumetric changes in the lower and upper membranes could induce non-uniform stress and strain distribution on the column surface. However, such a level of vertical strain is not sufficient to approach the failure of all specimen, and especially of composite soils. Some data on the deformation characteristics of soil mass can be still deduced. In the case of certain materials, like sand-tire chips/shreds mixtures, calibration chamber could be used to determine deformation characteristics of the composite. As an advantage, a penetration test in calibration chamber could be performed on the same specimen.

## References

[1] Bałachowski L., Dembicki E.: *La construction d'une chambre d'étalonnage à l'Université Technique de Gdańsk*, Studia Geotechnica et Mechanica, 2003, Vol. XXV, No. 1–2, 21–26.

[2] Bolt A.: *Design of foundation for railways overhead line support structures*, Proc. Deep foundations, 19–21 March, Paris, 1991.

[3] Brignoli E.G.M., Gotti M. & Stokoe K.H.I.: *Measurement of shear waves in laboratory specimens by means of piezoelectric transducers*, ASTM Geotech. Test. J, 1996, 19, No. 4, 384–397.

[4] Brignoli E.G.M., Fretti C., Jamiolkowski M., Pedroni S., Stokoe K.H., II: *Stiffness of Gravelly Soils at Small Strains*, Proceedings, XIV International Conference on Soil Mechanics & Foundation Engineering, Hamburg, Germany, September, 1997, 37–40.

[5] Da Re G., Santagata M.C., Germaine J.T.: *LVDT based system for the measurements of the prefailure behavior of geomaterials*, Geotechnical Testing Journal, 2001, Vol. 24, No. 3, 288–298.

[6] Fannin R.J., Eliadorani A., Wilkinson J.M.T.: *Shear strength of cohesionless soils at low stress*, Géotechnique, 2005, 55, No. 6, 467–478.

[7] Fioravante V., Capoferri R.: *On the use of multi-directional piezoelectric tranducers in triaxial testing*, Geotechnical Testing Journal, 2001, Vol. 24, No. 3, 243–255.

[8] Flavigny E., Hadj-Sadok M., Horodecki G., Bałachowski L.: *Séries répétitives d'essais triaxiaux dans deux laboratoires*, Archiwum Hydrotechniki, 1991, Vol. XXXVIII, No. 1–2, 21–35.

[9] Flora A., Jiang G.I., Kohata Y., Tatsuoka F.: *Small strain behaviour of a gravel along some triaxial stress paths*, Proc. of International Symposium on Pre-Failure Deformation of Geomaterials, Shibuya et al., (Editors), Balkema, 1994, Vol. 1, 241–246.

[10] Gotteland Ph., Lambert S., Bałachowski L.: *Strength characteristics of tyre chips-sand mixtures*, Studia Geotechnica et Mechanica, 2005, Vol. 27, No. 1–2, 55–66.

[11] Gryczmański M.: *Metody analizy nośności i osiadania podłoża wzmocnionego kolumnami kamiennymi*, Inżynieria Morska i Geotechnika, 1993, No. 5, 224–231.

[12] Matsuoka H., Liu S., Sun D., Nishikata U.: *Development of new in-situ direct shear test*, Geotechnical Testing Journal, 2001, Vol. 24, No. 1, 92–102.

[13] Tatsuoka F., Sato T., Park Ch.-S., Kim Y.-S., Mukabi J.N., Kohata Y.: *Measurements of elastic properties of geomaterials in laboratory compression tests*, Geotechnical Testing Journal, 1994, Vol. 17, March, 80–94.

## Komora kalibracyjna jako wielkowymiarowy aparat trójosiowego ściskania

Wycinek kolumny żwirowej o długości 1 m i średnicy 0,53 m modelowano w komorze kalibracyjnej. Uformowaną i zagęszczoną próbkę konsolidowano w komorze przy zadanym naprężeniu, a następnie zwiększano naprężenia pionowe, mierząc zmiany objętości w membranach górnej i dolnej oraz komorze wewnętrznej aparatu. Badania prowadzono do uzyskania odkształcenia pionowego próbki około 2%, przy którym występuje względna stabilizacja dewiatora naprężenia. Określono wartości kąta tarcia wewnętrznego oraz moduły odkształcenia masywu gruntowego przy dużych odkształceniach (0,5%) oraz w cyklu odciążenie–powtórne obciążenie. W ostatnim przypadku uzyskano wielokrotnie większe wartości modułu odkształ-

cenia. Zastosowanie komory kalibracyjnej jako wielowymiarowego aparatu trójosiowego ściskania należy ograniczyć do zakresu odkształceń pionowych nie większych niż 2%. Poza tym zakresem naprężenia oraz przemieszczenia przekazywane na grunt przez membrany wypełnione wodą mogą być nierównomiernie rozłożone. W niektórych gruntach możliwe jest przeprowadzenie testu obciążenia masywu gruntowego w komorze z wykonaniem sondowania statycznego lub badania dylatometrycznego w komorze kalibracyjnej na tej samej próbce gruntu.

ARCHIVES OF CIVIL AND MECHANICAL ENGINEERING

Vol. VI 2006 No. 4

# Information about PhD thesis at the Civil Engineering Faculty and the Mechanical Engineering Faculty of Wrocław University of Technology

## Title: *The method of reliability level increase for logistic system of vehicle industry* (in Polish) *Metoda podwyższania poziomu niezawodności systemu logistycznego dla produkcji wielkoseryjnej w przemyśle motoryzacyjnym*

**Author:** Iwona Kuprowska
**Supervisor:** Professor Tomasz Nowakowski, Wrocław University of Technology
**Promoting Council: Scientific Council of Institute of Machines Design and Operation**
**Reviewers:**
**Professor** Marek Fertsch, Poznań University of Technology
**Professor** Jan Kulczyk, Wrocław University of Technology
Date of PhD thesis presentation: October 17th, 2006
PhD is available in Main Library of Wrocław University of Technology
The monograph contains: 160 pages, 47 figs, bibliography: 70 items
Keywords: *logistics, reliability, controlling, production, combustion, engine*

*Abstract*: The aim of the monograph was to develop the method of increasing the reliability of logistic system and formulate the concept of avoiding failures and disturbances which occur in the system analyzed. The method is based on the quality assessment that integrates all functions which influence the cooperation between a supplier and a buyer and allows the supplier to improve their product. The main disadvantage of the previous method is partial and incomplete reliability assessment. The new method is implemented in European enterprises of Mahle consortium.

# **Title:** ***Analysis of the states of serviceability and load capacity limit of prestressed concrete members of circular hollow section*** **(in Polish)** ***Analiza stanów granicznych nośności i użytkowalności zginanych elementów sprężonych o przekroju pierścieniowym***

**Author:** Tomasz Oleszkiewicz
**Supervisor:** Professor Mieczysław Kamiński, Wrocław University of Technology
**Promoting Council: Institute of Civil Engineering, Wrocław University of Technology**
**Reviewers:**
Professor Leonard Runkiewicz
Professor Sylwester Kobielak, Professor of Wrocław University of Technology
Date of PhD thesis presentation: November 10th, 2004
PhD is available in Main Library of Wrocław University of Technology
The monograph contains: 340 pages, 201 figs, bibliography: 175 items
Keywords: *prestressed concrete, spun concrete, circular hollow section, bending*

*Abstract*: The results of experimental and theoretical investigations of the behaviour of prestressed circular hollow members subjected to monotonically increasing bending moment are presented. Two prestressed and three partially prestressed simply supported beams were tested. In this research, an extensive test programme has been carried out to study cracking, deformations, strain and stress distribution over the cracked cross section, and ultimate strength of tested beams when subjected to quasi-static loading. An investigation of the mechanical properties of spun concrete was conducted. A comparison between the properties of spun and vibrated concrete also was made. Based on the experimental results, new formulae for prediction of concrete compressive strength in prestressed flexural members and cracking moment in prestressed concrete members of circular hollow sections have been developed. The calculated stress distributions were also used to develop a simplified method of computing the ultimate flexural strength of the overreinforced prestressed members of circular hollow sections. The thesis contains a comprehensive overview of various design code recommendations for calculating cracking moment, deflection and ultimate moment capacity of prestressed concrete members of circular hollow.

# Title: *The influence of elasticity of a polymer journal bearing on its tribological properties* (in Polish) *Wpływ podatności polimerowego łożyska na jego właściwości tribologiczne*

**Author:** Mirosław Pitorak
**Supervisor:** Doctor Stanisław Krawiec
**Promoting Council: Institute of Machines Design and Operation, Wrocław University of Technology**
**Reviewers:**
**Professor** Marian Szczerek
**Doctor** Wojciech Wieleba
Date of PhD thesis presentation: November 16th, 2004
PhD thesis is available in Main Library of Wrocław University of Technology
The monograph contains: 100 pages, 114 figs, bibliography: 69 items

Keywords: *polymer journal bearings, elasticity, FEM models, design*

*Abstract*: The literature survey includes selected problems of the tribology of polymers and discusses the influence of some selected bearing parameters on the service life of journal bearings. The following thesis was put forward: a proper design of the shell of a journal bearing limits edge contact pressure and increases the longevity and load carrying capacity of this bearing. A few own proposals for polymer journal bearings with a flexible shell were presented. These were analyzed using the FEM method. A detailed analysis of the geometrical features of the selected solution for its elasticity (pressure distribution) was carried out using the FEM method. The same solution was experimentally tested to validate the assumed FEM model and to establish functions linking wear with selected geometrical features of the bearing.

# Title: *The influence of mechanical parameters of mineral-cement-emulsion mixtures on the bearing capacity of pavement structures* (in Polish) *Wpływ parametrów mechanicznych mieszanek mineralno-cementowo-emulsyjnych na nośność nawierzchni drogowych*

**Author:** Jarosław Kuźniewski
**Supervisor:** Professor Antoni Szydło
**Promoting Council: Institute of Machines Design, Wrocław University of Technology**
**Reviewers:**
**Professor** Józef Judycki, University of Technology, Gdańsk
**Professor** Jan Kukiełka, University of Technology, Lublin
Date of PhD thesis presentation: June 9th, 2004
PhD thesis is available in Main Library of Wrocław University of Technology
The monograph contains: 218 pages, 139 figs, bibliography: 146 items

Keywords: *mineral-cement-emulsion mixtures, laboratory test, pavement structures, bearing capacity*

*Abstract*: The influence of temperature and composition of cement-emulsion-mix on the strength and strain parameters was established. The fatigue criterion of mineral-cement-emulsion (MCE) mix was assumed. Acoustic emission parameters and their correlation with initiating stresses and critical stresses and with the fatigue limits were analyzed. The work pavement structures, whose base course was made from MCE mix, were also studied. The measurements of mechanical parameters such as: flexural, tensile and compression strength were carried out. There were performed fatigue tests including the initiating stresses and critical stresses by acoustic emission and modulus of elasticity. Based on the research we have determined physical properties of the mixtures such as: shrinkage, a clear area content, absorbability and resistance to frost. It was found a correlation between the strength parameters and a close relation between static and dynamic moduli. It was also stated that the initiating stresses coincide with the fatigue limits. It was demonstrated that the fatigue life of pavement structures whose base course was made from MCE mix had to be defined in two-phases. The first phase defines the fatigue life until a fracture of base course occurs, and the second phase is denoted by the fatigue life of asphalt layers or a base of strain after the fracture of the base course. The research confirmed that the mineral-cement-emulsion mixtures are useful for the production of the base course of pavement structures.